

Functionalized Surfaces and Surface Functionalization of Nanomaterials

Dissertation

Zur Erlangung des Grades

“Doktor der Naturwissenschaften”

**am Fachbereich Chemie, Pharmazie und Geowissenschaften
der Johannes-Gutenberg-Universität in Mainz**

von M.Sc. M.Phil. Muhammad Nawaz Tahir

geboren am 2. April 1976 in Jhang, Pakistan

Mainz 2006

TABLE OF CONTENTS

1. Introduction	1
1.1. Biosynthesis of nanomaterials.....	3
1.2. Synthesis of semiconductor metal oxides nanomaterials using silicatein	6
1.3. Surface functionalization of nanoparticles	10
1.4. References.....	15
2. Monitoring the Formation of Biosilica Catalyzed by Histidin-Tagged Silicatein	19
2.1. Introduction.....	19
2.2. Results and discussion	20
2.3. Conclusion	24
2.4. Experimental	25
2.5. References.....	29
3. Formation of Layered Titania and Zirconia Catalyzed by Surface-Bound Silicatein	30
3.1. Introduction.....	30
3.2. Results and discussion	32
3.3. Conclusion	37
3.4. Experimental	38
3.5. References.....	41
4. Controlling Au Nanocrystal Size and Shape by Chiral Induction Using Wildtype and Recombinant Silicatein from <i>Suberites domuncula</i>	43
4.1. Introduction.....	43

4.2. Results and discussion	44
4.3. Conclusion	53
4.4. Experimental	54
4.5. References.....	55
5. Facile Synthesis and Characterization of Functionalized, Monocrystalline Rutile TiO₂ Nanorods.....	58
5.1. Introduction.....	58
5.2. Results and discussion	59
5.3. Conclusion	66
5.4. Experimental	67
5.5. References.....	68
6. Reactive Polymers, a Versatile Toolbox for the Immobilization of Functional Molecules on TiO₂ Nanoparticles.....	70
6.1. Introduction.....	70
6.2. Results and discussion	72
6.3. Conclusion	78
6.4. Experimental.....	79
6.5. References.....	81
7. From Single Molecules to Nanoscopically Structured Functional Materials: Au Nanocrystal Growth on TiO₂ Nanowires Controlled by Surface Bound Silicatein	83
7.1. Introduction.....	83
7.2. Results and discussion	86
7.3. Conclusion	93

7.4. Experimental	95
7.5. References.....	97
8. Overcoming the Insolubility of Molybdenum Disulfide Nanoparticles Through a High Degree of Sidewall Functionalization Using Polymeric Chelating Ligands	101
8.1. Introduction.....	101
8.2. Results and discussion	105
8.3. Conclusion	110
8.4. Experimental.....	111
8.5. References.....	113
9. Facile Synthesis and Characterization of Monocrystalline Cubic ZrO₂ Nanoparticles	116
9.1. Introduction.....	116
9.2. Results and discussion	117
9.3. Conclusion	122
9.4. Experimental.....	123
9.5. References.....	124
10. Mineralisation of CdS on Gold Colloids Using Metal-Organic-Inorganic Architecture	126
10.1. Introduction.....	126
10.2. Results and discussion	128
10.3. Conclusion	132
10.4. Experimental.....	133
10.5. References.....	134

11. Summary and Conclusions.....	136
12. Methods and Instrumentation	140
12.1. Surface plasmon resonance spectroscopy (SPR).....	140
12.2. Atomic force microscopy (AFM).....	144
12.3. Confocal laser scanning microscopy (CLSM).....	147
12.4. References.....	149
13. Appendix	150
13. 1. List of figures.....	150

1. Introduction

Nanotechnology is an emerging interdisciplinary technology that has been booming in many areas during the recent decade, including materials science, machines, electronics, optics, medicine, energy and aerospace.^[1] Its profound societal impact has been considered as the huge momentum to usher in a second industrial revolution. The “nano” in nanotechnology comes from Greek word “nanos” that means dwarf. Scientists use the prefix to indicate 10^{-9} or one billionth. One nanometer is one-billionth meter that is about 100,000 times smaller than the diameter of a single human hair. Nanotechnology aims at manipulating atoms, molecules and nanosize particles in a precise and controlled manner in order to build materials with a fundamentally new organization and novel properties.^[2] The embryonic stage of nanotechnology is atomic assembly which was first articulated in 1959 by physicist Richard Feynman stating “there is plenty of room at the bottom”. Whereas the mature form of nanotechnology will be molecular assembly to make nanobuilding for the design of nanocomposites or selforganizing nanodevices. This can be achieved through control on interfacial functionalization to mimic interdisciplinary approaches.

The present doctorate work is an attempt to contribute to one important branch of nanotechnology-nanobiotechnology. Making most use of the surface functionalization as a tool to bring the artificially synthesized inorganic nanometer structures and naturally available biomolecules on a common platform, to produce hybrid products, this can be used as starting material to develop devices or structures to serve society in a productive and more practical way.

This dissertation is written in two parts, at the same time inter-related with each other. The products resulted are based on the common “*bottom up*” principle of nanotechnology, inspite of their different synthetic strategies. The different procedures gave versatility into their properties thereby broadening their area of application. The first part discusses the synthesis of insitu-functionalized hybrid nanomaterials in two ways. (a) Through biofunctionalized surfaces using self-assembled monolayers (SAMs) and (b) using functional organic molecules (biomolecules, polymers etc.) in solution. The second part describes the post-functionalization of inorganic nanomaterials utilising reactive organic functional groups, rendering the surface susceptible for further tailoring to produce organic-inorganic hybrid nanocompsites. In brief, **Chapter 1** gives an overview about biosynthesis of nanomaterials specially using hydrolytic

enzyme “silicatein” and the synthesis of pre- and post-functionalized metal, metal oxide and metal chalcogenide nanoparticles.

Chapter 2 describes that surface bound silicatein retains its biocatalytic activity, which is demonstrated by monitoring the immobilization of silicatein using a histidin-tag chelating anchor and the subsequent biosilicification of SiO₂ on surfaces by surface plasmon spectroscopy, atomic force microscopy and scanning electron microscopy.

Chapter 3 is an extension to illustrate the importance of surface bound silicatein. Silicatein immobilized on self-assembled polymer layers using a histidin-tag chelating anchor group not only retains its hydrolytical activity for the formation of biosilica, but catalyzes the formation of layered arrangements of biotitania and biozirconia.

In chapter 4 silicatein, a protein enzyme, which acts both as a catalyst and template for the formation of silica needles in marine sponges, has been used for the biosynthesis of gold nanocrystals. In a first reaction step, gold nanoparticles are formed by reduction of tetrachloroaurate, AuCl₄⁻, by the action of sulfhydryl groups hidden below the surface groups of the protein. The resulting gold nanoparticles which are stabilized by surface bound silicatein further aggregate to form Au nanocrystals. The triangular shape of the nanocrystals obtained by using recombinant silicatein can be explained by chiral induction through the protein during the nucleation of the nanocrystals.

Chapter 5 reports on the synthesis of functionalized, monocrystalline rutile TiO₂ nanorods, prepared from TiCl₄ in aqueous solution under acidic conditions in the presence of dopamine followed by aging and hydrothermal treatment at 150°C. The surface bound organic ligand controls the morphology as well as the crystallinity and the phase selection of TiO₂. The presence of monocrystalline rutile TiO₂ was confirmed by X-ray powder diffraction and HRTEM investigations. The as-prepared nanorods are resolvable in water at pH > 4. The surface functionalization was analyzed by IR, ¹H-NMR, confirming the presence of dopamine on the surface. The surface amine groups can be tailored further with functional molecules such as dyes. Confocal Laser Scanning Microscopy (CLSM) was used to characterize the binding of the fluorescent dye 4-chloro-7-nitrobenzylurazene (NBD) to the functionalized surface of the TiO₂ nanorods.

Chapter 6 describes the synthesis of reactive polymeric ligands which have been used successfully for the *in-situ* and post-functionalization of TiO₂ nanoparticles. Besides to chelating dopamine anchor group, the multifunctional ligand system presented here

incorporates a modifier molecule which allows the binding of functional molecules (here the dyes pyrene, NBD, and Texas Red) as well as additional entities which allow tailoring the solubility of inorganic nanocrystals in different solvents.

Chapter 7 illustrate the biofunctionalization of ceramic nanowires. Where silicatein, a protein related hydrolytic enzyme involved in the biomineralization of SiO_2 , was immobilized on the surface of TiO_2 nanowires with the aid of a reactive polymer, which simultaneously serves as an anchor to the oxide surface and as a chelating ligand for the binding of the protein. The surface bound protein not only retains its original hydrolytic properties, but also acts as a reductant for AuCl_4^- in the synthesis of hybrid TiO_2 /silicatein/Au nanocomposites.

Chapter 8 demonstrates the novel method for the surface functionalization of fullerene-type MoS_2 nanoparticles with polymeric ligands by complexation with a combination of Ni^{2+} via an umbrella-type nitrilotriacetic acid (NTA) and anchoring them to the sidewalls of TiO_2 nanorods. Synthesis of such a functional polymeric ligand was achieved via a reactive polymer precursor route. The interlinking of IF- MoS_2 is attractive for surface coatings of ceramics with IF- MoS_2 lubricants.

Chapter 9 describes the facile synthesis of monocrystalline cubic ZrO_2 nanoparticles. The nanoparticles are characterized using high resolution transmission electron microscopy (HRTEM), X-ray powder diffraction, Raman Spectroscopy, and emission spectroscopy.

Chapter 10 depicts a strategy to use the functionalized gold nanoparticles to synthesize metal/metal sulphide nanocomposites. Exposing bare gold colloids to long-chain dithiols results in their precipitation owing to cross-linking of the thiol groups with gold surfaces; here, we demonstrate that through the use of a dithiol that has one of the thiol groups protected, we can, through attachment followed by deprotection, prepare gold colloids with exposed thiol; the uses of such ‘sticky’ colloids in creating complex architectures is demonstrated by using them to template the growth of CdS particles.

Chapter 11 and 12 includes a brief summary, conclusions, methods and instrumentation used in the present work. The appendix is given in *chapter 13*.

1.1. Biosynthesis of nanomaterials

The convergence of biotechnology and nanotechnology has led to the development of hybrid nanomaterials that incorporate the highly selective catalytic and recognition properties of

biomaterials, such as proteins/enzymes and DNA, with the unique electronic, photonic, and catalytic features of nanoparticles.^[3,4] The conjugation of nanoparticles and other nanoobjects (e.g. nanorods and nanotubes) with biomolecules is an attractive area of research within nanobiotechnology.^[5] Enzymes, antigens and antibodies, and biomolecular receptors have dimensions in the range of 2–20 nm, similar to those of nanoparticles, thus the two classes of materials are structurally compatible (Figure 1.1).

Most of the multicellular organisms have inorganic materials as an integral part of their hard tissues. There are 60 different kinds of minerals that perform a vital structural,

The Scale of Things -- Nanometers and More

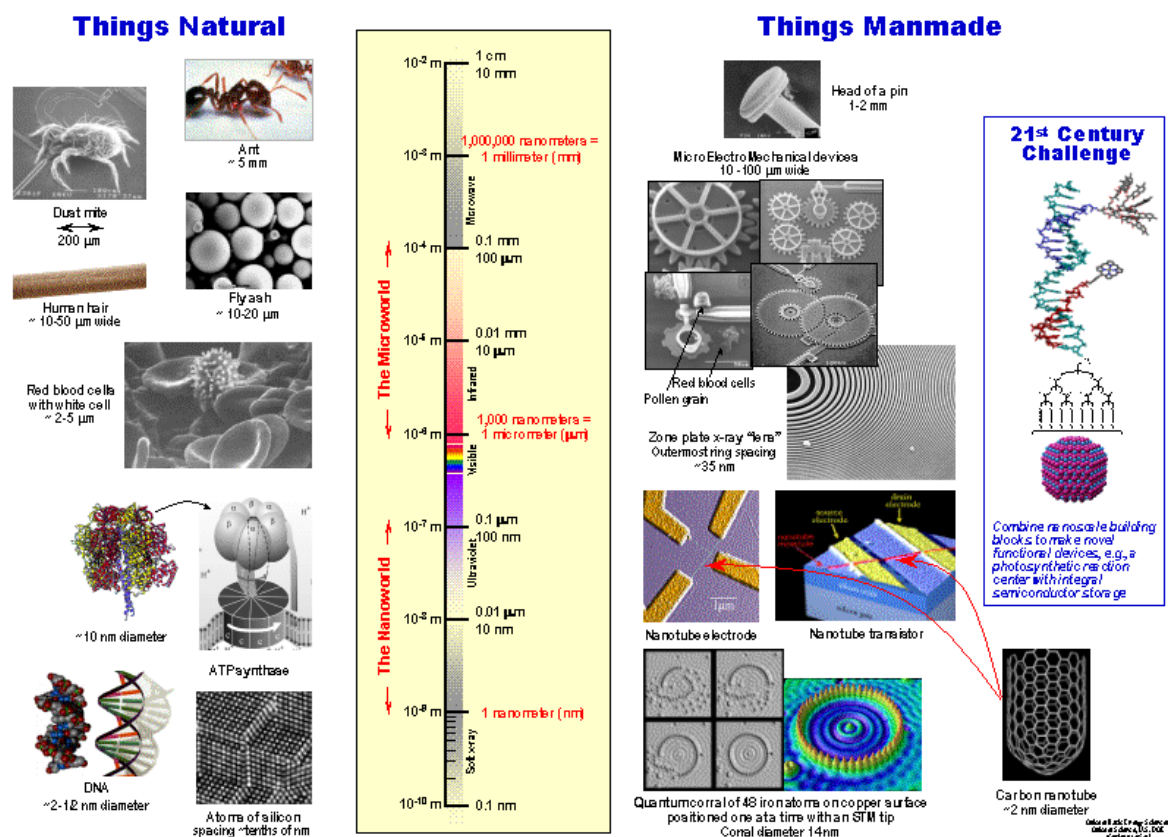


Figure 1.1. Comparison on length scale between naturally and artificially engineered materials

mechanical, and physiological role in the living organisms such as CaCO_3 , $\text{Ca}_3(\text{PO}_4)_2$, etc. Multicellular organisms and unicellular organisms such as bacteria and algae are capable of synthesising inorganic materials, both intra- and extracellularly.^[6,7,8,9] For example sponges, synthesize biosilica, magnetotactic bacteria synthesize magnetic particles, diatoms synthesize

biosilica and S-layer bacteria synthesize gypsum and calcium carbonate as surface layers.^[10,11,12,13,14,15]

Though solution based chemical methods enjoy a long history back to the pioneering work of Faraday on the synthesis of aqueous gold colloids, but at the same time, there is a rich and long history of gaining inspiration from nature for the design of practical materials and systems. Engineering materials are usually synthesized using a combination of approaches, for example, melting and solidification processes, followed by thermo mechanical treatments, or solution/vacuum deposition and growth processes. By contrast, biological systems use physiological conditions to synthesize inorganic nanoparticles and avoid the use of drastic conditions like high temperature, pressure and use of caustic chemicals. In this way these organism fulfills the requirement of nanotechnology which concerns with the development of experimental procedures for the reproducible synthesis of nanomaterials of controlled size, shape and crystallinity under facile conditions.

Nature has led to the “green chemistry” to synthesize inorganic materials on nano- and micro length scale with elegant species-specific structures with precise control on shape, morphology and crystallinity as shown in Figure 1.2.

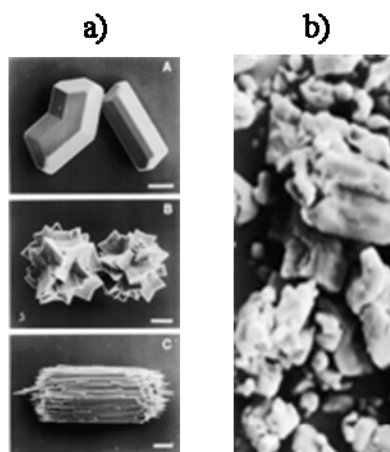


Figure 1.2. a) Oxalate crystal synthesized in plant leaves, b) Oxalate crystals synthesized in the laboratory.

Biosynthesis of inorganic materials has received the most attention in last few years. In a series of work, Tanja Klaus and coworkers showed that metal resistant bacterium, *Pseudomonas stutzeri* AG 259, resulted in the intracellular formation of silver and silver

sulphide nanoparticles when higher conc. of Ag ions were used for their culture.^[16,17,18] Another invention published by Nair et al showed that bacteria not normally exposed to large conc. of metal ions also be used to grow nanoparticles. These authors showed that *lactobacillus* strains present in butter milk, when exposed to silver and gold ions, resulted in the large scale synthesis of nanoparticles with in the bacterial cells.

Moreover they were able to show that lactic acid bacteria can be used to grow nanoparticles of alloys of gold and silver.^[19] Sastry and co-workers have described the formation of triangular shaped gold nanoparticles using lemon grass extract.^[20] Where biotransformation of gold acid into gold nanoparticles has control on shape and morphology.

Diatom unicellular microalgae show a high degree of complexity and hierarchical arrangement in their silica walls.^[21] Kröger et al. isolated phosphorylated proteins with polyamine “tail” termed silaffins. They were able to show that silaffins has pivotal role in the nanofabrication of diatom biosilica. The native silaffins are capable of assembling into supramolecular complexes by the intermolecular interactions between the negatively charged phosphate groups and polyamine moieties.^[22,23]

1.2. Synthesis of semiconductor metal oxides nanomaterials using silicatein

Marine sponges synthesize surprisingly well architected skeletal elements, the formation of which, in many instances, exceeds modern human engineering capabilities.^[24] These skeletal elements called spicules, not only provide the mechanical support to the whole body of sponge but also provide a uniquely docile model system for dissection of the molecular mechanisms controlling silica nanofabrication, and that the integral proteins of this and other marine biomineralized composites can be used to direct the formation of thin films of silica and other minerals with useful optical, electrical and magnetic properties.^[25,26]

These spicules (1-2 mm length × 30 μm diameter) are composed of silica with central axial filament of protein.^[24] Molecular biology of axial filaments and their role in biosilicification has led to the isolation of class of hydrolytic proteins called silicateins. On the basis of SDS-PAGE and electrophoresis analysis these protein are of three kinds and named α, β, and γ silicatein respectively. These subunits α, β, and γ are quite similar in aminoacids sequences and pI, with apparent molecular weights of 29, 28, and 27 kDa.^[27]

The presence of three different but related silicateins (silicatein- α , - β and - γ) as reported by Morse and coworkers^[27] in the axial filaments of spicules could not be substantiated at the molecular level; only genes encoding silicateins- α and - β could be isolated from *T. aurantium* (Shimizu et al., 1998; Cha et al., 1999)^[27,28] or other demosponges, e.g. *S. domuncula* (Krasko et al., 2000; Müller et al., 2005)^[29,30]. Comparison of silicatein α , and cathepsin L sequences reveals that the six cysteine residues that form the intramolecular disulfides in cathepsin L are fully conserved in silicatein, which that 3-D structure of both proteins are quite similar.

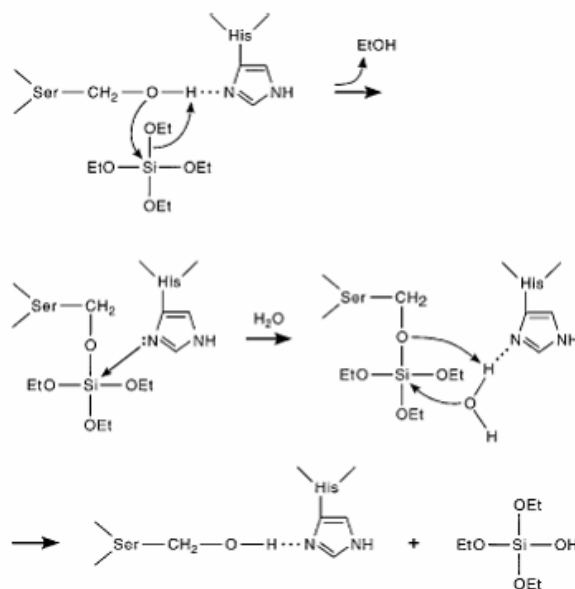


Figure 1.3. Catalytic mechanism of silicatein (Zhou et al 1999)

Two of the three residues (His and Asn) of the “catalytic triad” of the cathepsin L active site also are conserved in silicatein α , but the third active site Cys in cathepsin is replaced by Ser₂₆ residue in silicatein α . In this regard, the structure of silicatein α resembles with Ser proteases. From in vitro experiments using tetraethoxysilane (TEOS) as the silica precursor, silicatein protein was proposed to promote the hydrolysis and condensation of TEOS at neutral pH, a process which is typically acid or base catalyzed. It was proposed (Figure 1.3) that three active residues, serine, histidine and asparagine, catalyze the hydrolysis of TEOS by typical acid–base catalysis.^[31]

This result also shows the homology of silicatein α to the well known enzyme, cathepsin L, and Ser proteases enzyme. (Figure 1.4) Where the condensation of silicon alkoxides promoted by silicateins and cleavage of peptides catalyzed by the proteases both must proceed

through an obligatory hydrolysis reaction and both are known to be accelerated by general acid-base catalysis, suggesting that the mechanism of action of silicatein α in this process may be fundamentally related to that of its homologous enzyme counterparts.

Further experiments by site-directed mutagenesis of the silicatein protein, wherein either serine-26 or histidine-165 (both proposed to be at the active site) were replaced by an alanine residue, revealed that both of these amino acids were essential for catalysing the hydrolysis of TEOS at neutral pH.^[31]

Morse and coworkers has grafted the surfaces of gold nanoparticles via self assembled monolayers (SAMs) where the interface mimics the active site of silicatein and related hydrolases.^[32] They have used two kinds of gold nanoparticles, functionalized separately with organic moieties containing hydrogen-bonding (imidazole) and nucleophilic (hydroxyl) moieties closely resembling to those at the active site of silicatein α (imidazole from histidine and hydroxyl from serine). This model system constitutes an effective mimic of the enzyme capable of catalyzing the hydrolysis of silicon alkoxides and subsequently directing the condensation to form silica at physiological conditions. As expected, the interaction between the nucleophilic and hydrogen bonding containing functional groups grafted gold nanoparticles resulted in the formation of silica from silicon alkoxide at low temperature and neutral pH. Replacement of the either of the required functional groups by a non-reactive group like methyl failed to catalysis and condensation of silica. This finding confirms the mechanism of hydrolysis of alkoxide by silicatein proceeds through nucleophilic and hydrogen bonding of amino acids present in the active site of the protein.



Figure 1.4. 3-D structure of cathepsin L (right) and silicatein (left)

Cha et al. synthesized block copolypeptides to mimic the catalytic hydrolysis and polycondensation activity of silicatein.^[33] These copolypeptides were able to self assemble into structured aggregates that hydrolyze TEOS at neutral pH and low temperature and simultaneously directed the formation of ordered silica nanoparticles. By substituting the residues of these peptides with some suitable groups showed that the rate of catalysis was proportional to the strength of nucleophilicity of the nucleophilic side chain, that hydrogen bonding was required for efficient catalysis. Among the peptides tested, cysteine-lysine block copolypeptides were the most effective.

In the race of elucidating the mechanism for the biocatalyst “silicatein” Roth et al. put forward their efforts in mimicking small bifunctional molecules containing functionalities present in the active centre of silicatein. They concluded that cysteamine, which contains both –SH and –NH₂, showed the best catalytic activity in synthesising the silica at neutral pH and room temperature among the molecules were used. Also analogues lacking either one of these two functionalities exhibit a dramatic decrease in the catalytic activity. These findings are in good agreement with the results of alteration of the silicatein active centre by genetic engineering.

Investigation of mechanism governing the biological synthesis of silica structures in marine sponges, genetic engineering and biomimetic synthesis of silica confirmed that silicatein contains the catalytic triad (serine, histidine, and asparagines residues) typical of a large family of hydrolases.

The presence of catalytic triads in the structure of silicatein suggests that silicatein should be very diverse in catalytic activity. Biocatalytically templated synthesis of TiO₂ from water stable Titanium alkoxide using silicatein filaments at neutral pH and room temperature has been reported.^[35] The properties of the TiO₂ formed through this biocatalytic route differ from those of TiO₂ formed from the same precursor by via alkali catalysis or thermal pyrolysis. These authors could also be able to show the synthesis of gallium oxide and titanium phosphate using axial filaments of demosponge *tythea aurantium*.^[36] The in-vitro synthesis of biosilica using Histidine-tagged recombinant silicatein and formation of layered titania and zirconia has been demonstrated by Tahir et al. on Au(111) surface using self assembled monolayer of thiols.^[37,38]

1.3. Surface functionalization of nanoparticles

The rational synthesis of nanocrystalline materials appears to be a challenge in materials chemistry. Owing to the technological importance (photoluminescence, solar energy conversion, photo catalysis, biomaterials, etc),^[39,40,41] the development of improved pathways for the synthesis of nanomaterials with a control of particle size, shape and crystallinity is the fundamental object of nanochemistry.^[42] The use of nanomaterials in technological applications is limited because of their restricted behaviour in different solvents. Molecular engineering on the surfaces of nanoparticles surface helps the nanomaterials to tune their properties which plays a vital role in exploring and developing their applications in the field of nanotechnology.^[43]

The surface properties of nanoparticles determine the interaction among the components, as well as the solubility and agglomeration behaviour in different solvents and thus, decide whether individual nanocrystals are stable as nanobuilding blocks for the design of nanocomposites or for self organizing nanodevices^[44]. Moreover, the surface modifying groups of the nanoparticles can be used to couple the unique electronic, photonic, or catalytic properties of quantum-size nanoparticles with molecular or macromolecular functionalities to yield hybrid systems with advanced features^[44a]. For example, nucleic acid-functionalized Au nanoparticles, exhibiting a characteristic red color originating from the single-particle plasmon exciton, turns blue upon hybridization with the target DNA due to the formation of an interparticle-coupled plasmon exciton^[44b].

There are different approaches to modify the surfaces of inorganic nanomaterials to make organic-inorganic nanocomposites. The simplest approach is to entrap an inorganic component in an organic host, or vice versa. Examples include inorganic-organic hybrid polymers with interpenetrating but otherwise nonconnected inorganic and organic networks, polymers filled with inorganic nanoparticles, or layered inorganic compounds interclated with organic molecules. In the second class of inorganic-organic hybrid materials, strong covalent or ionic bonds connect the constituents with each other.

To connect the inorganic nanomaterials to the organic moiety in hybrid materials by strong covalent or ionic interactions, reactive organic groups have to be attached onto the surface of inorganic component. There are two main strategies for the preparation of organically

modified nanoparticles. The organic groups can either be grafted to preformed nanoparticles, “post synthesis functionalization”^[45] or introduced during the nanoparticles synthesis “in-situ functionalization”.^[46] While former has the advantage of offering a means to alter the interfacial properties without affecting the bulk characteristics of materials, the significance of the latter method lies in the self-limiting organization process of the inorganic and organic building blocks, where organic ligand controls, the growth, size and crystallinity of nanomaterials.

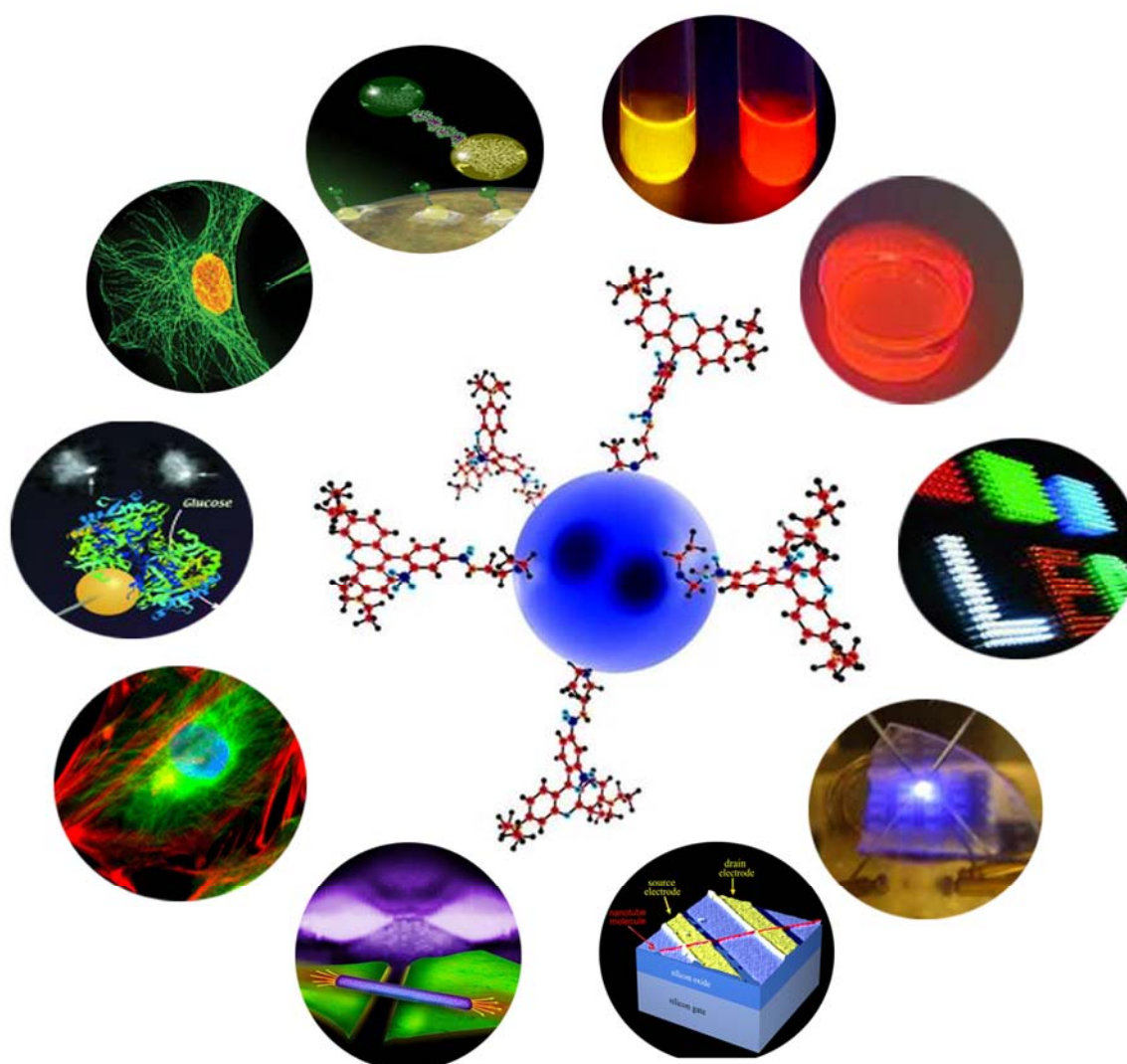


Figure 1.5. Use of functionalized nanoparticles in various fields of nanotechnology

A huge variety of neutral or charged semiconductor metal oxide nanoparticles are known and there are established routes for their synthesis. The valence requirements of the surface atoms

are satisfied by the bonding of terminal or bridging O⁻ or OH groups. These surface groups must be used to attach suitable organic groups to the surface of nanoparticles.

One major approach of surface functionalization on silica particles is using alkoxy silane compounds. Through the condensation reaction between the silanol group (Si-OH) of the silica surface and the alkoxy silane compounds, organic functional groups are introduced onto the surface of silica particles.

However, this method of surface functionalization has some drawbacks accompanied by this reaction route. First, some silanol groups of the alkoxy silane compounds might remain in the product owing to the incompleteness of the dehydration reaction. These silanol groups are highly reactive and might cause further condensation reactions during the period of storage and usage of the formed nanocomposites. Secondly the high cost of the alkoxy silane compounds also limited their practicability in mass production but still this method can be successfully employed for metal oxides like SiO₂, Fe₂O₃, and ZrO₂.^[47] In metal oxides particulate in nanocrystallites, the metal atoms are hexacoordinated (octahedral) in the bulk, whereas they are pentacoordinated (square pyramidal) at the surface. Ene diol ligands such as dopamine (DA) and catechol have a large affinity for these undercoordinated surface sites, restoring the metal atoms to the octahedral coordination and forming irreversible ligand-to-particle charge-transfer complexes.^[45,48,49] In these hybrid structures localized orbitals of surface attached ligands are electronically coupled with the delocalized electron levels from the conduction band of a semiconductor. As a consequence of this conformation, absorption of light by the metaloxide dopamine system yields to the excitation of electrons from the chelating ligands directly into the conduction band of metaloxide nanocrystallites, without transitioning through the ene diol excited state. The above strategy can also be successfully employed by many groups to achieve post modification of semiconductor metaloxides like TiO₂, SiO₂, Fe₂O₃, and ZrO₂.^[45,50,51,52]

The dative bonds, often used to modify the metal oxides nanoparticles are not suitable for the stabilization of metal nanoparticles, because metal nanoparticles do not have pronounced Lewis- acidic properties i.e. (no empty coordination sites). Owing to the surface reactivity of metal atoms, these nanoparticles are often stabilized by some surface capping agents which can be replaced by other functional ligands. The most common, and general method for the synthesis of metal nanoparticles involves the reduction of metal compounds in the presence of stabilizing ligands or templates. Traditionally, the ligands that have been used to produce stable nanoparticles by reduction method are phosphines, thiols and amines.^[53,54,55] Block

copolymers or dendrimers have also been used to provide cavities within which the reduction of metal like gold compound can be carried out.^[56]

Carbon nanotubes are unique materials, which offer a variety of structural parameters for engineering their physical and chemical properties.^[57] They can be synthesized as single wall (SWNT) or multiple-wall nanotubes (MWNT). Especially, single-wall carbon nanotubes (SWNT)s have the unique characteristic of being either metallic or semi-conducting. These properties depend on the chirality and diameter of nanotubes. Functionalization of carbon nanotubes with organic molecules can be used to tune their physical and chemical properties. For example, depending on the pattern of hydrogen atom coverage, while a metallic armchair of SWNT can be transformed to a wide band gap semiconductor, a semiconducting zigzag tube may become a metal with very high state density. A free SWNT, which is normally nonmagnetic, becomes magnetic with unpaired spins upon the adsorption of oxygen molecules or specific transition metal atoms. A recent study demonstrates that a semiconducting zigzag tube becomes both, a magnetic and a highly conducting wire as a result of Ti coating.^[58] Functionalization of carbon nanotubes can be achieved easily by oxidizing the surface, which results in the formation of carboxylic groups on the surface of a nanotube. Using the reactive functional groups surface can be tailored easily. This method is useful to improve the physical properties of nanotubes like solubility but has very low impact on the electrical or mechanical properties of nanotubes. To address the question, the addition reactions on the surface of nanotubes are quite successful. This methodology enables the direct coupling of functional groups onto the conjugated carbon framework of the tubes. The required reactive species (atoms, radicals, carbenes, or nitrenes) are in general made available through thermally activated reactions, and small-diameter tubes are preferred as they show higher chemical reactivity due to their increased curvature.^[59,60] Other methods used to functionalize carbon nanotubes are derivatization of carbon nanotubes with metal containing molecular coordination complexes, fluorination followed by nucleophilic substitution and chemically induced exfoliation of larger tubular bundles into smaller aggregates.^[61]

The surface chemistry of chalcogenides is more difficult to tackle, whereas simple sulfides such as MX (Where M= Cd, Zn and X= S, Se) are still amenable to complexation (due to metal atoms with vacant coordination sites at the surface of the nanoparticles). Possible organic anchor groups for semiconductors such as CdSe or ZnS are provided by amines, oxides, and thiols.^[62] Layered chalcogenides are much more inert because of the sulfur lone

pairs pointing away from the surfaces, while the metal is sandwiched by the chalcogen layers and, therefore, hardly accessible for complexation by any ligands.

To conclude, nanomaterials, especially with functionalized surfaces, opens the door for the coming era of nanotechnology in various applied fields. By controlling the surface properties of nanomaterials such as interaction with different solvents, functionalization of ligands (biomolecules, polymers etc), one can apply these nanomaterials into other disciplines to get a mature and diverse stage of nanotechnology. Moreover there is an ever need to develop synthetic methods which are nature friendly. In this thesis, we introduce novel and facile methods for the synthesis, characterization, in-situ and post-functionalization of nanomaterials which can be used as raw materials in various interdisciplinary fields.

1.4. References

- [1] S. Ciraci, S. Dag, T. Yildirim, O. G. Ulseren, R. T. Senger, *J. Phys. Condens. Matter.* **2004**, *16*, R901-R960.
- [2] E. Katz, I. Willner, *Angew. Chem.* **2004**, *116*, 6166–6235. *Angew. Chem. Int. Ed.* **2004**, *43*, 6042–6108.
- [3] C. C. Chen, Y. C. Liu, C. H. Wu, C. C. Yeh, M. T. Su, Y. C. Wu, *Adv. Mater.* **2005**, *17*, 404-407.
- [4] M. I. H. Panhuis, S. Gowrisanker, D. J. Vanesko, C. A. Mire, H. Jia, H. Xie, R. H. Baughman, I. H. Musselman, B. E. Gnade, G. R. Dieckmann, R. K. Draper, *Small* **2005**, *1*, 1-4.
- [5] C. M. Niemeyer, *Angew. Chem.* **2001**, *113*, 4254-4287. *Angew. Chem. Int. Ed.* **2001**, *40*, 4128-4158.
- [6] A. Ahmad, P. Mukherjee, D. Mandal, S. Senapati, M. I. Khan, R. Kumar, M. Sastry, *J. Am. Chem. Soc.* **2002**, *124*, 12108-12109.
- [7] R. Y. Sweeney, C. Mao, X. Gao, J. L. Burt, A. M. Belcher, G. Georgiou, B. L. Iverson, *Chemistry and Biology* **2004**, *11*, 1553–1559.
- [8] V. Bansal, D. Rautaray, A. Ahmad, M. Sastry, *J. Mater. Chem.* **2004**, *22*, 3303-3305.
- [9] V. Bansal, D. Rautaray, A. Bharde, K. Ahire, A. Sanyal, A. Ahmad, M. Sastry, *J. Mater. Chem.* **2005**, *26*, 2583-2589.
- [10] H. C. Schröder, S. P. Ottstadt, V. A. Grebenjuk, S. Engel, I. M. Müller, W. E. G. Müller, *Genomics* **2005**, *85*, 666-678.
- [11] R. Lovley, J. F. Stolz, G. L. Nord, E. J. F. Phillips, *Nature* **1987**, *330*, 252-254.
- [12] P. Philse, D. Maas, *Langmuir* **2002**, *18*, 9977-9984.
- [13] N. Kröger, R. Deutzmann, M. Sumper, *Science* **1999**, *286*, 1129-1133.
- [14] J. Milligan, F. M. M. Morel, *Science* **2002**, *297*, 1848-1850.
- [15] U. B. Sleytr, P. Messner, D. Pum, M. Sara, *Angew. Chem.* **1999**, *111*, 1098-1120. *Angew. Chem. Int. Ed.* **1999**, *38*, 1034-1054.
- [16] R. Joerger, T. Klaus, C. G. Granqvist, *Adv. Mater.* **2000**, *12*, 407-409.
- [17] T. Klaus, R. Joerger, E. Olsson, C. G. Granqvist, *Proc. Nat. Acad. Sci. USA* **1999**, *96*, 13611-13614.

- [18] T. K. Joerger, R. Joerger, E. Olsson, C. G. Granqvist, *Trends. Biotech.* **2001**, *19*, 15-20.
- [19] B. Nair, T. Pradeep, *Crystal Growth & Design* **2002**, *4*, 293-298.
- [20] S. S. Shankar, A. Rali, B. Ankamwar, A. Singh, A. Ahmad, M. Sastry, *Nature Mater.* **2004**, *3*, 482-488.
- [21] R. Wetherbee, *Science* **2002**, *298*, 547-547.
- [22] N. Kröger, R. Deutzmann, M. Sumper, *Science* **1999**, *286*, 1129-1132.
- [23] N. Kröger, R. Deutzmann, C. Bergsdorf, M. Sumper, *Proc. Nat. Acad. Sci. USA* **2000**, *97*, 14133-14138.
- [24] W. E. G. Müller, *Silicon Biomineralization*, Progress in Molecular and subcellular Biology.
- [25] W. E. G. Müller, A. Krasko, G. Penneç, H. C. Schröder, *Microscopy Research and Technique* **2003**, *62*, 368-377.
- [26] W. E. G. Müller, M. Rothenberger, A. Boreiko, W. Tremel, A. Reiber, H. C. Schröder, *Cell and Tissue Research* **321**, 285-297.
- [27] K. Shimizu, J. Cha, G. D. Stucky, D. E. Morse, *Proc. Nat. Acad. Sci. USA* **1998**, *95*, 6234-6238.
- [28] J. N. Cha, K. Shimizu, Y. Zhou, S. C. Christiansen, B. F. Chemlka, G. D. Stucky, D. E. Morse, *Proc. Natl. Acad. Sci. USA* **1999**, *96*, 361-365.
- [29] A. Krasko, B. Lorenz, R. Batel, H. C. Schröder, I. M. Müller, W. E. G. Müller, *Eur. J. Biochem.* **2000**, *267*, 4878-4887.
- [30] W. E. G. Müller, A. Borejko, D. Brandt, R. Osinga, H. Ushijima, B. Hamer, A. Krasko, C. Xupeng, I. M. Müller, H. C. Schröder, *FEBS Journal* **2005**, *272*, 3838-3852.
- [31] Y. Zhou, K. Shimizu, J. N. Cha, G. D. Stucky, D. E. Morse, *Angw. Chem.* **1999**, *111*, 825-827. *Angw. Chem. Int. Ed.* **1999**, *38*, 780-782.
- [32] D. Kisailus, M. Najarian, J. C. Weaver, D. E. Morse, *Adv. Mater.* **2005**, *17*, 1234-1239.
- [33] J. N. Cha, G. D. Stucky, D. E. Morse, T. J. Deming, *Nature* **2000**, *403*, 289-292.
- [34] M. K. Roth, Y. Zhou, W. Yang, D. E. Morse, *J. Am. Chem. Soc.* **2005**, *127*, 325-330.
- [35] J. L. Sumerel, W. Yang, D. Kisailus, J. C. Weaver, J. H. Choi, D. E. Morse, *Chem. Mater.* **2003**, *15*, 4804-4809.

- [36] D. Kisailus, J. H. Choi, J. C. Weaver, W. Yang, D. E. Morse, *Adv. Mater.* **2005**, *17*, 314-318.
- [37] M. N. Tahir, P. Theato, W. E. G. Müller, H. C. Schröder, A. Janshoff, J. Zhang, J. Huth, W. Tremel, *Chem. Comm.* **2004**, 2848-2849.
- [38] M. N. Tahir, P. Theato, W. E. G. Müller, H. C. Schröder, A. Borejko, S. Faiß, A. Janshoff, J. Huth, W. Tremel, *Chem. Comm.* **2005**, 5533-5535.
- [39] R. Xie, U. Kolb, J. Li, T. Basche, A. Mews, *J. Am. Chem. Soc.* **2005**, *127*, 7480-7488.
- [40] M. Grätzel, *Nature* **2001**, *414*, 338-344.
- [41] L. Dai, P. He, S. Li, *Nanotechnology* **2003**, *14*, 1081-1097.
- [42] A. N. Goldstein, *Handbook of Nanophase Materials* **1997**, (New York: Dekker)
- [43] B. Z. Tang, H. Xu, *Macromolecules* **1999**, *32*, 2569-2576.
- [44] H. Duan, M. Kuang, D. Wang, D. G. Kurth, H. Möhwald, *Angew. Chem.* **2005**, *117*, 1745–1748. *Angew. Chem. Int. Ed.* **2005**, *44*, 1717-1720.
- [45] N. M. Dimitrijevic, Z. V. Saponjic, B. M. Rabatic, T. Rajh, *J. Amer. Chem. Soc.* **2005**, *127*, 1344-1345.
- [46] M. Niederberger, G. Garnweitner, F. Krumeich, R. Nesper, H. Cölfen, M. Antonietti, *Chem. Mater.* **2004**, *16*, 1202-1208.
- [47] G. Carrot, D. R. Houze, A. Pottier, P. Degee, J. Hilborn, P. Dubois, *Macromolecules* **2002**, *35*, 8400-8404.
- [48] T. Rajh, O. Poluektov, A. A. Dubinski, G. Wiederrecht, M. C. Thurnauer, A. D. Trifunac, *Chem. Phys. Lett.* **2001**, *344*, 31-39.
- [49] T. Rajh, L. X. Chen, K. Lukas, T. Liu, M. C. Thurnauer, D. M. Tiede, *J. Phys. Chem. B* **2002**, *106*, 10543-10552.
- [50] C. Xu, K. Xu, G. Gu, R. Zheng, H. Liu, X. Zhang, Z. Guo, B. Xu, *J. Am. Chem. Soc.* **2004**, *126*, 9938-9939.
- [51] H. Gu, Z. Yang, J. Gao, C. K. Chang, B. Xu, *J. Am. Chem. Soc.* **2005**, *127*, 34-35.
- [52] M. N. Tahir, M. Eberhardt, P. Theato, S. Faiß, A. Janshoff, T. Gorelik, U. Kolb, W. Tremel, *Angew. Chem.* **2006**, *118*, 922-926. *Angew. Chem. Int. Ed.* **2006**, *45*, 908-912.
- [53] W. W. Weare, S. M. Reed, M. G. Warner, J. E. Hutchison, *J. Am. Chem. Soc.* **2000**, *122*, 12890-12891.
- [54] M. Brust, M. Walker, D. Bethell, D. J. Schiffrin, R. Whyman, *Chem. Comm.* **1994**, 801-802.

- [55] L. O. Brown, J. E. Hutchison, *J. Am. Chem. Soc.* **1999**, *121*, 882-883.
- [56] Z. B. Shifrina, M. S. Rajadurai, N. V. Firsova, L. M. Bronstein, X. Huang, A. L. Rusanov, K. Muellen, *Macromolecules* **2005**, *38*, 9920-9932.
- [57] A. Hirsch, *Angew. Chem.* **2002**, *114*, 1933-1939. *Angew. Chem. Int. Ed.* **2002**, *41*, 1853-1859.
- [58] S. Dag, E. Durgun, S. Ciraci, *Phys. Rev. B* **2004**, *69*, 121407(R)-4.
- [59] J. L. Bahr, J. M. Tour, *J. Mater. Chem.* **2002**, *12*, 1952-1958.
- [60] C. A. Dyke, J. M. Tour, *Chem. Eur. J.* **2004**, *10*, 812-817.
- [61] V. N. Khabashesku, W. E. Billups, J. L. Margrave, *Acc. Chem. Res.* **2002**, *35*, 1087-1095.
- [62] I. Potapova, R. Mruk, S. Prehl, R. Zentel, T. Basche, A. Mews, *J. Am. Chem. Soc.* **2003**, *125*, 320-321.

2. Monitoring the Formation of Biosilica Catalyzed by Histidin-Tagged Silicatein

2.1. Introduction

Nanoscale control of polymerization of silicon and oxygen determines the structures and properties of a wide range of siloxane-based materials.^[1] These materials typically require high temperatures, high pressures and the use of caustic chemicals.^[2] In comparison, biological systems can synthesize siloxane-based materials at ambient temperatures, pressures and produce an amazing diversity of precisely nanostructured morphologies.^[3] Biosilicification in diatoms^[4], sponges^[5] and grasses^[6] represents typical examples in this context. The studies of biosilicification have led to the isolation of proteins that facilitate silica formation *in vivo*, in particular, silaffins in diatoms^[3] and silicateins in sponges^[5,7,8,9] have been studied and identified as constituents of biosilica (silica formed by proteins) showing an accelerated silica formation from monosilicic acid solution *in vitro*.^[8] To verify the specificity and significance of the above proteins in biosilicification,

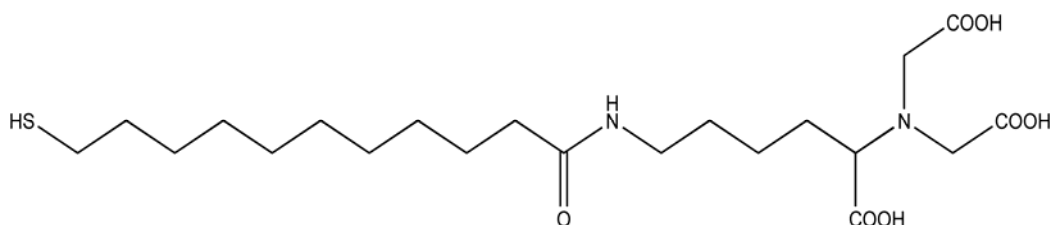


Figure 2.1. Nitrilotriacetic acid (NTA) terminated alkanethiol.

a variety of synthetic polymers including polypeptides and di-block co-polypeptides have been investigated for their role in silicification in solution.^[8,10,11] The process of silica formation in marine sponges is thought to be mediated by a family of catalytically active structure-directing enzymes, the so-called silicateins. It has been shown that silicateins facilitate the formation of SiO₂ in solution at neutral pH using tetraethoxysilane (TEOS) as a monomer.^[5,7,9] Whereas no polymerization of TEOS was observed at neutral pH in the absence of silicatein.^[12] To understand the operation of silicatein and the formation of the

resulting silica structures at the molecular level by means of surface methods, we present the immobilization of silicatein which was isolated from marine sponge *suberites domuncula*.

In order to be able to immobilize silicatein onto surfaces we synthesized a chelator alkanethiol based on the idea that silicatein expresses a short affinity sequence of histidines (histidine-tag) that is capable to bind metal ion complexes such as nitrilotriacetic acid (NTA). It's known that NTA, when complexed with Ni^{2+} , selectively binds proteins whose sequence is terminated with a sequence of histidines.^[13] The structure of the NTA-terminated alkanethiol, whose synthesis was adopted from similar structures reported recently,^[13] is shown in Figure 2.1. The self-assembled monolayer formation of the chelating alkanethiol NTA and the immobilization of the protein to the gold (111) surface were monitored using the surface sensitive optical technique of surface plasmon resonance (SPR). The plasmon spectra were recorded against ethanol on bare gold slides, after self-assembly of chelating alkanethiol NTA and after immobilization of silicatein on the gold surfaces, both Ni^{2+} coordinated as well as without coordination of Ni^{2+} .

2.2. Results and discussion

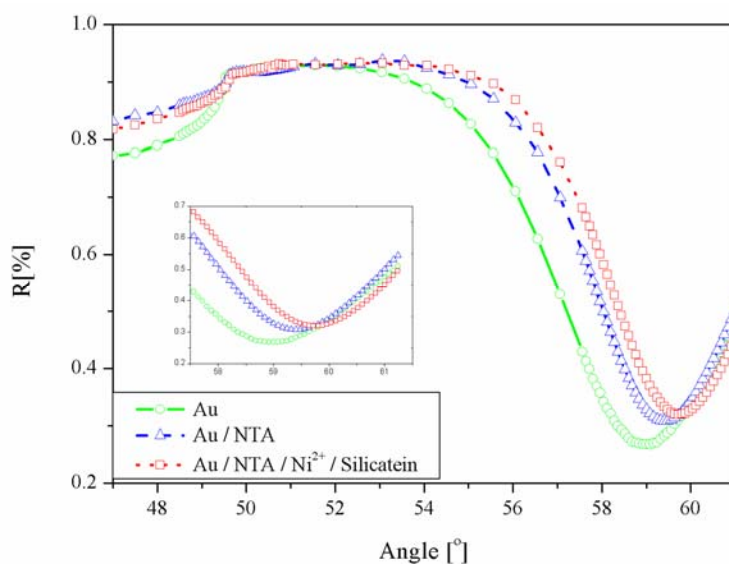


Figure 2.2. SPR curves of gold (circles), NTA alkanethiol on gold (triangles) and immobilized silicatein thereon (squares).

Figure 2.2 displays the corresponding SP spectra of all these experiments and a closer view of the corresponding minima reflectivity angle. The shifts of the plasmon curves were calculated, corresponding to angular changes of 0.420° (monolayer of NTA alkanethiol on bare gold) and 0.720° (silicatein on Ni^{2+} coordinated surface). In a separate experiment immobilization of silicatein without Ni^{2+} could not be detected, supporting the chelating efficiency of histidine-tags in the presence of Ni^{2+} .

These shifts in surface plasmon resonance angle were converted by complex Fresnel calculations to an average thickness of monolayer of NTA alkanethiol and silicatein layer assuming a refractive index of $n=1.5$ for both layers. NTA alkanethiol resulted in a 1.6 nm thick film, while silicatein immobilization increased the thickness by 2.8 nm, which matches the theoretical diameter of 3.0 nm for a protein with a molecular weight of 24000 Dalton.

In order to confirm that the silicatein was immobilized on the surfaces functionalized with NTA alkanethiol SAMs, direct evidence by scanning force microscopy (SFM) was provided.

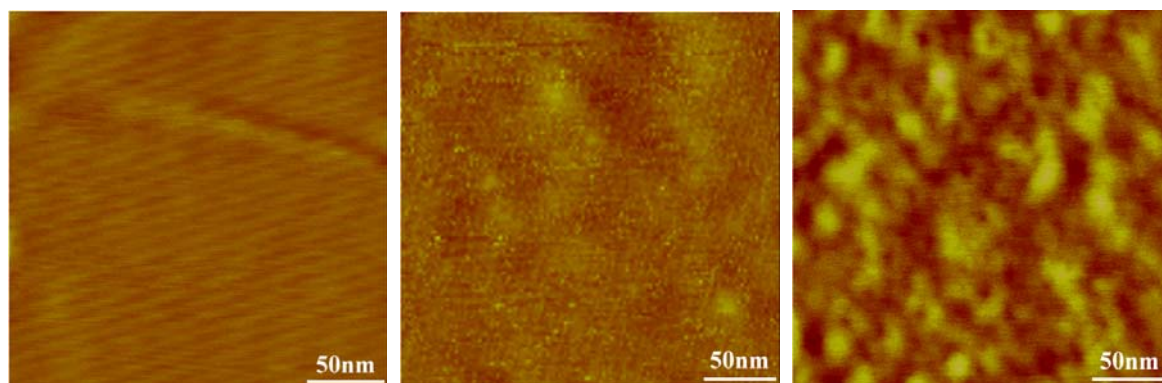


Figure 2.3. SFM height pictures of a) gold (111) surface, b) NTA alkanethiol on gold and c) immobilized silicatein (same scale for all images).

Figure 2.3a-c show the SFM height images obtained in intermediate contact mode of Au (111) crystal surface, the NTA monolayer surface, and the surface of immobilized silicatein film, respectively. We have no intention to show the observation of the atomic structures of these three surfaces using SFM, however, the height and roughness analysis of the topologies of these surfaces supported strong evidence that the modification of Au (111) by NTA alkanethiol self-assembled monolayers (SAMs), and subsequently the immobilization of

silicatein on the surfaces of NTA alkanethiol SAMs had both taken place. The roughness of Au (111) surface was 0.590 nm, which is rather flat, but the roughnesses of the NTA SAMs

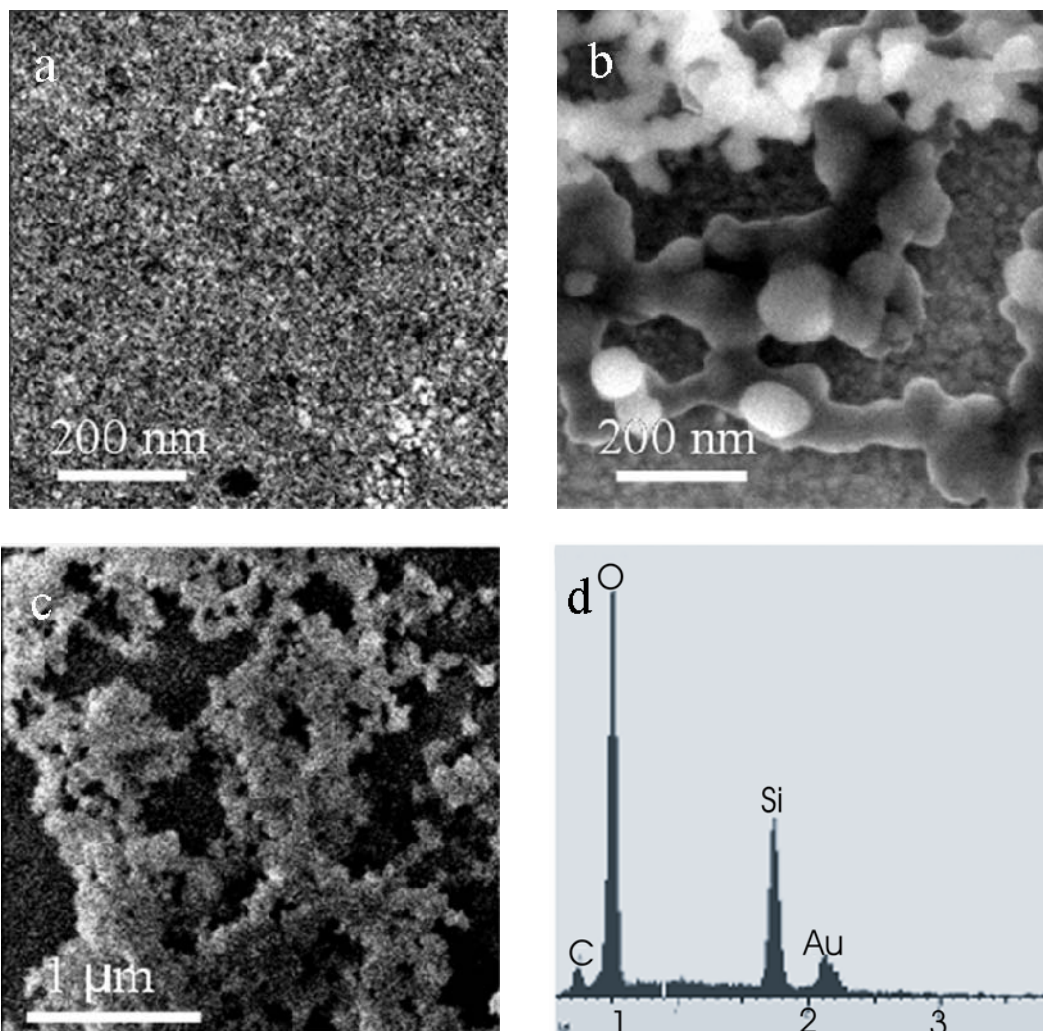


Figure 2.4. SEM images of silicization onto surfaces functionalized with NTA alkanethiol without Ni^{2+} (a) and NTA alkanethiol with Ni^{2+} chelating silicatein (b, c). No observable formation of SiO_2 occurred on NTA alkanethiol modified surfaces (a). In contrast, Ni^{2+} chelated silicatein immobilization onto NTA alkanethiol surfaces induced the formation of SiO_2 (b,c), as evidenced by the EDX-spectrum (d).

surface and the silicatein film surface were 1.415 and 2.384, separately, which were rougher compared with Au (111) plane.

The increase of the roughness illustrates that the uncoated gold surfaces is atomically flat, but the NTA-coated gold samples and the silicatein films are only molecularly flat. Though difficult to define fully, we believe that the SFM image in Figure 2.3c arises from the surface of an immobilized silicatein film chemisorbed on the NTA monolayers.

In order to confirm the activity of silicatein through the ability to precipitate silica on the surface, we performed two sets of experiments. One, using gold surface modified with NTA or NTA with Ni²⁺ and a second, with gold surfaces functionalized with immobilized silicatein. Under these similar sets of conditions for both experiments, we could find structured silica only on the silicatein immobilized surfaces, using SEM characterisation, as shown in Figures 2.4(b and c). Figure 2.4a shows the results after having performed the precipitation of silica on the surface modified by NTA thioalkane only. Clearly, no formation of silica was observed. Furthermore, the surface became black when exposed to the electron beam in the scanning electron microscope which indicated the presence of organic species, such as NTA alkanethiol, that decomposed upon exposure to the electron beam. On surfaces functionalized with silicatein nanospheres of silica had been precipitated (Figures 2.4(b and c)). Structures of interconnected nanospheres with a diameter about 70-300 nm were observed. Figure 2.4d shows the energy dispersive x-ray (EDX) analysis spectrum of the material synthesized on the surface, which give evidence that it consists of silica. Analyzing the EDX spectrum of the surface without immobilized silicatein during the silicization process showed that no silica was formed here. The formation of interconnected silica spheres in the vicinity of surface bound protein indicates that the active site of the immobilized protein is oriented towards the solution and that the reaction is diffusion controlled. This is corroborated by the silicification of TEOS with silicatein used as an additive in solution, which resulted in no precipitation of SiO₂ on NTA functionalized surfaces, as can be seen in the supporting information. It is obvious from the SEM pictures shown in Figures 2.4(b and c) that the coverage of the surface with silica is heterogeneous. About 70% of the surface was covered with silica structures. Whether this is due to the limited reaction time of 8 hours or an imperfect homogeneous immobilization of the silicatein is the subject of ongoing investigations.

2.3. Conclusion

To conclude, we could present a novel NTA terminated alkanethiol which can be successfully self-assembled onto gold surfaces. These functionalized surfaces could immobilize histidine-tagged silicatein using the efficient chelating properties with Ni^{2+} . The results presented here demonstrate that silicatein, previously shown active for catalysing and structurally directing the polycondensation of silicon alkoxides in solution, when immobilized onto surfaces is also capable of catalysing and templating the polycondensation of monomeric silicon alkoxides to form silica structures on surfaces.

2.4. Experimental

Gold films (100nm) were coated on freshly cleaved mica surfaces using (Balzer BAE 250) at rate of 0.2 nm/s and under pressure of 5×10^{-6} mbar. Film thickness was monitored by a quartz crystal oscillator. After evaporation, the mica supported gold films were placed on a stainless steel plate which was kept inside a glass tube of a tube furnace. The gold films were annealed at 600°C under a constant flow of N₂ for 10 mint. Finally the gold films were quenched and rinsed with methanol and dried with N₂. Gold (111) coated glass substrates were placed in an ethanolic solution of NTA thioalkane (3 mmol) for a period of 12 hours. After self assembly, the surfaces were washed with ethanol to remove unbound NTA. The quality of monolayer was ascertained by SPS and AFM. To immobilize the protein, Ni^{II} was bound to NTA group, the gold slides functionalized with NTA thioalkane were treated with 1 mmol NaOH for 10 mint, followed by dipping of slides in a solution of NiSO₄ (40 mmol) for 1 hour. Then slides were taken out, washed with (150 mmol) solution of NaCl and deionized water and dried in a stream of N₂. Then silicatein solution (30 nmol) in MOPS buffer was introduced to the Ni^{II} bound SAMs for 1 hour. Then slides were washed with MOPS buffer and deionized water to get rid of unbound protein and dried by N₂. The immobilization of silicatein was monitored by AFM, SPR. The Silicification from monomeric TEOS was carried out at room temperature and neutral pH. The silicatein immobilized substrates were placed facing down into a reaction vessel containing 200 ml of TEOS (4.5 mmol, 135 ml) and MOPS buffer (75 ml). The reaction vessel was transferred into a desiccator. The polymerization was stopped after 6 hrs. Then substrates were washed with MOPS and deionized water and dried by stream of N₂.

For SPR and SEM glass slides (3.5 X 2.5 cm) were used. Quartz crystal with evaporated gold electrode was used as substrate for QCM measurements. Quartz crystal evaporated with gold and glass slides were cleaned with aq.NH₃ / H₂O₂ / H₂O (1:1:5) for 10 mint at 80 °C, washed with water and isopropanol and dried in stream of N₂. These glass slides were coated with gold using a Balzer BAE 250, vacuum coating unit under pressure of less than 5×10^{-6} hPa, typically depositing 50 nm of gold after first depositing 2 nm of Cr. The slides were exposed to NTA thiol (1) solution (1 mmol) for 12 hours.

Scanning Force Microscopy

Samples were imaged at room temperature with a commercial SFM (Nanoscope IIIa, Digital Instruments, Santa Barbara, California) employing TappingMode™ using rectangular silicon cantilevers (Nanosensors, 125 μm long, 30 μm wide, 4 μm thick) with an integrated tip, a nominal spring constant of 42 N m⁻¹, and a resonance frequency of 330 kHz. To control and enhance the range of the attractive interaction regime the instrument was equipped with a special active feedback circuit, called Q-control (Nanoanalytics, Germany). The quality factor Q of this oscillating system is increased up to one order of magnitude. As a consequence, the sensitivity and lateral resolution are enhanced, allowing us to prevent the onset of intermittent repulsive contact and thereby to operate the SFM constantly in the attractive interaction regime.

SPR Experimental

SPR measurements were performed in the Kretschmann configuration against ethanol. Optical coupling was achieved with a LASFN 9 prism, n = 1.85 at λ = 632.8 nm and index matching fluid n = 1.70 between prism and the BK270 glass slides. The plasmon was excited with P-polarized radiation using a He/Ne laser (632.6 nm, 5 mW).

Synthesis of chelating thioalkane NTA

Synthesis of N^α, N^α-Bis(tert-butyloxycarbonyl)methyl]-N^ε-benzyloxy carbonyl-L-Lysine tert-butyl ester.

2140 mg (5.74 mmol) of N^ε-benzyloxycarbonyl-L-Lysine tert-butyl ester hydrochloride, 5.32 ml of triethylamine and 12.8 g (8.25 mmol) of bromoacetic acid tert-butyl ester was stirred in 80 ml of DMF for four days at 50°C. The solvent and excess of bromoacetic acid tert-butyl ester was evaporated in vacuum and remaining very thick oil was extracted 4 times with hexane. The combined organic phases were combined and solvent was removed in rotary vacuum evaporator. The purification was carried out by column chromatography (pet.ether : MeOH 1000 : 1). Yield: 3237 mg (71%) ¹H NMR (400 MHz, CDCl₃): δ=1.43 (s,18H), δ=1.45 (s,9H), δ=1.50 (m,4H), δ=1.65 (m, 2 H), δ=3.19 (m, 2 H), δ=3.33 (t,1 H), δ=3.48 (dd, 4H), δ= 5.08 (s,2 H), δ=7.35 (m,5 H),

Synthesis of N^α, N^α-Bis(tert-butyloxycarbonyl)methyl]-L-Lysine tert-butyl ester

150 mg of Pd/C (10%) was suspended in 120 ml of dried ethanol. The N^α, N^α-Bis(tert-butyloxycarbonyl)methyl]-N^ε-benzyloxy carbonyl-L-Lysine tert-butyl ester (1800 mg) was added and was hydrogenated at 30 °C temperature and normal pressure for 4 hours. The catalyst was filtered off and solvent was removed in vacuum. Yield: 1220 mg (91%) ¹H NMR (400 MHz, CDCl₃): δ=1.41 (s,18H), δ=1.43 (s,9H), δ=1.21 (q,2H), δ=1.65 (m, 2 H), δ=2.98 (t, 2 H), δ=3.39 (t,1 H), δ=3.67 (dd, 4H), δ=1.84 (bm, 2H),

Synthesis of 11-(Acetyl Thio) undecanoic acid

The 11-bromoundecanoic acid (954 mg) was dissolved in 20 ml of dried DMF at 0 °C. After that 1172 mg of potassium thioacetate was added at above mention temperature. The deep red mixture was stirred for 30 mint at room temperature, diluted with CH₂Cl₂ (60 ml) and washed three times with water. The organic phase was dried over MgSO₄ and solvent was coevaporated with toluene. The light yellow crude product was purified by recrystallization in pet. Ether. Yield: 824 mg (88%) ¹H NMR (400 MHz, CDCl₃): δ=2.33 (s,3H), δ=2.86 (t,2H), δ=1.53-1.67 (m,4H), δ=1.26-1.36 (m, 4 H), δ=2.37 (t, 2 H),

Synthesis of 6-(11-acetyl sulfanyl-undecanoylamino)-2-(bis-tert-butyloxy carbonyl methyl-amino)-hexanoic acid tert-butyl ester

The 11-(Acetyl Thio) undecanoic acid (693 mg 2.66 mmol) were dissolved in 55ml of absolute CH₂Cl₂ and 550 mg of dicyclohexylcarbodiimide (DCC), 308 mg of N-hydroxy succinimide and 41 mg of 4-dimethylaminopyridine in 27 ml of acetone were added. The solution was stirred for 4 hours at room temperature, the precipitated urea was filtered off and (1150 mg 2.66 mmol) of N^α, N^α-Bis(tert-butyloxycarbonyl)methyl]-L-Lysine tert-butyl ester and 1065 μl of triethylamine in 50 ml of absolute CH₂Cl₂ were added. The reaction was stirred for 5 hours. Thereafter the solvent was removed in vacuum. The product was purified by re-crystallization in acetone. Yield: 1526 mg 85% ¹H NMR (400 MHz, CDCl₃): δ=3.69 (dd, 4H), δ=3.43 (t, 1H), δ=3.11 (m,2H), δ=2.81 (m, 2 H), δ=2.63 (t, 2 H), δ=2.30 (s,3 H), δ=1.84 (m, 2H), δ=1.50-1.73 (m, 4H), δ= 1.42-1.44 (bs, 27H), δ=1.20-1.37 (m, 6H)

Synthesis of 2-[N^α-N^α-bis(hydroxycarbonylmethyl)-amino-6-[11-Acetylthio-undecanoyl amino]-hexanoic acid.

1200mg (1.78 mmol) of Synthesis of 6-(11-acetyl sulfanyl-undecanoylamino)-2-(bis-tert-butyloxy carbonyl methyl-amino)-hexanoic acid tert-butyl ester was dissolved in 180ml of chloroform/trifouroacetic acid (5:1). The reaction was stirred for 20 hours at room temperature, extracted twice with 1N NaOH. The solvent was evaporated and product was

crystallized in acetone. Yield: 721 mg 80.76% ^1H NMR (400 MHz, CDCl_3): $\delta=3.67$ (dd, 4 H), $\delta=3.26-3.46$ (bm, 6 H), $\delta=2.28$ (t, 2 H), $\delta=2.12$ (s, 3 H), $\delta=1.84$ (m, 2 H), $\delta=1.57-1.70$ (bm, 6 H), $\delta=1.04-1.34$ (m, 6H)

Synthesis of 2-[N $^\alpha$ -N $^\alpha$ -bis(hydroxycarbonylmethyl)-amino-6-[11-mercapto-undecanoyl amino]-hexanoic acid.

The compound 2-[N $^\alpha$ -N $^\alpha$ -bis(hydroxycarbonylmethyl)-amino-6-[11-Acetylthio-undecanoyl amino]-hexanoic acid (690 mg 1.36 mmol) was dissolved in 50ml of CH_2Cl_2 and solution was purged with N_2 . then 355 μl of HCl was added and mixture was refluxed under N_2 atmosphere for 5 hours. Then product was concentrated and washed with 18.2 Ω water until neutral. The organic phase was dried over MgSO_4 and evaporated. The product was purified by acetone recrystallization. Yield: 600mg 95%. ^1H NMR (400 MHz, CDCl_3): $\delta=3.74$ (dd, 4 H), $\delta=3.22$ (t, 2 H), $\delta=2.28$ (t, 2 H), $\delta=2.55$ (t, 2 H), $\delta=1.84$ (m, 2 H), $\delta=1.20-1.48$ (m, 4 H), $\delta=1.55-1.70$ (m, 4H)

2.5. References

- [1] E. Morse, *Tibtech.* **1999**, *17*, 230-232.
- [2] S. H. Tolbert, A. Firouzi, G. D. Stucky, B. F. Chmelka, *Science* **1997**, *278*, 264-268.
- [3] N. Kröger, R. Deutzmann, M. Sumper, *Science* **1999**, *286*, 1129-1132.
- [4] R. Wetherbee, *Science* **2002**, *298*, 547-547.
- [5] W. E. G. Müller, A. Krasko, G. L. Pennec, R. Steffen, M. S. A. Ammar, M. Wiens, I. M. Müller, H. C. Schröder, *Progress Molec. Subcell. Biol.* **2003**, *33*, 195-221.
- [6] A. Lux, M. Luxova, S. Morita, J. Abe, S. Inanaga, *Can. J. Bot./Rev. Can. Bot.* **1999**, *77*, 955-960.
- [7] K. Shimizu, J. Cha, G. D. Stucky, D. E. Morse, *Proc. Natl. Acad. Sci. USA* **1998**, *95*, 6234-6238.
- [8] N. Kröger, R. Deutzmann, C. Bergsdorf, M. Sumper, *Proc. Natl. Acad. Sci. USA* **2000**, *97*, 14133-14138.
- [9] Y. Zhou, K. Shimizu, J. N. Cha, G. D. Stucky, D. E. Morse, *Angew. Chem. Int. Ed. Engl.* **1999**, *38*, 779-782.
- [10] H. Menzel, S. Horstmann, P. Behrens, P. Bärnreuther, I. Krüger, M. Jahns, *Chem. Comm.* **2003**, 2994-2995.
- [11] L. L. Brott, R. R. Naik, D. J. Pikas, S. M. Kirkpatrick, D.W. Tomlin, P. W. Whitlock, S. J. Clarson, M. O. Stone, *Nature* **2001**, *413*, 291-293.
- [12] J. N. Cha, K. Shimizu, Y. Zhou, S. C. Christiansen, B. F. Chmelka, G. D. Stucky, D. E. Morse, *Proc. Natl. Acad. Sci. USA* **1999**, *96*, 361-365.
- [13] a) D. Kröger, M. Liley, W. Schiweck, A. Skerra, H. Vogel, *Biosensors & Bioelectronics* **1999**, *14*, 155-161. b) G. B. Sigal, C. Bamdad, A. Barberis, J. Strominger, G. M. Whitesides, *Anal. Chem.* **1996**, *68*, 490-497.

3. Formation of Layered Titania and Zirconia Catalyzed by Surface-Bound Silicatein

3.1. Introduction

Self-assembled monolayers (SAM) of alkanethiol derivatives on metal electrodes provide numerous possibilities for immobilising proteins.^[1] In the past few years, such devices have gained increasing interest in (nano)biotechnology. In particular, the current and potential importance of immobilized enzymes for the design and development of biosensors,^[2] bioelectronic systems,^[3] or biocatalytic cells^[4] has stimulated a large number of experimental studies in this field. Customising the catalytic functions and optimising the efficiencies of these systems represent a challenge in current research as they require a detailed characterization of the structural and functional properties of the active adlayers as well as of the dynamics of the processes involved.

In a preliminary report, we have demonstrated the formation of biosilica catalyzed by surface-bound histidine tagged silicatein.^[5] Silicatein in sponges has been identified as constituent of biosilica.^{[6],[7]} In this contribution we demonstrate that surface bound silicatein is not only capable of polycondensating biosilica, but is also significant for the synthesis of other metal oxides such as TiO₂^[8] and ZrO₂ using water stable alkoxide precursors such as [titanium bis-(ammonium-lactato)-dihydroxide],^[8] and anionic hexafluorozirconate (ZrF₆²⁻),^[9] resulting in the synthesis of oxide particles with a layered morphology at neutral pH and room temperature. TiO₂ is a wide-bandgap semiconductor with important applications in optoelectronics,^[10] photocatalysis,^[11] and as pigment in resin,^[12] solar cell^[13] and molecular sieves^[14] while zirconia attracts the nanotechnologist because of its superb electronic properties with application as a piezoelectric,^[15] electrooptic^[16] and dielectric material.¹⁷ Synthesis of these oxides proceeds by hydrolysis of suitable metal complexes under extreme pH and temperature conditions. A biological synthesis of titania and zirconia would thus help mitigate the shortcomings of chemical methods.

In order to immobilize silicatein onto surfaces we designed a reactive ester polymer, poly(acetoxime methacrylate), which specifically reacts with primary amines.^[18] The gold surfaces were exposed to a cysteamine solution (3 mmol) for 12 hours followed by the reaction of the amine group with the reactive polymer.

This leads to a reactive thin film bound to cysteamine. The recombinant protein has a short affinity sequence of histidines (histidine-tag) that is capable to bind metal ion complexes such as nitrilotriacetic acid (NTA). Thus an ω -terminated NTA amine was chemisorbed on top of a soft reactive polymer thin film.^[18] The stepwise architecture of the self-assembly and immobilisation of His-tagged silicatein is shown in Figure 3.1.

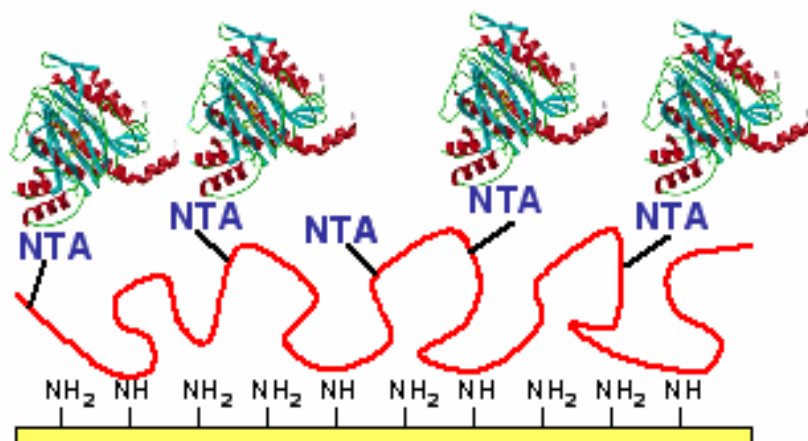


Figure 3.1. Immobilization of silicatein using cysteamine, a reactive ester polymer, and the NTA ligand.

This spacer layer decouples the protein from the surface and thus provides a hydrophilic layer (between the protein and the Au substrate) which establishes a water-containing sub-layer space, which reduces the hydrophobic influence of the metal surface.^[19]

The self-assembled monolayer formation of the cysteamine, polymer, NTA and silicatein immobilization to the gold (111) surface was monitored using the surface sensitive optical technique of surface plasmon resonance (SPR) spectroscopy. The plasmon spectra were recorded against water on bare gold slides, after self-assembly of cysteamine and polymer, NTA and after immobilization of silicatein on the surfaces by Ni^{2+} coordination. Fig. 3.2a displays the corresponding SPR spectra of all these experiments and the corresponding minima reflectivity angles.

3.2. Results and discussion

The shifts of the plasmon curves were calculated, corresponding to angular changes of 0.160° (monolayer of cysteamine and polymer on bare gold after quenching all unreacted active ester groups), 0.420° (NTA onto polymer) and 0.70° (silicatein on Ni^{2+} coordinated surface). In a

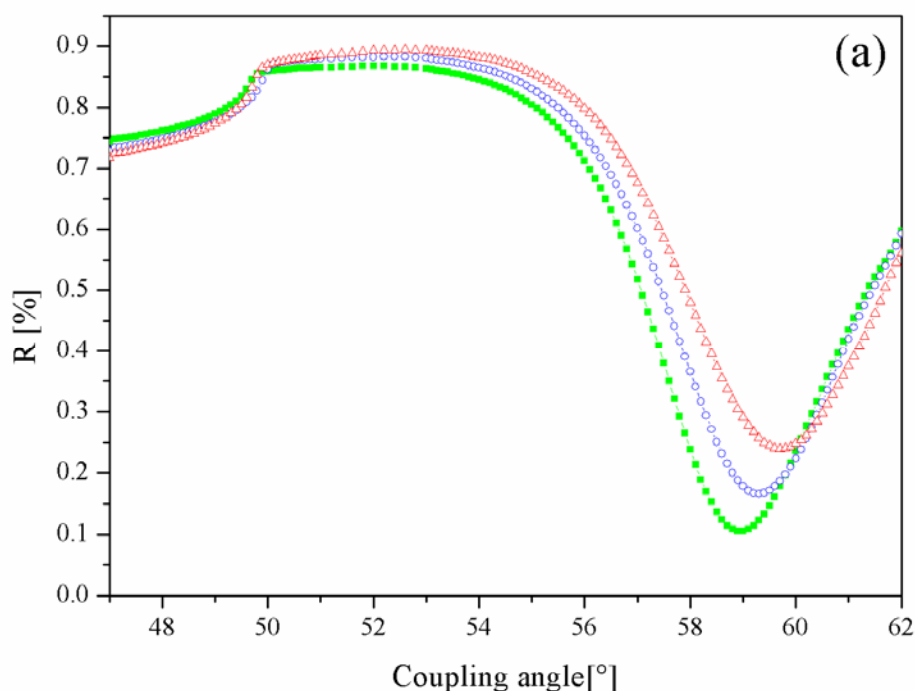


Figure 3.2a. SPR curves of cysteamine on gold (dots), polymer with NTA (open circles) and immobilized silicatein thereon (filled circles).

separate experiment immobilization of silicatein without Ni^{2+} could not be detected, supporting the chelating efficiency of histidine-tags with Ni^{2+} . These shifts in surface plasmon resonance angle were converted by complex Fresnel calculations to an average thickness of the monolayers of cysteamine and polymer, cysteamine polymer and NTA, and the immobilized silicatein layer assuming a refractive index of $n = 1.5$ for all layers.

For the cysteamine polymer we derived a surface thickness of 16 \AA , which increased to 32 \AA after NTA binding. Subsequent silicatein binding increased the thickness by 34 \AA which is close to the theoretical diameter of 30 \AA for a protein with a molecular weight of 24000 Dalton.

Fig. 3.2b compares the protein immobilization under specific and non-specific binding conditions. The solid line (lower trace) represents the non-specific binding in the absence of

Ni^{2+} ions. After protein addition a slight increase in thickness was observed. However, upon rinsing, any non-specifically bound protein could be washed away. In contrast, in the presence of Ni^{2+} ions chelated to the NTA linker specific binding was achieved (dashed line, upper trace). A strong increase in thickness was observed upon protein addition, which was stable even after thorough rinsing.

The fixation of the reactive polymer was proven by FT-IR reflectometry. Fig 3.3a shows the surface FT-IR spectra of the polymer functionalized cysteamine SAM on gold slides (dotted lines) and the polymer-bound NTA ligand (solid line).

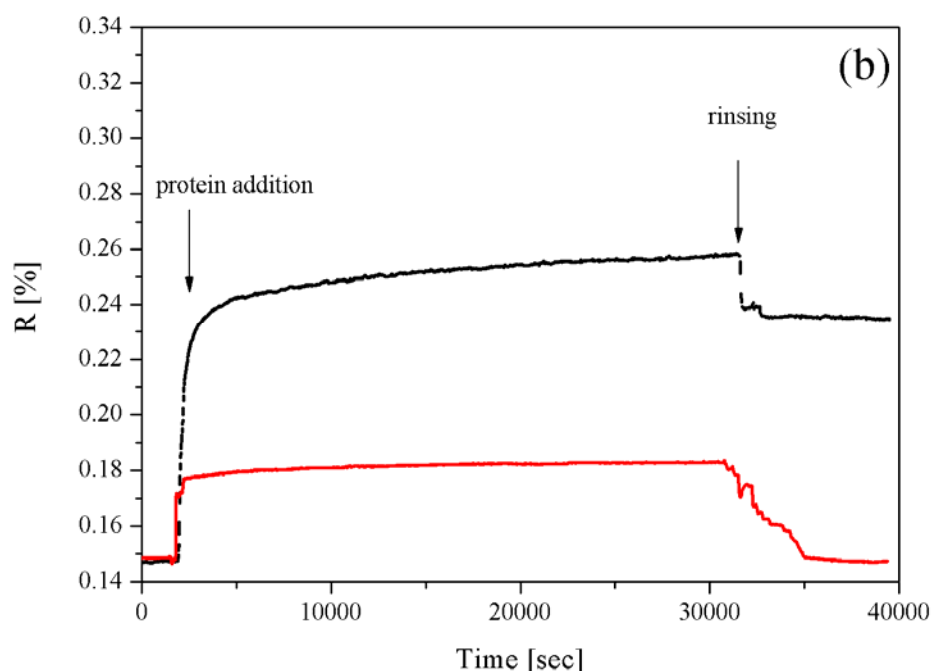


Figure 3.2b. Reflectivity plotted as a function of time in the absence (solid line) and presence (dotted line) of Ni^{2+} indicating the specific binding of the silicatein to the NTA linker.

Clearly, the carbonyl peak of the reactive ester can be seen at 1765 cm^{-1} as well as a vibration of the amide group at 1648 cm^{-1} . After binding the NTA ligand to the polymer layer the polymer layer was rinsed twice with concentrated ammonia solution in order to quench the unreacted acetoxyimide functional groups. The binding of the NTA ligand is demonstrated by the presence of two additional vibrations originating from the symmetric and asymmetric stretch of the carboxylate groups at 1597 cm^{-1} and 1400 cm^{-1} .^[20] Upon attachment of the protein to

the NTA ligand (as shown in the inset of Figure 3.3a the C=O vibrational bands broaden due to the multitude of amide groups present in the surface bound protein).

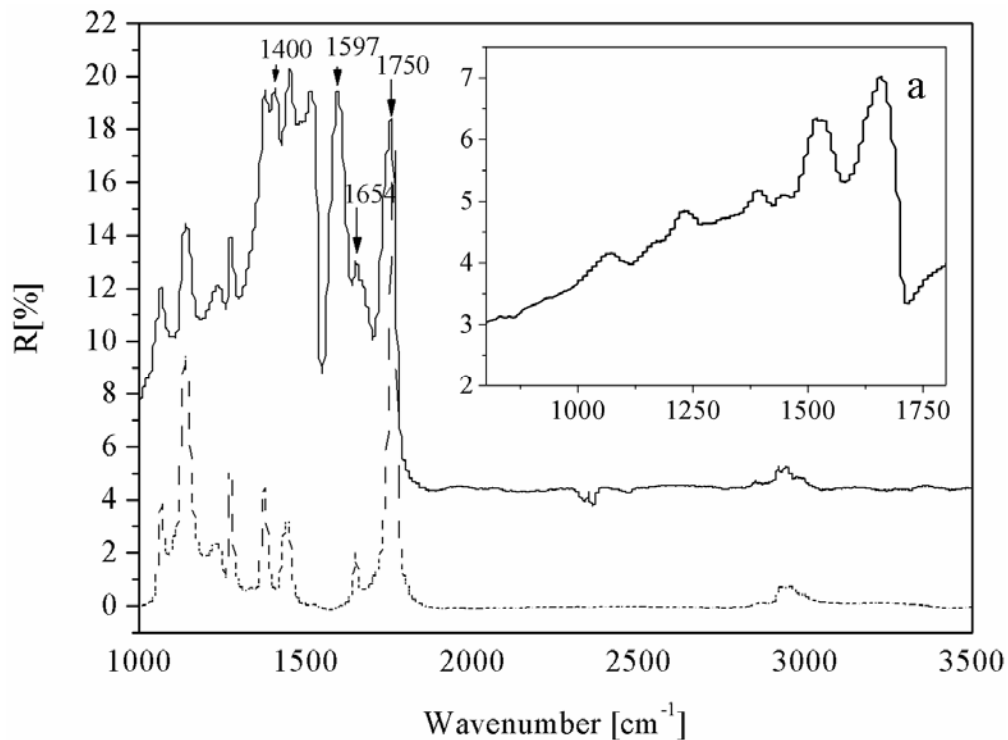


Figure 3.3a. FT-IR of NH_2 functionalized gold substrate (dotted line) and covalently bound reactive polymer atop (solid line).

Binding of silicatein to the surface functionalized with NTA on top of the polymer thin films was also confirmed by confocal laser scanning microscopy (CLSM, Leica TCS SL with an argon laser).^[21]

Fluorescence of the dye molecules was excited at 488 nm and detected from 504 - 514 nm using a 20 fold dry objective. The advantage of CLSM is that (i) detection of protein using fluorophore labeled antibodies is very specific, i.e. this antibody does not bind to any other component, and (ii) a large surface area can be seen. Fig. 3.3b shows the CLSM image of immobilized silicatein after exposing the surface to fluorophore labeled antibodies. The polyclonal antibodies raised against the axial filaments of the demosponge *Suberites domuncula* were used.^[21]

The surfaces with immobilized silicatein were reacted with solutions containing PoAb-aSilic; the immunocomplexes were then stained with fluorophore-labeled (Cy3-label) secondary goat

anti-rabbit antibodies. The surface bound silicatein strongly reacted with the antibodies. Due to the presence of Cy2, they appeared green and fluoresced at 520 nm using an Olympus AHB3 light microscope, together with an AH3-RFC reflected light fluorescence attachment. The high magnification image in Fig. 3.3b indicates that (i) silicatein is immobilized on the SAM, (ii) the surface coverage is large, and (iii) exhibit partly cluster-type adsorption patterns.

In order to confirm the hydrolytic activity of the surface-bound silicatein for the deposition of titania or zirconia, we performed two comparative sets of experiments. One set of experiments used surface-bound silicatein, and a second set of experiments was conducted with non-functionalized gold surfaces.

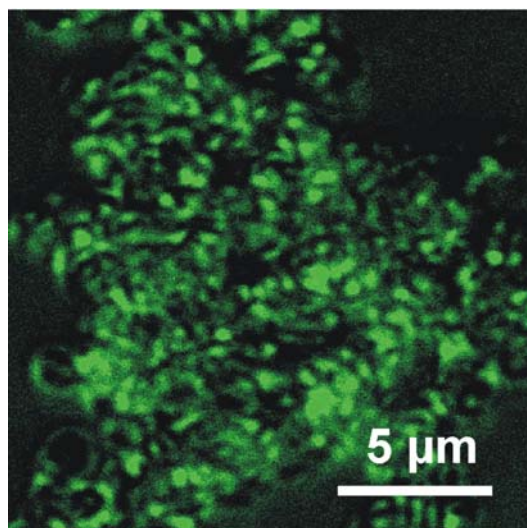


Figure 3.3b. CLSM picture of fluorophor labelled silicatein.

Under these similar sets of conditions for both experiments, we observed the formation of structured titania or zirconia only on silicatein-coated surfaces, as evidenced by the SEM images in Fig. 3.4a and 3.4c. Fig. 3.4b and 3.4d show HRSEM images, which reveal a layer-like appearance of titania and zirconia nanoparticles with diameters of 50-60 nm using immobilized silicatein.

No formation of titania or zirconia was observed, when the precipitation was performed on surfaces modified with polymer NTA only. The surface turned black when exposed to the

electron beam in the scanning electron microscope, which indicates the presence of organic material, such as NTA alkanethiol, that decomposes upon exposure to the electron beam.

Furthermore, the distribution pattern of TiO_2 and ZrO_2 is reminiscent of that observed for silicatein in Fig. 3.3b. The formation of titania and zirconia by surface bound protein indicates that the hydrolytic activity of silicatein is quite unspecific, i.e. charge density and coordination number of the metal atom seem to be less important (c.n. 4 for Si, 6 for Ti, 6-8 for Zr). Moreover, the active site of the protein immobilized on top of a “polymer cushion” is freely accessible from solution.

There are significant morphological differences between TiO_2 and ZrO_2 resulting from silicatein- and base-catalyzed syntheses. The product resulting from the catalysis by surface bound silicatein has a layer-like appearance, whereas the particles resulting from a base catalysis have a more spherical character.

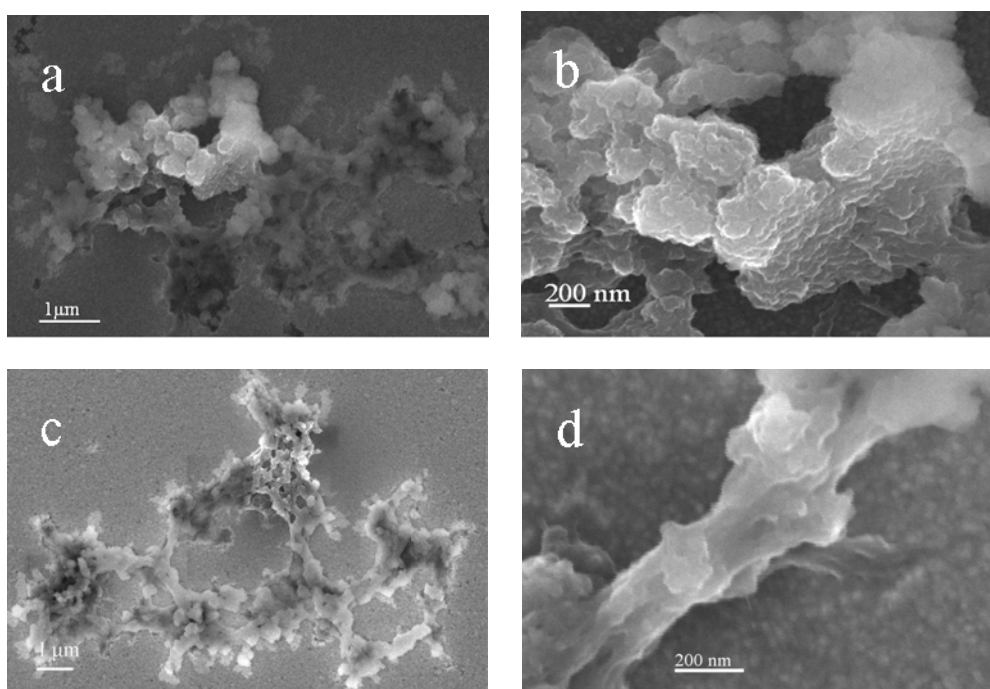


Figure 3.4. SEM/HRSEM images of TiO_2 (a) and (c) and ZrO_2 (b) and (d) formed by catalysis using surface-bound silicatein. No observable formation of TiO_2 or ZrO_2 occurred on NTA alkanethiol modified surfaces.

These morphological differences may be directly related to the nucleation mechanism occurring during the growth of TiO_2 and ZrO_2 . Surface-bound silicatein should exhibit a

number of nucleation sites (e.g. clusters of contiguous -OH side chains on the silicatein protein upon which the newly formed MO_x ($M = \text{Ti}, \text{Zr}$) polyhedra might condense. Such structural features of the surface bound silicatein can act as “electrostatic reliefs” which lower the heterogeneous nucleation barrier while keeping the intrinsically high barrier for homogeneous nucleation (i.e. base-catalyzed precipitation from solution) constant. By offering favorable surface sites on which nuclei can form, the surface-bound silicatein (in particular clusters as seen in Fig. 3.3b) may act initially as a template and stabilize smaller nuclei (with lower surface roughness) than formed by homogeneous nucleation. The potential for a summation of weak interactions (i.e., hydrogen bonding and van der Waals forces) at the interface between the polymer/silicatein layers and the crystallising mineral may even stabilize a layered polymorph of TiO_2 . There exists, in fact, a true layered polymorph of TiO_2 ($\text{TiO}_2(\text{B})^{[22]}$) which is formed under different (hydrothermal) conditions.

3.3. Conclusion

In conclusion, we could present a novel self-assembly of NTA on top of a “cushion” of reactive ester polymer. These functionalized rfaces could immobilize histidine-tagged silicatein using the efficient chelating properties with Ni^{2+} . The results presented here demonstrate that silicatein, previously shown active for catalysing and structurally directing the polycondensation of silicon alkoxides in solution as well as on surfaces can catalyze the deposition of titania and zirconia from aqueous solution. Furthermore, it becomes evident that silicatein exhibits a very general hydrolytic activity which seems independent of the coordination of the metal in the precursor compound. Finally, the results indicate that surface binding of crystallization promoters such as silicatein have an important impact on the morphology of the resulting products.

3.4. Experimental

Gold films (100nm) were coated on freshly cleaved mica surfaces using (Edwards FL 400) at rate of 0.2 nm/s and under a pressure of 5×10^{-6} mbar. Film thickness was monitored by a quartz crystal oscillator. After evaporation, the mica supported gold films were placed on a stainless steel plate which was kept inside a glass tube of a tube furnace. The gold films were annealed at 650°C under a constant flow of N₂ for 2 minutes. Gold (111) coated glass substrates were placed in an ethanolic solution of cysteamine alkanethiol (3 mmol) for a period of 12 hours. After self assembly, the surfaces were washed with ethanol to remove unbound cysteamine alkanethiol. Cysteamine coated gold slides were exposed to polymer solution in ethanol (1 mg/ml) followed by the solution of NTA amine. To immobilize the protein, Ni^{II} was bound to NTA group, the gold slides functionalized with NTA were treated with 1 mmol NaOH for 10 minutes, followed by dipping of slides in a solution of NiSO₄ (40 mmol) for 1 hour. Then slides were taken out, washed with (150 mmol) solution of NaCl and deionized water and dried in a stream of N₂. Then silicatein solution (30 nmol) in 3-(N-morpholino) propane sulfonic acid (MOPS) buffer was introduced to the Ni^{II} bound surfaces for 1 hour. Then slides were washed with MOPS buffer and deionized water to get rid of unbound protein and dried by N₂. The immobilization of silicatein was monitored by CLSM and SPS. The synthesis of titania and zirconia from titanium bis(ammonium lactato) dihydroxide and anion of zirconium fluoride was carried out at room temperature and neutral pH. The silicatein immobilized substrates were placed facing down into a reaction vessel containing 200 ml of titanium bis(ammonium lactato) dihydroxide (4.5 mmol, 135 ml) or potassium hexafluoro zirconate (3 mmol, 135 ml) and MOPS buffer (75 ml). The reaction vessel was transferred into a desiccator. The polymerization was stopped after 16 hrs. Then substrates were washed with MOPS and deionized water and dried by stream of N₂. For SPS and (scanning electron microscopy (SEM) glass slides (3.5 x 2.5 cm) were used. Glass slides were cleaned with aq.NH₃ / H₂O₂ / H₂O (1:1:5) for 10 minutes at 80 °C, washed with water and isopropanol and dried in stream of N₂. These glass slides were coated with gold using (Edwards FL 400), vacuum coating unit under pressure of less than 5×10^{-6} hPa, typically depositing 50 nm of gold after first depositing 2 nm of Cr.

Scanning Force Microscopy

Gold (111) surfaces were imaged at room temperature with a commercial SFM (Nanoscope IIIa, Digital Instruments, Santa Barbara, California) employing Tapping Mode TM using rectangular silicon cantilevers (Nanosensors, 125 μm long, 30 μm wide, 4 μm thick) with an integrated tip, a nominal spring constant of 42 N/m^{-1} , and a resonance frequency of 330 kHz. To control and enhance the range of the attractive interaction regime the instrument was equipped with a special active feedback circuit, called Q-control (Nanoanalytics, Germany) as described in ref. 1. The quality factor Q of this oscillating system is increased up to one order of magnitude. As a consequence, the sensitivity and lateral resolution are enhanced, allowing us to prevent the onset of intermittent repulsive contact and thereby to operate the SFM constantly in the attractive interaction regime.

SPS Experimental

SPS measurements were performed in the Kretschmann configuration against ethanol. Optical coupling was achieved with a LASFN 9 prism, $n = 1.85$ at $\lambda = 632.8$ nm and index matching fluid $n = 1.70$ between prism and the BK270 glass slides. The plasmon was excited with P-polarized radiation using a He/Ne laser (632.6 nm, 5 mW).

Scanning Electron Microscopy

The SE micrographs were acquired with LEO 1530 by LEO Electron Microscopy Ltd, Cambridge, England Carl Zeiss and Leica Join Forces in Electron Microscopy.

Confocal Laser Scanning microscopy

Fluorescence images were taken by an inverted laser scanning microscope (Leica TCS SL, Leica Microsystems, Bensheim, Germany). A 40x (NA 1.25) oil immersion objective was used for the imaging of all samples.

Synthesis of the reactive ester polymer

The polymer was synthesized according to method already published by Marc et al.^[18] A brief description of the synthesis is provided below.

Synthesis of monomer acetoxime methacrylate:

2,19 g (0,03 mol) acetoxime and a few percent of 2,6-di-tert-butyl-4-methyl phenol were dissolved in 60 ml of dry chloroform. To the cold mixture 4,2 ml of triethylamine and 2,9 ml (0,03 mol) methacryloylchloride were added drop wise. The solution was stirred for 3 hours at room temperature. After evaporating the solvent under reduced pressure the salt was filtered off and product was distilled under reduced pressure yielding pure acetoxime methacrylate. (1,6* 10⁻² mbar, bp. 41°C). ¹HNMR: δ [ppm]= 5.99, 5.47, 1.91, 1.88, 1.84.

Polymerization:

The monomer and 0.01 mol% of AIBN were dissolved in dry dioxane, degassed and stirred for 24 hours at 80°C. The resulting homopolymers were precipitated in cold diethylether.

3.5. References

- [1] a) K. L. Prime, G. M. Whitesides, *Science* **1991**, 252, 1164-1167. b) I. Willner, E. Katz, *Angew. Chem. Int. Ed.* **2000**, 38, 1180-1218.
- [2] T. Wink, S. J. van Zuilen, A. Bult, W. P. van Bennekom, *Analyst.* **1997**, 122, 43R-50R.
- [3] I. Willner, E. Katz, *Angew. Chem. Int. Ed.* **1998**, 37, 3253-3256.
- [4] I. Willner, E. Katz, *New J. Chem.* **1999**, 23, 481-487.
- [5] M. N. Tahir, P. Theato, W. E. G. Müller, H. C. Schröder, A. Janshoff, J. Zhang, J. Huth, W. Tremel, *Chem. Comm.* **2004**, 2848-2849.
- [6] a) K. Shimizu, J. N. Cha, G. D. Stucky, D. E. Morse, *Proc. Natl. Acad. Sci. USA* **1998**, 95, 6234-6238. b) J. N. Cha, K. Shimizu, Y. Zhou, S. C. Christiansen, B. F. Chmelka, G. D. Stucky, D. E. Morse, *Proc. Natl. Acad. Sci. USA* **1999**, 96, 361-364.
- [7] A. Krasko, R. Batel, H. C. Schröder, I. M. Müller, W. E. G. Müller, *Eur. J. Biochem.* **2000**, 267, 4878-4887.
- [8] J. L. Sumerel, W. Yang, D. Kisailus, J. C. Weaver, J. H. Choi, D. E. Morse, *Chem. Mater.* **2003**, 15, 4804-4809.
- [9] V. Bansal, D. Rautaray, A. Ahmad, M. Sastry, *J. Mater. Chem.* **2004**, 14, 3303-3305.
- [10] H. Ding, M. K. Ram, C. Nicolini, *J. Nanosci. Nanotechnol.* **2001**, 1, 207-213.
- [11] S. Sato, R. Nakamura, S. Abe, *Appl. Catal. A* **2005**, 284, 131-137.
- [12] J. Braun, A. Baidins, R. E. Marganski, *Progr. Org. Coatings* **1992**, 20, 105-138.
- [13] M. Y. Song, D. K. Kim, K. J. Ihn, S. M. Jo, D. Young, *Nanotechnol.* **2004**, 15, 1861-1865.
- [14] D. Qing, H. Nongyue, G. Yan, Y. Chunwei, *Chem. Lett.* **1998**, 11, 1113-1114.
- [15] A. Corma, *Chem. Rev.* **1997**, 97, 2373-2419.
- [16] A. Rosidian, Y. Liu, R. O. Claus, *Adv. Mater.* **1998**, 10, 1087-1091.
- [17] J. Zhu, T. L. Li, B. Pan, L. Zhou, Z. G. Liu, *J. Phys. D: Appl. Phys.* **2003**, 36, 389-393.
- [18] M. Eberhardt, N. Metz, R. Zentel, P. Theato, *Polymer Prepr.* **2005**, 46, 100-101.
- [19] W. J. Miller, N. L. Abbott, *Langmuir* **1997**, 13, 7106-7114.
- [20] N. Wu, L. Fu, M. Su, M. Aslam, K. C. Wong, V. P. Dravid, *Nano Lett.* **2004**, 4, 383-386.

- [21] W. E. G. Müller, M. Rothenberger, A. Boreiko, W. Tremel, A. Reiber, H. C. Schröder, *Cell. Tiss. Res.* **2005**, *321*, 285–297.
- [22] (a) M. Tournoux, R. Marchand, L. Brohan, *Prog. Solid State Chem.* **1986**, *17*, 33-52.
(b) T. P. Feist, P. K. Davies, *J. Solid State Chem.* **1992**, *101*, 275-295.

4. Controlling Au Nanocrystal Size and Shape by Chiral Induction Using Wildtype and Recombinant Silicatein from *Suberites domuncula*

4.1. Introduction

The growing interest in building advanced materials based on nanoscale building blocks^[1] calls for general approaches to control the phase, size, morphology of inorganic nanoparticles. A range of methods have been applied to this end, but there is still need for systems that are flexible enough to be applied to chemically distinct systems. Belcher and coworkers^[2] recently suggested that combinatorial strategies may offer the required generality, and this evolutionary approach stimulated research following biomimetic pathways to metal, metal oxide, and sulfide nanoparticles.^[3] Although presumably most proteins are capable of binding metal ions in solution, inorganic binding proteins have been identified using combinatorial as well as traditional approaches, where the “traditional approach” includes the isolation and identification of proteins that associate with inorganic components *in vivo* using molecular biology techniques.^[4] Combinatorial approaches, on the other hand, have been used to identify oligopeptides and protein fragments that selectively recognize the surface of inorganic solids such as metals,^[5] metal oxides,^[6] sulfides^[7] or ionic compounds.^[8] In fact, a tenet of biomineralization is that by molecular recognition peptide fragments of proteins or other biomacromolecules serve as templates for the nucleation and growth of inorganic materials.^[9]

From a simple coordination chemistry viewpoint the chemical lead involved in the deposition of inorganic materials using biological or synthetic macromolecules are the amino acid sequence and the spatial density of functional groups at the periphery of the macromolecule that control its “surface chemistry” by complexation of the metal cations, resulting in the subsequent nucleation and growth of the inorganic nanoparticles. Although the combinatorial idea is quite successful it may be nonetheless not exhaustive and yield results that seem to contradict chemical experience such as the selective binding of silver ions by a preferential enrichment of proline and hydroxyl-containing amino acid residues.^[10] Intrigued by these

predictions and based on a databank search we focused on silicatein,^[11] a cathepsin L-type protein from sponges for the following reasons: (1) it has been shown to contain high serine (> 10%), tyrosine (> 7%), and lysine and arginine (12%) contents as well as six cysteine residues involved in intramolecular bridges. The cysteine at the active site of the proteases is replaced by serine in α -silicatein, although the six cysteines that form disulfide bridges in the proteases are conserved. Furthermore, α -silicatein contains unique tandem arrays of multiple hydroxyls. These structural features can explain the mechanism of biosilicification and the activity of the silicateins in promoting the condensation of silica and organically modified siloxane polymers (silicones) from the corresponding silicon alkoxides.^[12] (2) The biological function of silicatein is related to a serine and histidine residues at the active site but seems to be unrelated to the large spatial density of serine and tyrosine at the periphery of the protein.^[13]

As expected from the combinatorial predictions, silicatein assists in the “biosynthesis” of Ag and Au nanocrystals. Surprisingly, however, the hydroxyl-containing amino acid residues seem to be unrelated the stabilization of metal nanoparticles. Here we demonstrate that (1) hexagonal and substantial amounts of triangular Au nanocrystals are formed by the reducing action of silicatein, (2) Au nanocrystals are stabilized by the surface binding of NH₂ containing amino acid residues, and (3) we give evidence that the morphogenetic control of nanocrystal formation reflects the chirality of the surface binding of the protein.

4.2. Results and discussion

Colloidal gold particles are formed upon incubating buffered solutions of silicatein with aqueous solution tetrachloroaurate anions AuCl₄⁻ at room temperature. The formation of the Au nanocrystals and the adsorption onto the axial filaments from *S. domuncula* can be monitored unaided with the naked-eye or by UV-vis spectroscopy (Figure 4.1). 60 min after mixing silicatein and the pale yellow tetrachloroaurate solution the color of the solution turned ruby red indicating the reduction of tetrachloroaurate and the formation of gold colloids. Plasmon absorption of metal colloid is a well-known indicator of aggregation as well as particle size. A study of the area under the single and aggregated plasmon resonance peaks provides information about the extent of the aggregation. After about 60 min a surface

plasmon band appears at ~ 580 nm. The intensity of this absorption band increases with time and shifts to smaller wavelengths. After six hours, the absorption spectrum of the gold colloid solutions showed a strong absorption band with a maximum at ca. 540 nm and an increase of the absorption close to the infrared region of the visible spectrum. Single isolated colloidal gold particles have a surface plasmon resonance manifested as a single absorbance band at approximately 520 nm and aggregated gold complexes develop new red-shifted peaks/shoulders depending on the nature and extent of the aggregated complex.^[14] The UV-vis spectroscopic data is consistent with the formation of colloidal particles and subsequent aggregation with time to larger units.

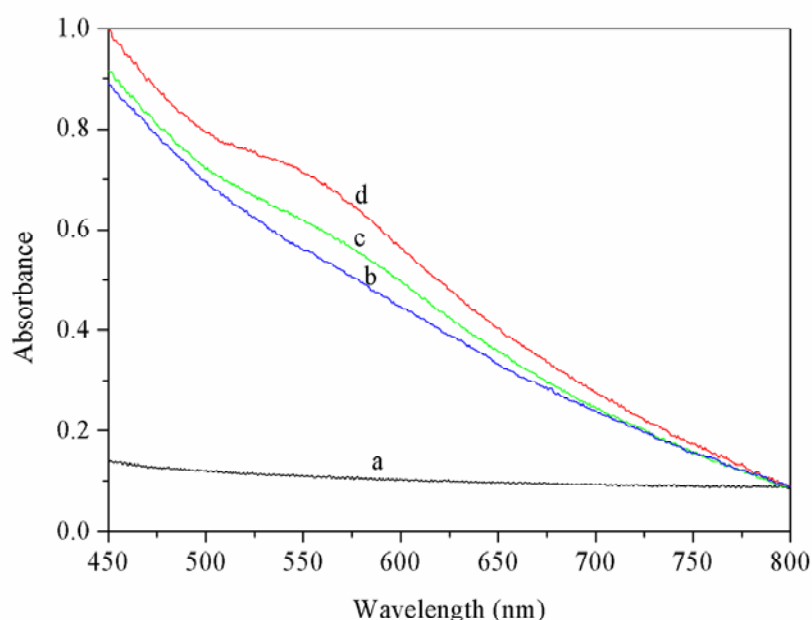


Figure 4.1. UV-Vis spectra of the products of the reaction of recombinant silicatein with AuCl_4^- recorded as a function of time. (a) 60 min, (b) 180 min, (c) 300 min, (d) 420 min

Transmission electron microscopy (TEM) images of the AuCl_4^- / silicatein solution after 24 hours are presented in Figure 4.2. Figure 4.2a shows the product distribution obtained from the reaction of silicatein filaments with an aqueous AuCl_4^- solution (10^{-3} M). Hexagonal shaped Au nanocrystals with diameters of approx. 100 nm are composed of much smaller Au nanoparticles with diameters of approx. 10 nm.

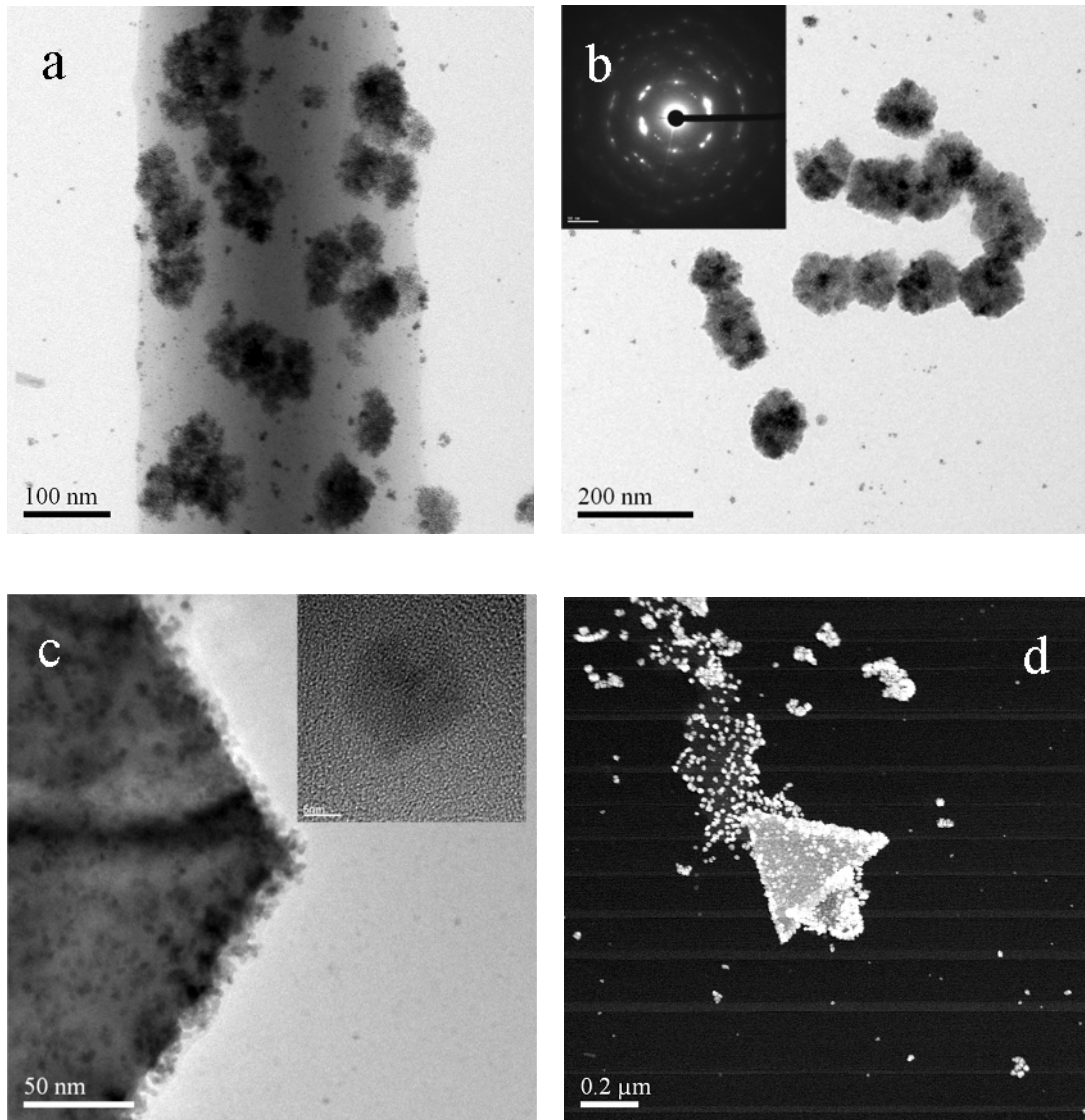


Figure 4.2. TEM images of AuCl_4^- reduced with aqueous solutions of recombinant silicatein. (a) Au nanocrystals on the axial filaments from *S. domuncula*. (b) Au nanocrystals not attached to the axial filament with SAED (selected area diffraction pattern), indicating the crystalline nature of the sample. (c) TEM image of the edge of one of the nanocrystals in (b) decorated with small nanocrystals stabilized by silicatein. The inset reveals the crystallinity of the smaller nanocrystals. This image demonstrates the high surface mobility at the edges of the nanocrystals. (d) Triangular Au

These findings are compatible with the UV-Vis absorption spectra in Figure 4.1, which indicate the formation of Au nanoparticles with diameters of ~ 10 nm. Both, smaller and larger particles aggregate on the silicatein containing filaments with the (111) face of the Au fcc lattice appearing as the large flat high-symmetry face of the Au nanocrystals.

In Figure 4.2b several of the hexagonal platelets are shown in higher magnification. The selected area electron diffraction pattern in the inset of Figure 4.2b shows the presence of agglomerated Au nanocrystals with hexagonally arranged diffraction spots characteristic of crystalline (111) oriented gold platelets apparent. Figure 4.2c reveals that the edges of the hexagonal platelets are decorated with smaller (diameter ~ 5 nm) Au nanoparticles.

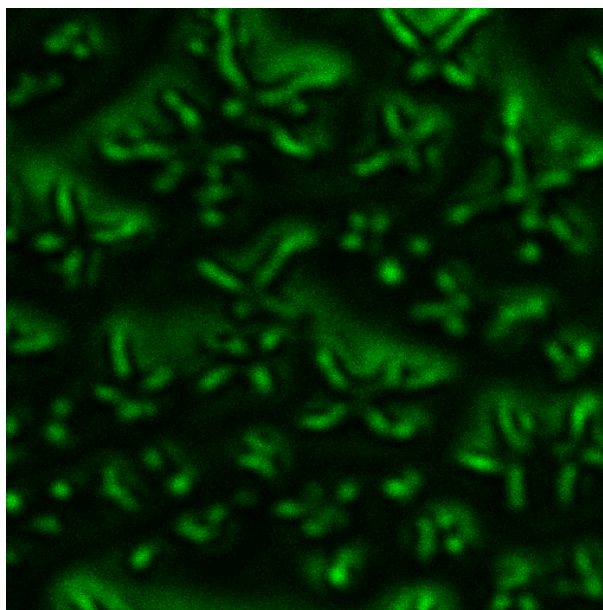


Figure 4.3. Upon covalent immobilization of fluorophore-labeled (Cy2 label) secondary goat anti rabbit antibodies onto their surfaces, the surface bonded silicatein can be visualized by using fluorescence microscopy.

Particle edges and stepped high-index surfaces with low-coordinate Au atoms represent high energy surfaces sites that tend to stabilize themselves by surface restructuring, adding nanoclusters from solution stabilized by surface bound silicatein or binding of protein surface ligands.^[15] In a recent paper describing the formation of Au nanocrystals using lemon grass extract Sastry and coworkers^[16] assume liquid-like assemblies of spherical nanoparticles to be responsible for the nanocrystal formation. The particles observed in Figure 4.2 may be supportive of that hypothesis. After several hours of reaction compact hexagonal platelets with sharpened edges area are formed by ripening process (Ostwald ripening) in which the larger hexagonal nanocrystals grow at the expense of the smaller ones, with silicatein still being present as a surface ligand on the hexagonal nanocrystals.

Replacing native silicatein by the recombinant protein leads to enhanced formation of triangular Au nanocrystals (diameter ~ 50 nm). This is illustrated in Figure 2d. Similar as in the case of the native silicatein, the crystal edges are decorated with Au nanoparticles. Monoclonal antibodies raised against axial filaments were used to demonstrate the surface binding of silicatein using fluorescence microscopy^[17] as shown in Figure 3. The solutions containing Au nanocrystals were prepared and reacted with mAb-aSilic (monoclonal antibodies directed against recombinant silicatein- α); the immunocomplexes were then detected via fluorophore-labeled (Cy2-label) secondary goat anti-rabbit antibodies. The surface of the Au nanoparticles and the axial filament strongly reacted with the antibodies. Fluorescence of the dye molecules was excited at 488 nm and detected from 504 - 520 nm using a 20 fold dry objective.

Due to the presence of Cy2, they appeared green and fluoresced at 520 nm. CLSM with line of a helium/neon laser was used. A 40x (NA 1.25) oil immersion objective was used for the imaging of all samples, as a result it can be seen at high magnification that the antibodies brightly stain the surface of the Au nanoparticles, i.e. the protein is chemically bonded to the Au surface. It is difficult to comment on the actual size of gold nanoparticles because it was beyond the resolution limits of CLSM. Functional groups involved in the surface binding of silicatein could be the SH groups of the cysteine, the OH groups of the serine or the amino groups of arginine, lysine or histidine residues. Vibrational spectroscopy can offer clues concerning the Au-ligand binding.

Figure 4.4 shows the infrared (FT-IR) spectrum of the Au / silicatein complex where the most prominent bands in the $3500\text{-}3300\text{ cm}^{-1}$ region can be assigned to the amino and amido stretching vibrations, the absorption bands from $1700\text{-}1600\text{ cm}^{-1}$ to the C=O stretches, and the bands below 400 cm^{-1} may be attributed to the Au-ligand vibrations.

The asymmetry of the carbonyl stretch combined with its position at 1627 cm^{-1} are indicative of a large amount of parallel β sheets,^[18] where the CO stretching frequency is reduced significantly by amide formation and hydrogen bonding, and the amide II stretch is hidden in the shoulder of the band centered at 1518 cm^{-1} which can be assigned to the aromatic rings of tyrosine. The strong shoulder centered at 3280 cm^{-1} and the small hump at 3050 cm^{-1} is indicative of (partially protonated) primary and secondary amino groups. Vibrational bands that could be assigned to Au-ligand stretches should appear in the low frequency range $\leq 250\text{ cm}^{-1}$. Only a limited number of coordination compounds are known for the noble metals gold

and silver,^[19] the most stable ones among them being sulfur or chloro species. As a noble metal with soft ions, gold has a very low affinity towards oxygen.^[19,20] While the two group homologues, silver and copper, possess a visible oxide chemistry,^[21] only a small number of metastable gold oxygen compounds exist.^[22]

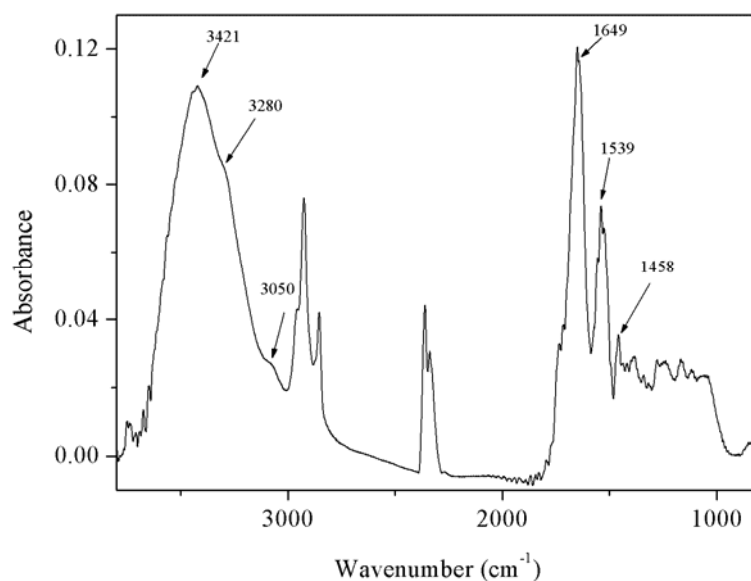


Figure 4.4. FT-IR spectrum of biocatalytically synthesized gold nanoparticles.

The paucity of gold or silver oxygen compounds in comparison to the corresponding nitrogen complexes (such as the $[\text{Ag}(\text{NH}_3)_2]^+$ complex) together with the available spectroscopic data indicate that the protein binding to the surface of the Au nanoparticles should be due to complexation by the sulfido or amino groups of the protein. This hypothesis is also in agreement with the Pearson HSAB concept.^[23] In fact, inspection of the amino acid sequence of silicatein reveals an unusually large amount (12 %) of basic amino acids (arginine, lysine) to be present.^[11b] Some polypeptide sequences in proteins secreted by the bacterium *Escherichia coli* have been reported to induce the formation of triangular nanocrystals in low yield.^[5b] Finally, Sastry and coworkers described the reduction of AuCl_4^- solutions by using lemon grass extract to yield triangular Au nanocrystals.^[16] These triangular crystals were assumed to be assembled from “liquid-like” colloidal particles stabilized by surface-bound aldehydes/ketone (from (poly)saccharides) present in the extract. Since recombinant silicatein does not contain any saccharide groups, the SH groups must be considered to be involved in

the formation of Au colloids as reductive sites. As electron transfer can occur easily over distances of 20 Å and more,^[24] this reduction does not require the SH groups to be located at the periphery of protein. The amino groups arranged at the outer surface of silicatein may be assumed to act as coordinating centers for the surface binding of the gold colloids.

What leads to the hexagonal or triangular morphology of the Au nanocrystals? First of all, it is remarkable that in aqueous reaction media, where crystals are free to grow in three dimensions, platelet-like triangular and hexagonal gold crystals are formed. This phenomenon

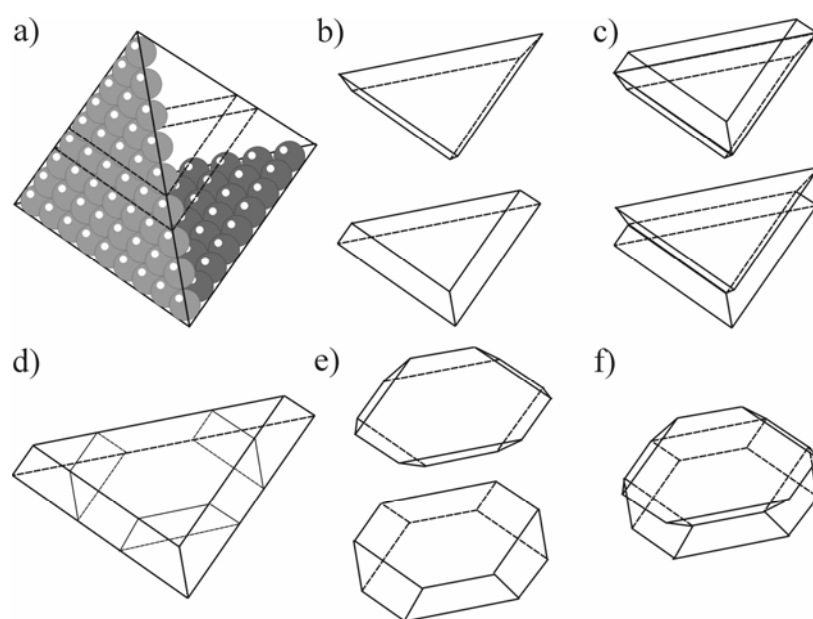


Figure 4.5. (a) Au nanocrystal with fcc structure. (b) Morphology of a triangular slice cut from a 3D gold crystal. (c) A stacking fault in the structure can be constructed by mirroring the triangle and gluing it to the first one face to face. (d) The hexagonal platelets can be modeled by truncating the three corners of a triangle. (e) One can construct a faulted hexagon by mirroring with a perimeter containing (f) alternating bulges and notches (convex and concave faces).

has been already observed by other authors,^[5,16,25] who reported on the formation of 2D (platelets) and 3D growth of gold crystals induced by various organic materials.

Gold crystallizes in a fcc-type structure. The hexagonal face of the crystals corresponds to the (111) plane, the most densely populated lattice plane of the Au structure. The (111) plane has

the lowest surface energy and the lowest growth rate, and this is why $\langle 111 \rangle$ facets usually contour gold crystals in their equilibrium shape, which would be cuboctahedral, octahedral, etc. Brown et al.^[5] suggested that the large platelet-like crystals can include an internal grain boundary, parallel to the large (111) facets. Figure 4.5 schematically shows the morphology of a triangular slice cut from a 3D gold crystal (Figure 4.5a). A stacking fault in the structure can be constructed by mirroring the triangle and gluing it to the first one face to face. This construction has an edge around the perimeter which will favor lateral growth for surface energy reasons. One can imagine this edge to be inversed as shown in Figure 4.5c (upper part). This construction seems to be less favorable for 2D growth, but usually several parallel stacking faults are formed; as a result, the perimeter has a zigzag shape with several reactive surface sites for accelerated lateral growth.

The hexagonal platelets can be modeled by truncating the three corners of a triangle. The facets have to be of (111) type, so the cutting planes must be inclined. The resulting hexagon has a perimeter bounded by six $\langle 111 \rangle$ facets: three of them are inclined upwards, three of them downwards. One can construct a faulted hexagon by mirroring (Figure 4.5e) with a perimeter containing alternating bulges and notches (convex and concave faces, Figure 4.5f).

No established mechanism for gold crystallization in the presence of organic/biological additives exists so far. One possibility would be that the protein influences the formation of gold clusters at the nucleation stage. At this early stage either spherical gold particles seeds, whose surfaces are stabilized by silicatein binding, are formed, or nuclei with stacking faults appear. The faulted seeds will then give rise to large platelet-like crystals. These twinned crystals usually grow laterally much faster than 3D polygons.

What is the reason for the triangular morphology of the Au nanocrystals in the presence of recombinant silicatein? Shape control of inorganic materials in biological systems is achieved either by growth in constrained environments such as membrane vesicles,^[26] or through functional molecules such as polypeptides that bind specifically to inorganic surfaces.^[5,16,27,28] Specific polypeptide repeat sequences in proteins secreted by the bacterium *E. coli* have been shown to induce growth of flat, triangular gold nanocrystals in low yield relative to the total nanoparticle formation.^[5] Therefore, a possible explanation for the formation of surface bound nano-triangles is based on the chirality of the nucleation centers at the surface of the protein. Whereas hexagonal crystals are *achiral*, because they have an inversion center in the center of the Au hexagons, triangular crystals are *chiral*, because the inversion symmetry is lost during the nucleation and growth of the triangular crystal. An S_3 axis of the hexagon is maintained as

the high symmetry element, i.e. chiral information contained in the silicatein structure is transmitted to the nucleating gold nanocrystals during the $\text{AuCl}_4^- \rightarrow \text{Au}$ reduction and the subsequent Au nucleation at the outer surface of the protein and maintained during the nanocrystal growth. This is compatible with the observation that triangular nanocrystals were also formed by reduction of AuCl_4^- in presence of lemon grass extract,^[16] which presumably contains a multitude of yet unidentified proteins. In contrast, no triangular or even pronounced Au nanocrystal morphologies were observed when Au precursor compounds were reduced chemically and attached to histidin-rich peptides on the surface of carbon nanotubes.^[29] These findings suggest that the morphology of the Au nanocrystals is determined by the coordination and simultaneous reduction during nucleation process in the presence of the protein rather than by the chemical reduction in solution and subsequent binding to the polypeptide chain.

Another clue is that the triangular morphology is most prominent when the reduction and biomimetic growth of the gold nanocrystals is performed using the recombinant silicatein, whereas smaller yields are obtained using silicatein isolated from *S. domuncula* (which may contain unknown non-chiral contaminant components). The formation of triangular gold nanocrystals using recombinant silicatein provides a link between the highly complex processes involved for example in determining the helicity of shells of *Globigerina pachyderma*,^[30] and typical model systems studied in the laboratory, such as the growth of calcite in the presence of chiral amino acids.^[31]

There are several examples of crystals formed by biological processes that have macroscopic chirality with only one of the possible mirror-images being produced. The sponge *Sycon* has calcitic spicules, some of which grow into a sabre shape along one of three possible symmetrically identical directions.^[32] The plane of symmetry of the saber-shaped spicule, however, does not coincide with any symmetry element of the *Sycon* structure. Thus the integration of the molecular symmetry with the macroscopic symmetry is chiral. The calcium oxalate crystals from the leaves of tobacco or tomato plants have been known for more than a century to have chiral morphology.^[33] Each plant species always forms crystals with the same morphology at the same tissue site, implying that the chirality is under genetic control.

Finally, the biological function of silicatein, i.e. the formation of biosilica, and the reported non-biological activity of silicatein in the hydrolytic formation of SiO_2 ,^[12,34] TiO_2 ,^[35] ZrO_2 ,^[36] and GaOOH ^[37] or the reductive formation of Au nanoparticles reported in this paper allows some general assignments and predictions to be made concerning the reactivity and the

chemical functionality of the protein subunits: (1) hydrolytic activity at the active center, e.g. for the formation of early transition metal oxides^[35,36] or transition metal oxyhydroxides,^[37] (2) reductive formation of late transition metal colloids by the SH groups of the cystein units and subsequent stabilization of the resulting nanoparticles by complexation through the amino acids at the periphery of the protein, (3) stabilization of chalcogenide nanoparticles (such as CdS) by metal complexation through the NH₂-containing residues of the protein. The general hydrolytic activity of silicatein has been reported,^[12] and the reductive formation of gold nanocrystals is described in this contribution. Research aiming at the stabilization of chalcogenide nanoparticles by silicatein is underway.

4.3. Conclusion

In summary, the formation of Au nanoparticles by the hydrolytic protein silicatein has been demonstrated. The reduction of AuCl₄⁻ species occurs by the action of sulfhydryl groups hidden below the surface groups of the protein. The gold nanoparticles resulting from the bioreduction by silicatein are stabilized by surface binding through the NH₂ groups of the basic amino acid residues of silicatein, as shown by fluorescence microscopy using a fluorophore attached to the protein by specific antigen-antibody interactions. The Au nanoparticles further aggregate to form Au nanocrystals as evidenced by transmission electron microscopy. The triangular shape of the nanocrystals obtained by using recombinant silicatein may be explained by chiral induction through the protein during the nucleation of the nanocrystals.

4.4. Experimental

Preparation of recombinant silicatein and silicatein filaments. The native silicatein (axial filaments) were isolated from the *S. domuncula* spicules by dissolution of the silica material with hydrofluoric acid (2 M HF / 8 M NH₄F; pH 5) at room temperature.^[38] The axial filaments were obtained, dialyzed against distilled water and collected by centrifugation. Recombinant silicatein was prepared as described.^[39]

“Nanogold formation” silicatein filaments in water or silicatein recombinant in Tris buffer (0.05 M) were added to 0.5 ml of aqueous solution of H₂AuCl₄ (10⁻³ M) in 1.5 ml of polyethylene vial. The protein was mixed with precursor solution by pipetting for 2 min and immediately placed on rotator (biocentrifuge fresco). The protein-precursor suspension was mixed on the rotator at a speed of 1000 rpm for 24 hours under normal conditions. The biotransformation was routinely monitored by periodic sampling of aliquots of aqueous component and measuring the UV-visible spectroscopy. Following this reaction period; the biomass was centrifuged at 3000 rpm for 10 min and repeatedly washed with sterile distilled water before doing all characterization.

Analytical Methods. X-ray powder diffraction studies were carried using Siemens D8 powder diffractometer equipped with a position sensitive detector. Data were collected between $2\theta = 30^\circ - 70^\circ$ (using Cu K α radiation), at an operation potential of 40 kV and a current of 40 mA. The morphology of the Au nanoparticles and triangles was characterized by a high-resolution transmission electron microscopy (FEI Tecnai F30 ST operated at an extraction voltage of 300kV, equipped with an EDXA (energy dispersive X-ray spectrometer) and by selected area electron diffraction techniques (SAED). For transmission electron microscopic (TEM) studies, carbon film coated copper grids containing a drop of suspension of the sample in ethanol was used.

4.5. References

- [1] G. Schmid, *Adv. Eng. Mater.* **2001**, *3*, 737-743.
- [2] (a) S. R. Whaley, D. S. English, E. L. Hu, P. F. Barbara, A. M. Belcher, *Nature* **2000**, *405*, 665-668. (b) P. Ball, *Nature* **2001**, *409*, 413-416.
- [3] M. Sarikaya, C. Tamerler, A. K. Y. Jen, K. Schulten, F. Baneyx, *Nature Mater.* **2003**, *2*, 577-587.
- [4] N. Kröger, R. Deutzmann, M. Sumper, *Science* **1999**, *286*, 1129-1132.
- [5] (a) S. Brown, *Nature Biotechnol.* **1997**, *15*, 269-272. (b) S. Brown, M. Sarikaya, E. Johnson, *J. Mol. Biol.* **2000**, *299*, 725-732.
- [6] (a) R. R. Naik, L. Brott, S. J. Carlson, M. Stone, *J. Nanosci. Nanotechnol.* **2002**, *2*, 1-6. (b) S. Brown, *Proc. Natl. Acad. Sci. USA* **1992**, *89*, 8651-8655.
- [7] (a) P. V. Braun, P. Osenar, V. Tohver, S. B. Kennedy, S. I. Stupp, *J. Am. Chem. Soc.* **1999**, *121*, 7302-7309. (b) W. S. Lee, C. Mao, C. E. Flynn, A. M. Belcher, *Science* **2002**, *296*, 892-895.
- [8] D. J. H. Gaskin, K. Starck, E. N. Vulfson, *Biotech. Lett.* **2000**, *22*, 1211-1216.
- [9] (a) L. Addadi, S. Weiner, *Proc. Natl. Acad. Sci. USA* **1985**, *82*, 4110-4114. (b) S. Mann, *Nature* **1998**, *332*, 119-124. (c) S. Mann, D. D. Archibald, J. M. Didymus, T. Douglas, B. R. Heywood, F. C. Meldrum, N. J. Reeves, *Science* **1993**, *261*, 1286-1292.
- [10] R. R. Naik, S. J. Stringer, G. Agarwal, S. E. Jones, M. O. Stone, *Nature Mater.* **2002**, *1*, 169-172.
- [11] (a) K. Shimizu, J. Cha, G. D. Stucky, D. E. Morse, *Proc. Natl. Acad. Sci. USA* **1998**, *95*, 6234-6238. (b) A. Krasko, R. Batel, H. C. Schröder, I. M. Müller, W. E. G. Müller, *Europ. J. Biochem.* **2000**, *267*, 4878-4887.
- [12] J. N. Cha, K. Shimizu, Y. Zhou, S. C. Christiansen, B. F. Chmelka, G. D. Stucky, D. E. Morse, *Proc. Natl. Acad. Sci. USA* **1999**, *96*, 361-365.
- [13] Y. K. Zhou, K. Shimizu, J. N. Cha, G. D. Stucky, D. E. Morse, *Angew. Chem. Intl. Ed.* **1999**, *38*, 779-782.
- [14] (a) C. A. Mirkin, R. L. Letzinger, R. C. Mucic, J. J. Storhoff, *Nature* **1996**, *382*, 607-609. (b) E. Hao, K. L. Kelly, J. T. Hupp, G. C. Schatz, *J. Am. Chem. Soc.* **2002**, *124*, 15182-15183.

- [15] G. A. Somorjai, *Chemistry in two Dimensions*, Cornell University Press, Ithaca **1981**.
- [16] S. S. Shankar, A. Rai, B. Ankamwar, A. Singh, A. Ahmad, M. Sastry, *Nature Mater.* **2004**, *3*, 482-488.
- [17] W. E. G. Müller, M. Rothenberger, A. Borejko, W. Tremel, A. Reiber, H. C. Schröder, *Cell Tissue Res.* **2005**, *321*, 285-297.
- [18] (a) R. Winter, F. Noll, *Methoden der Biophysikalischen Chemie*, Teubner Studienbücher, Stuttgart, **1998**, 1790 (b) N. H. Jang, *Bull. Korean Chem. Soc.* **2002**, *23*, 1790-1800. (c) P. Laasch, Ph.D. Dissertation, FU Berlin,
- [19] A. Holleman, E. Wiberg, *Lehrbuch der Anorganischen Chemie*, De Gruyter, Berlin, **1995**.
- [20] *Gmelin Handbook of Inorganic and Organometallic Chemistry*, 8th edn., Gold Suppl., Vol. B1-B3, Springer-Verlag, Berlin **1992-94**.
- [21] M. Jansen, *Angew. Chem.* **1987**, *99*, 1136-1149. *Angew. Chem. Int. Ed.* **1987**, *26*, 1098-1110.
- [22] (a) P. G. Jones, H. Rumpel, E. Schwarzmann, G. M. Sheldrick, H. Paulus, *Acta Crystallogr.* **1979**, *B 35*, 1435-1437. (b) M. Jansen, A. V. Mudring, *The Chemistry of Gold Oxides*, in: H. Schmidbaur (Ed.), *Gold: Progress in Chemistry, Biochemistry and Technology*, John Wiley & Sons, Chichester, **1999**.
- [23] (a) R. G. Pearson, *J. Am. Chem. Soc.* **1963**, *85*, 3533-3543. (b) R. E. Palmer, P. J. Rous, J. L. Wilkes, R. F. Willis, *Phys. Rev. Lett.* **1988**, *60*, 329-332. (c) R. G. Pearson, *Inorg. Chem.* **1988**, *27*, 734-740. (d) R. G. Pearson, in: *Structure and Bonding*, Vol. 80, Springer, Berlin **1993**.
- [24] (a) *Electron Transfer in Biology and the Solid State*, M. K. Johnson, R. B. King, D. M. Kurtz, C. Kotal, M. L. Norton, R. A. Scott (Eds.), *Adv. Chem. Ser. 226*, American Chemical Society, Washington **1990**. (b) N. M. Dimitrijevic, Z. V. Saponjic, B. M. Rabatic, T. Rajh, *J. Am. Chem. Soc.* **2005**, *127*, 1344-1345.
- [25] Y. Shao, Y. Jin, S. Dong, *Chem. Comm.* **2004**, 1104-1105.
- [26] N. Kröger, R. Deutzmann, M. Sumper, *Science* **1999**, *286*, 1129-1132.
- [27] (a) L. Addadi, Z. B. Yellin, I. Weissbuch, M. Lahav, L. Leiserowitz, *Topics Stereochem.* **1986**, *16*, 1-85. (b) J. M. McBride, S. B. Bertman, *Angew. Chem. Int. Edn.* **1989**, *28*, 330-333.

- [28] (a) L. A. Estroff, C. D. Incarvito, A. D. Hamilton, *J. Am. Chem. Soc.* **2004**, *126*, 2-3.
(b) N. Banno, T. Nakanishi, M. Matsunaga, T. Asahi, T. Osaka, *J. Am. Chem. Soc.* **2004**, *126*, 428-429.
- [29] (a) H. Matsui, S. Pan, G. E. Douberly, Jr., *J. Phys. Chem. B* **2001**, *105*, 1683-1686. (b) R. Djalali, Y. F. Chen, H. Matsui, *J. Am. Chem. Soc.* **2002**, *124*, 13660-13661.
- [30] J. Bijma, H. J. Spero, D. W. Lea, in *Use of Proxies in Paleoceanography, Examples from the South Atlantic*, Eds. G. Fischer, G. Wefer, Springer, Berlin, Heidelberg, **1999**, pp. 489.
- [31] Y. Levi, S. Albeck, A. Back, S. Weiner, L. Addadi, *Chem. Eur. J.* **1998**, *4*, 389-396.
- [32] J. Aizenberg, J. Hanson, T. F. Koetzle, L. Leiserowitz, S. Weiner. *Chem. Eur. J.* **1995**, *1*, 414-422.
- [33] N. Bouropoulos, S. Weiner, L. Addadi, *Chem. Eur. J.* **2001**, *7*, 1881-1888.
- [34] M. N. Tahir, P. Theato, W. E. G. Müller, H. C. Schröder, A. Janshoff, J. Zhang, J. Huth, W. Tremel, *Chem. Comm.* **2004**, 2848-2849.
- [35] J. L. Sumerel, W. Yang, D. Kisailus, J. C. Weaver, J. H. Choi, D. E. Morse, *Chem. Mater.* **2003**, *15*, 4804-4809.
- [36] M. N. Tahir, P. Théato, W. E. G. Müller, H. C. Schröder, A. Borejko, S. Faiß, A. Janshoff, J. Huth, W. Tremel, *Chem. Comm.* **2005**, 5533-5535.
- [37] D. Kisailus, M. Najarian, J. C. Weaver, D. E. Morse, *Adv. Mater.* **2005**, *17*, 314-318.
- [38] O. V. Kaluzhnaya, S. I. Belikov, H. C. Schröder, M. Wiens, M. Giovine, A. Krasko, I. M. Müller, W. E. G. Müller, *Naturwiss.* **2005**, *92*, 128-133.
- [39] W. E. G. Müller, A. Krasko, G. L. Penec, R. Steffen, M. S. A. Ammar, M. Wiens, I. M. Müller, H. C. Schröder, *Progr. Mol. Subcell Biol.* **2003**, *33*, 195-221.

5. Facile Synthesis and Characterization of Functionalized, Monocrystalline Rutile TiO₂ Nanorods

5.1. Introduction

One dimensional (1D) inorganic materials (such as rods, wires, whiskers, belts and tubes)^[1] have been a target for the vigil eyes of attraction for nanotechnologist, owing to the wide range of electrical and optical properties that depend on both size and shape.^[2] So the development of improved pathways for the synthesis of nanomaterials, with control of particle, size, shape and crystallinity is the fundamental object of modern materials chemistry. TiO₂ possesses interesting optical, dielectric and catalytic properties, which result in industrial applications such as pigment, dyes sensitized solar cells,^[3] filters for catalysts support and in photocatalysis.^[4,5,6] As a pure component or combined with other elements, TiO₂ has been associated with improved sensitivity to humidity, oxygen,^[7] enhanced mechanical properties,^[8] and catalytic activity,^[9] and it has also been used in membrane separations involving chemical reactions^[10].

Being non-toxic, TiO₂ is promising to create chemical and biological hybrid nanocomposites that can be introduced into cells which can further be used to initiate, intracellular processes as well as bio tracers.^[11] Moreover, TiO₂ have been recognized to make hydroxyapatite-titania composites to provide bio-compatible materials.^[12] A common strategy for the surface functionalization of TiO₂ (and other oxides) is based on anchor groups using chelating ligands such as alkendiols, which can carry additional functionalities to explore further applications of these materials.^[13] In order to get desirable applications from nanomaterials, reactive organic groups have to be attached to the surface of the inorganic nanocrystals. Niederberger et al. have described the synthesis of anatase TiO₂ nanoparticles with an amine functionalized surface.^[14]

Titania has three crystalline polymorphs: anatase, rutile and brookite. Each phase has different physical properties, such as refractive index, chemical reactivity, and photochemical reactivity. Therefore, it is important to develop synthetic methods in which the crystalline form as well as the size and shape of the TiO₂ nanocrystals can be controlled. Among three polymorphs of TiO₂, the rutile phase exhibits an excellent combination of physical properties which have made it the most widely used white pigment on the world market due to its

exceptional light scattering efficiency, high refractive index, opacity, chemical inertness,^[15,16] and superb photocatalytic properties.^[17] But unlike anatase, the synthesis of rutile TiO₂ nanocrystals is much more difficult as most of the methods adopted for the synthesis of TiO₂ generally produce the kinetically controlled polymorph, anatase, at low temperatures.^[18]

So far, many groups have carried out significant work to explore novel methods to prepare nanocrystalline rutile TiO₂ controlling size, morphology as well as related properties.^[19,20,21,22,23,] Some groups have used rutile TiO₂ as seed crystals to accelerate the crystallization of rutile TiO₂.^[24] while others use NaCl and SnCl₄ as mineralizers to obtain rutile TiO₂ nanocrystals.^[23] The drawback in using rutile TiO₂ as a seed crystal is a decrease in the yield of rutile for higher concentrations of the starting TiCl₄ solution, and anatase TiO₂ is formed as a side product. In the presence of SnCl₄ and NaCl as mineralizers, the products got agglomerated and the mineralizers existed in the product as contamination. Huang et al.^[25] provided a method to synthesize rutile TiO₂ nanorods, but this procedure requires highly acidic and oxidizing (HNO₃) media which does not allow any useful *in situ* functionalization. Herein, we report on the synthesis of *in situ* surface functionalized, monocrystalline rutile TiO₂ nanorods, using a hydrothermal method (operating under mild conditions) which gives us the control on size, morphology, as well as crystal modification of the product. These rutile TiO₂ nanorods offer amine group functionality on the surface which offers excellent prospects to prepare future TiO₂-nanobiocomposites and -biotracers. As an example, this surface functionality is used for the covalent binding of a fluorescent dye, 4-chloro-7-nitrobenzylurazene (NBD) to the TiO₂ nanorods.^[26]

The TiO₂ nanorods were synthesized using a hydrothermal procedure. Briefly, TiCl₄ was dropped to ice-cooled water, following the addition of Na₂CO₃ solution. To the preformed TiO₂, 3-hydroxytyramine was added as a functionalization agent. Aging and hydrothermal treatment at 150°C for 13 hours resulted in the formation of functionalized rutile nanorods.

5.2. Results and discussion

Figure 5.1 shows the X-ray diffraction (XRD) pattern of the synthesized dopamine functionalized nanorods. All reflections can be indexed to rutile with (110), (211) and (101) as strongest reflections. In the powder pattern no traces of other TiO₂ polymorphs could be

detected, i.e. the crystalline material can be considered single phase. Based on the half-width Δ , the (101) reflection in the powder pattern is sharper than the (110) reflection, which indicates that the product grows anisotropically. The average grain size L determined from the broadening of the (110) reflection by the Scherrer formula $L = 0.9\lambda / \Delta \cos \theta$ is approx. 15

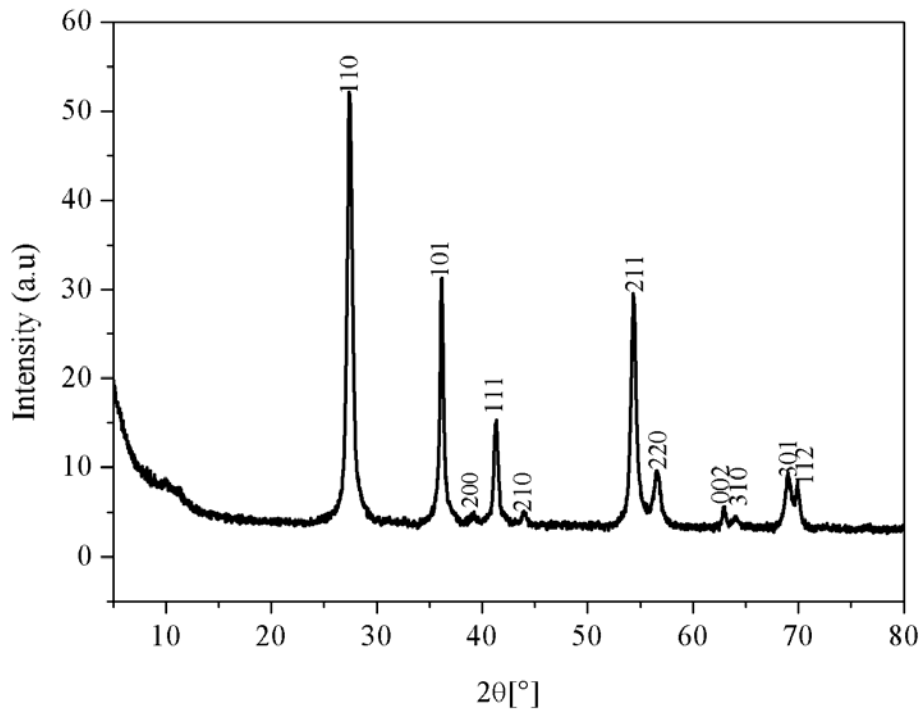


Figure 5.1. XRD powder pattern of as-synthesized amine functionalized rutile TiO_2 nanorods.

nm which is close to the diameter of the nanorods.

Representative transmission electron microscopy (TEM) images of functionalized TiO_2 nanorods are provided in Figure 5.2. An overview of the nanorods at low magnification in Figure 5.2a shows that the sample contains almost exclusively nanorods with uniform length up to 80 nm and diameters of approx. 15-16 nm. The corresponding high resolution TEM (HRTEM) images are given in Figure 5.2(b and c). The single crystal nature of the nanorods, with perfect perfect rutile structure, is clearly visible. The fringe spacing parallel to the main axis of the nanorod is estimated to be 0.32 nm, similar to the findings of Huang et al.²⁵ This is close to the (110) lattice spacing of rutile TiO_2 , indicating that crystal growth is preferential in the [110] direction, which results in an anisotropic growth of nano-crystals, leading to elongated nanoparticles (nanorods).

Furthermore, the diffraction pattern shown in the Figure 5.2c, taken from the corresponding nanorod is consistent with the rutile TiO_2 .

Anisotropic crystal growth results in rod formation, which is usually achieved when the surface free energies of different crystallographic planes differ significantly.

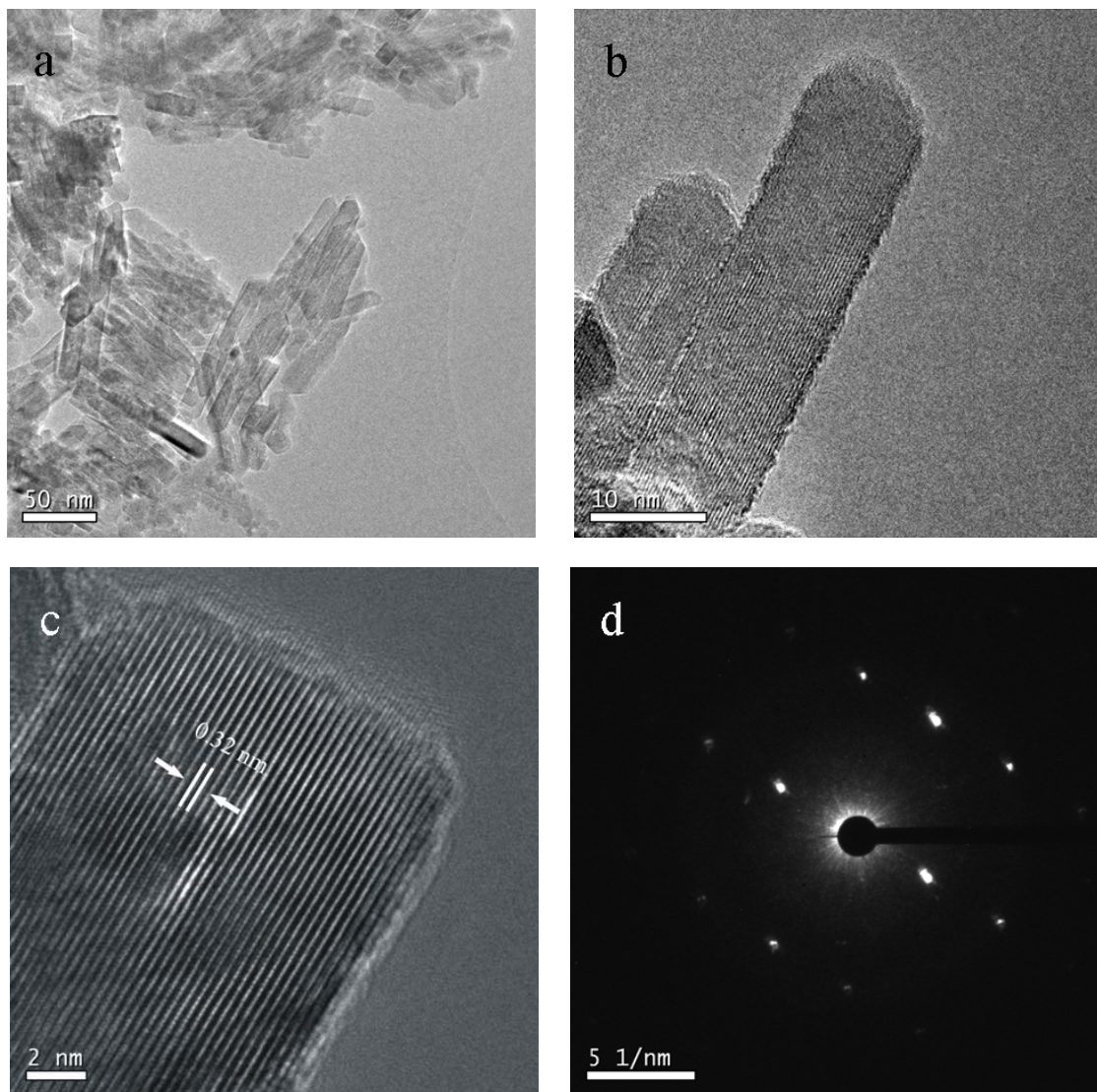


Figure 5.2. TEM micrographs of the rutile TiO_2 nanorods: overview image (a), HRTEM image (b) and (c). Figure 2d shows the electron diffraction pattern of a TiO_2 nanorod.

The case of different surface ligands which bind selectively to the respective surface planes has already been previously demonstrated as suitable approach for rod formation in a controlled manner.^[27]

In our system, the tendency for unidirectional growth of TiO₂ nanorods can be understood as arising from the selective adsorption of dopamine through its OH groups onto undercoordinated Ti surface atoms, resulting in the formation of a bidentate surface complex, which plays an important role in controlling the crystal phase and growth direction.^[26] As discussed by Yan et al.^[28] the surface bound dopamine forms a “screening layer” which renders the product monocrystalline rutile.

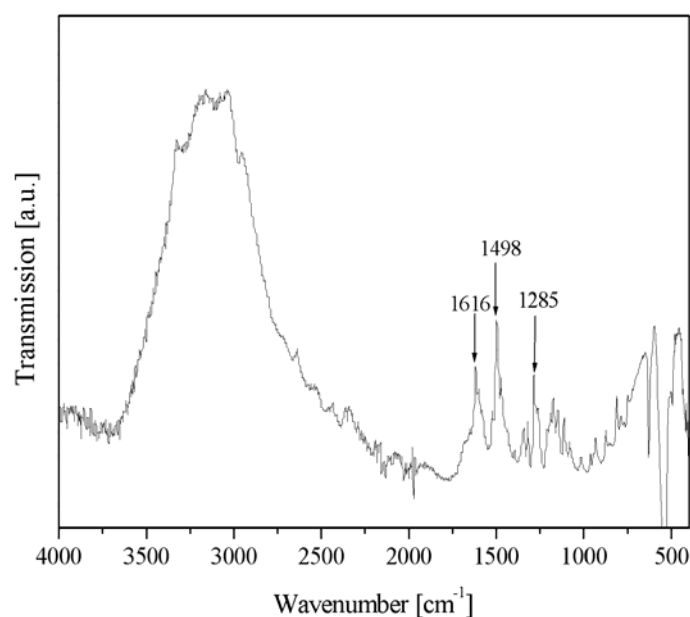


Figure 5.3. FT-IR data of as synthesized Functionalized TiO₂ nanorods

The functionalized TiO₂ nanorods were further characterized by means of IR spectroscopy. A typical FT-IR spectrum in the region between 4000 – 400 cm⁻¹ of dopamine functionalized TiO₂ nanorods is presented Figure 5.3. Above 2000 cm⁻¹, the IR spectrum is dominated by the O-H broad stretching peak centered at 3300 cm⁻¹. This peak is due to titanol groups or adsorbed H₂O. Superimposed are the C-H stretching vibrations at 2960 cm⁻¹ of the –CH₂– groups of the hydrocarbon moiety and the C-H stretching vibrations at 3040 cm⁻¹ attributable to the aromatic groups. Below 2000 cm⁻¹ the peaks for the amino group, the N-H bending can be assigned to 1616 cm⁻¹. The contributions of the aromatic –C-H bending, resulting in two peaks, can only be assigned to the peak at 1498 cm⁻¹, while the second peak around 1600 cm⁻¹

cannot be unambiguously discerned, owing to the possible coincidence of the amine signal at 1616 cm^{-1} in the same spectral region.

The peak at 1285 cm^{-1} can be assigned to the C-O stretching. In the fingerprint region (below 1000 cm^{-1}) the expected 1,2,4 trisubstitution can be revealed by the peaks at 876 cm^{-1} and 814 cm^{-1} . However, the characteristic vibrations of the inorganic Ti-O-Ti network in titanium dioxide below 950 cm^{-1} are overlaid, which results in a poor signal-to-noise ratio of the organic moiety.

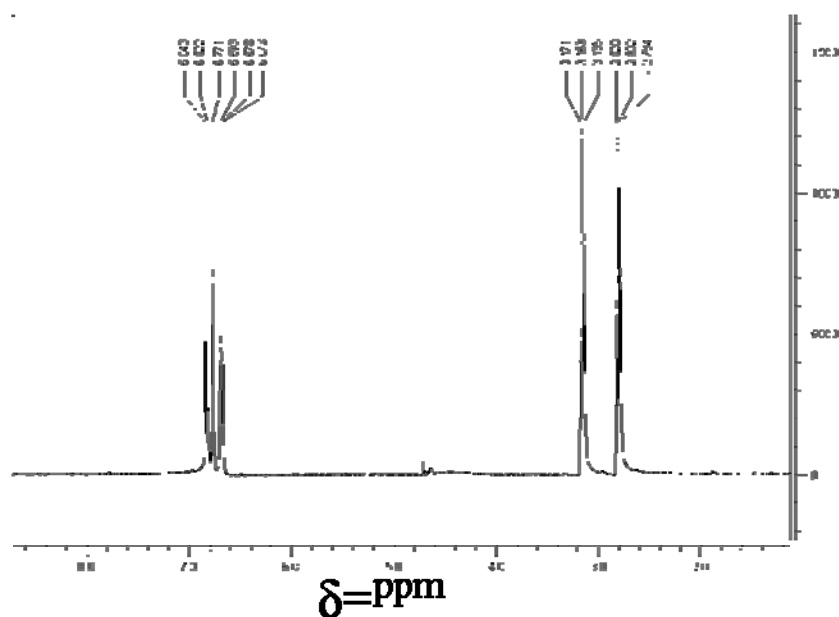


Figure 5. 4. NMR data of as synthesized TiO_2 nanorods.

Further $^1\text{H-NMR}$ characterization of functionalized TiO_2 nanorods proved the presence of dopamine. The $^1\text{H-NMR}$ spectrum (Figure 5.4) contains three peaks. The three aromatic protons give rise to three signals at 6.83 ppm, 6.77 ppm, and 6.68 ppm, respectively, revealing the 1,2,4 trisubstitution pattern of the aromatic ring. A slight shift of all aromatic protons by 0.04 ppm towards low field – compared to pure dopamine - can be attributed to the complexation phenomenon of dihydroxy groups with titanium. The signals of the two aliphatic CH_2 groups appear as two triplets at 3.15 ppm and 2.80 ppm, respectively. Due to the presence of NH_2 , the triplet at 3.15 ppm can be assigned to the CH_2 group adjacent to NH_2 .

A nice macroscopic evidence, as shown in Figure 5.5, that the 3-hydroxytyramine is really bonded to the surface of the nanorods, is the fact that the nanorods display strongly different solubilities at different pH values in aqueous solutions due to the amphiphilic behaviour of the amine group. In an acidic medium ($\text{pH} < 3$) the amine group is protonated and it is impossible to precipitate the nanorods, i.e. a stable suspension is formed, as shown in Figure 5.5a. This solution is stable over months and even centrifugation at 4000 rpm for 10 minutes did not show any indication of precipitation. The protonation of amine groups on the surface of the nanorods is responsible for their dispersability. When the pH is increased to basic conditions ($\text{pH} > 9$), the nanorods precipitated within a few minutes, even without centrifugation (see Figure 5.5b). The nanorods are insoluble in water, because the amine groups on the surface are not protonated under these pH conditions. If the pH is again decreased to acidic conditions

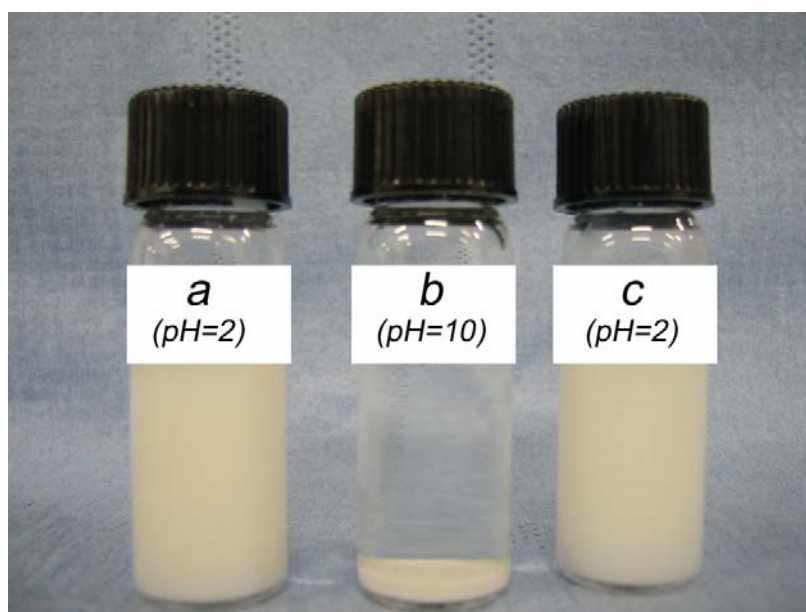


Figure 5.5. Photographs of amino functionalized TiO_2 nanorods in water: suspension at $\text{pH} = 2$ (a), precipitate at $\text{pH} = 10$ (b), and re-suspension at $\text{pH} = 2$ (c).

($\text{pH} < 3$) the nanorods are fully dispersible again (Figure 5.5c).

Nano-rutile TiO_2 has important applications as UV absorbent in cosmetics, pigments and plastics instead of organic UV absorbents because of its high absorbance for ultraviolet light and its non-toxicity. Figure 5.6b shows the UV-VIS absorption spectrum of dopamine functionalized rutile TiO_2 nanorods at a concentration of 1 mg/mL. Noteworthy, a clear absorption maximum at 322 nm characteristic for rutile TiO_2 nanocrystals can be observed.²⁴

In order to demonstrate the potential functionalization possibilities of the synthesized nanorods we attached a fluorescent dye (4-chloro-7-nitrobenzylurazene, NBD), as shown in

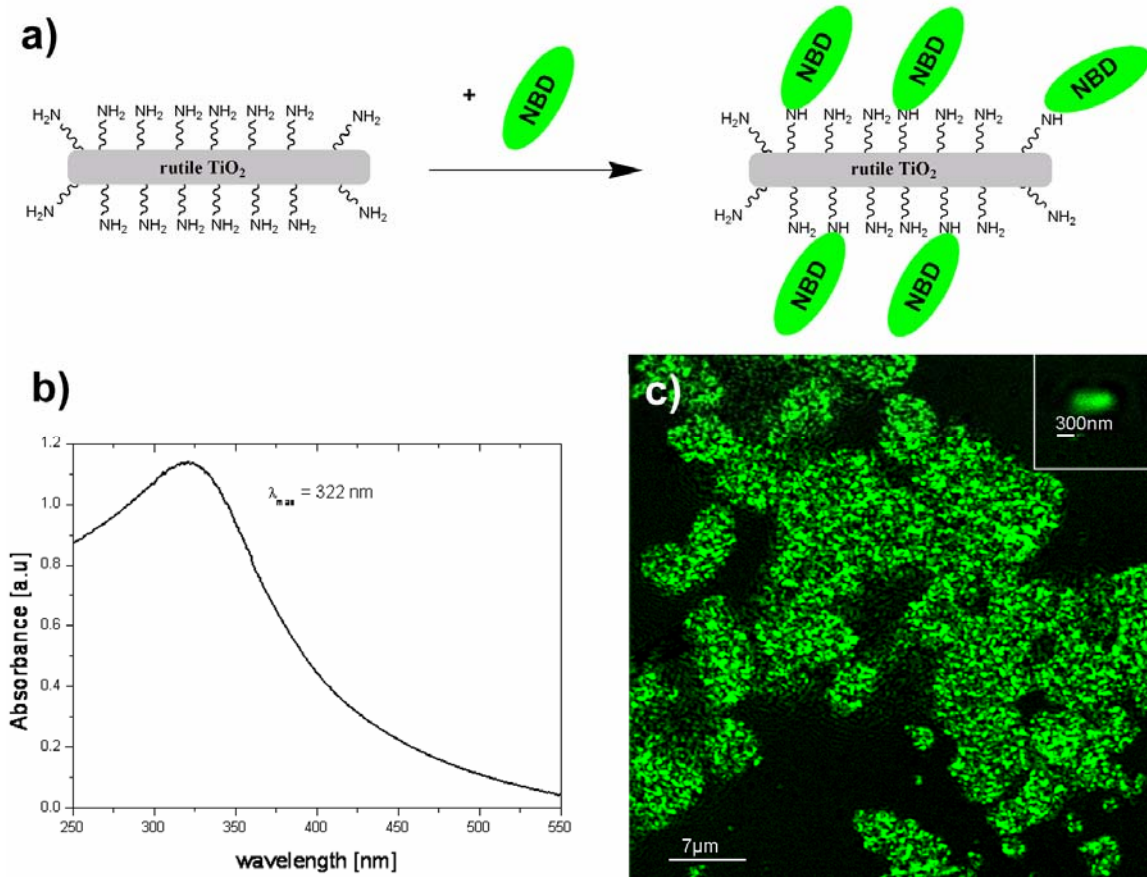


Figure 5.6. Schematic illustration of the binding of the fluorescent dye NBD to the surface functionalized rutile TiO₂ nanorods (a). UV-VIS absorption spectrum of amine functionalized rutile TiO₂ nanorod solution in water (b). Confocal LASER scanning microscopy image of dye functionalized nanorods at 488 nm excitation (c).

Figure 5.6a. After labelling the TiO₂ nanorods with the fluorescent dye NBD, they were characterized by means of confocal laser scanning (CLS) microscopy. The results are presented in Figure 5.6c. Clearly, green fluorescent agglomerates can be seen, proving the successful binding of NBD onto the TiO₂ nanorods. The inset picture of the CLS in Figure 5.6c shows an isolated fluorescently labelled object. As the size of our nanorods is smaller than the resolution of the microscope, it is hard to comment on the real size of the nanorod.

Nevertheless, the isolated fluorescent labelled object could be a single nanorod. In the present study we demonstrated that rutile TiO₂ nanorods with dimensions of 15 x 80 nm can be synthesized under mild conditions in high yield in a facile and reproducible manner.

5.3. Conclusion

Establishing a versatile procedure gave us not only the control on size, morphology and crystallinity, but also on surface functionalization. The reaction conditions used in the synthesis allow the *in situ* functionalization of the rutile TiO₂ nanorods. As an example, we show that surface bound amine groups can bind covalently to the fluorescent dye NBD. This technique of tailored surface functionalization opens further possibilities for improving the quality of rutile pigments or the fabrication of conducting polymer/TiO₂ thin films, which would enhance the performances of some electronic or optoelectronic devices based on such nanocomposite thin films (e.g. photovoltaic or electroluminescent devices).

5.4. Experimental

In a typical synthesis, 1.5 mL of TiCl_4 was added to 6 mL of distilled water with in ice water bath under constant stirring. The reaction mixture was stirred until it became clear again. Then a 2.1 M aqueous solution of Na_2CO_3 (17 mL) was added dropwise into the transparent Ti-containing solution to obtain a white suspension at $\text{pH} = 10$. To this mixture, 56.9 mg of 3-hydroxytyramine hydrogen chloride (0.3 mmol) were added under constant stirring and the reaction mixture was heated at $60\text{ }^\circ\text{C}$ for 1 hour. Afterwards the product was washed 4 times with water by centrifugating the precipitate off in order to remove excess of ligand and Na_2CO_3 . 3 mL of water was added to suspend the precipitate and the pH was adjusted to 0.5 by adding dropwise 15% HNO_3 . The suspension was allowed to age at room temperature for 3 hours and then was autoclaved in a steel jacketed Teflon lined autoclave at $150\text{ }^\circ\text{C}$ for 13 hours. After hydrothermal treatment, the product was purified by washing with water, as described above, and dried under vacuum at room temperature.

The attachment of NBD was performed as follows. 10 mL suspension of dopamine functionalized rutile TiO_2 nanorods ($c = 1\text{ mg/mL}$) in THF was mixed with 10 mL of a NBD solution (10 mmol) in THF. The mixture was stirred for 24 hours in the absence of light at room temperature. The product was purified by subsequently washing with CHCl_3 and afterwards dried in vacuum.

5.5. References

- [1] Z. W. Pan, Z. R. Dai, Z. L. Wang, *Science* **2001**, *291*, 1947-1949.
- [2] P. D. Cozzooli, A. Cornowski, H. Weller, *J. Am. Chem. Soc.* **2003**, *125*, 14539-14548.
- [3] G. Ramakrishna, H. N. Ghosh, *J. Phys. Chem. B* **2001**, *105*, 7000-7008.
- [4] E. W. McFarland, J. Tang, *Nature* **2003**, *421*, 616-618.
- [5] M. Anderson, L. Österlund, S. Ljungström, A. Palmqvist, *J. Phys. Chem. B* **2002**, *106*, 10674-10679.
- [6] B. O. Regan, M. Grätzel, *Nature* **1991**, *353*, 737-740.
- [7] Y. C. Yen, T. T. Tseung, D. A. Chang, *J. Amer. Ceram. Soc.* **1989**, *72*, 1472-1475.
- [8] T. Matsumoto, Y. Murakami, Y. Takasu, *Chem. Lett.* **2000**, *29*, 348-349.
- [9] R. Asahi, T. Morikawa, T. Ohwaki, K. Aoki, Y. Taga, *Science* **2001**, *293*, 269-271.
- [10] A. Chemseddine, H. P. Boehm, *J. Mol. Catal.* **1990**, *60*, 295-311.
- [11] T. Paunesku, T. Rajh, G. Wiederrecht, J. Maser, T. Vogt, N. Stojicevic, M. Protic, B. Lai, J. Oryhon, M. Thurnauer, G. Woloschak, *Nature Mater.* **2003**, *2*, 343-346.
- [12] H. W. Kim, H. E. Kim, V. Salih, J. C. Knowels, *J. Biomed. Mater. Res.* **2005**, *72*, 1-8.
- [13] (a) C. Xu, K. Xu, G. Gu, R. Zheng, H. Liu, X. Zhang, Z. Guo, B. Xu, *J. Am. Chem. Soc.* **2004**, *126*, 9938-9939.
- (b) N. M. Dimitrijevic, Z. V. Saponjic, B. M. Rabatic, T. Rajh, *J. Amer. Chem. Soc.* **2005**, *127*, 1344-1345.
- [14] M. Niederberger, G. Garnweitner, F. Krumeich, R. Nesper, H. Cölfen, M. Antonietti, *Chem. Mater.* **2004**, *16*, 1202-1208.
- [15] E. S. Thiele, R. H. French, *J. Am. Ceram. Soc.* **1998**, *81*, 469-479.
- [16] T. C. Patton, *Pigment Handbook*, Wiley, New York, **1973**.
- [17] Y. Li, N. H. Lee, E. G. Lee, J. S. Song, S. J. Kim, *Chem. Phys. Lett.* **2004**, *389*, 124-128.
- [18] S. T. Aruna, S. Tirosh, A. J. Zaban, *J. Mater. Chem.* **2000**, *10*, 2388-2391.
- [19] W. Wang, B. Gu, L. Liang, W. A. Hamilton, D. J. Wesolowski, *J. Phys. Chem. B* **2004**, *108*, 14789-14792.
- [20] A. Fujishima, K. Honda, *Nature* **1972**, *238*, 37-38.
- [21] N. G. Park, G. Schlishtor, J. van de Lagemat, H. M. Cheong, A. Mascarenhas, A. Frank, *J. Phys. Chem* **1999**, *103*, 3308-3314.

- [22] K. N. P. Kumar, K. Keizer, A. J. Burggraaf, *J. Mater. Sci. Lett.* **1994**, *13*, 59-61.
- [23] H. Cheng, J. Ma, Z. Zhao, L. Qi, *Chem. Mater.* **1995**, *7*, 663-671.
- [24] Y. Li, Y. N. Fan, Y. Chen, *J. Mater. Chem.* **2002**, *12*, 1387-1390.
- [25] Q. Huang, L. Gao, *Chem. Lett.* **2003**, *32*, 638-639.
- [26] R. Nudelman, O. Ardon, Y. Hadar, Y. Chen, J. Libman, A. Shanzer, *J. Med. Chem.* **1998**, *41*, 1671-1678.
- [27] (a) X. Peng, L. Mana, W. Yang J. Wickhman, E. Scher, A. Kadavanich, A. P. Alivisatos, *Nature* **2000**, *404*, 59-62.
(b) Y. Sun, Y. Xia, *Science* **2002**, *298*, 2176-2179.
- [28] M. Yan, F. Chen, J. Zhang, *Chem. Lett.* **2004** , *33*, 1352-1353.

6. Reactive Polymers, a Versatile Toolbox for the Immobilization of Functional Molecules on TiO₂ Nanoparticles

6.1. Introduction

The nanoengineering of particle surfaces is a key for the design and tailored construction of innovative nanomaterials.^[1] Having control of the inorganic nanoparticle surfaces allows one to tailor the particle size^[2] and solubility.^[3] Moreover, the surface characteristics of nanomaterials influence the broad range of properties and the performance of a large variety of devices. For instance, the charge transport process across the interface between a semiconductor metal oxide and an organic dye^[4] or a biomolecule^[5] forms the basis for improving the performance of many optoelectronic devices, photovoltaic cells^[6] and light emitting diodes (LEDS).^[7] Oligonucleotides can also be linked to surfaces of nanoparticles, which may become a new tool for gene therapy.^[8]

To connect the inorganic nanomaterials to the organic moiety in hybrid materials by strong covalent or ionic interactions, reactive organic groups have to be attached on the surface of inorganic component.^[9] Surface modification of nanomaterials can be achieved by two methods, grafting of organic groups to surface of nanomaterials after synthesis (post-functionalization)^[10] or *in situ* modification of nanomaterials by organic compounds (*in situ*-functionalization).^[11] In particular, nanocrystalline TiO₂ is attractive for several applications, such as photocatalysis,^[12] solar cells,^[13] membranes,^[14] sensors,^[15] nanoceramics,^[16] and for degrading environmental hazardous chemicals.^[17]

In this communication, we introduce a new versatile polymeric ligand which can be used for *in-situ* - and *post-functionalization* of TiO₂ as well as for other metal oxide nanomaterials.^[18]

The multifunctional polymeric ligand combines three properties: (i) a robust anchor group based on dopamine, capable of binding to many metaloxides (TiO₂, Fe₂O₃, etc.),^[19] (ii) a functional molecule (fluorescent dye, catalysts, biological molecules, etc.), and (iii) an outer group to provide solubility in different solvents, thereby allowing to tune the application of the inorganic nanomaterials (e.g. solubility of TiO₂ pigments, directed binding to biological targets etc.).

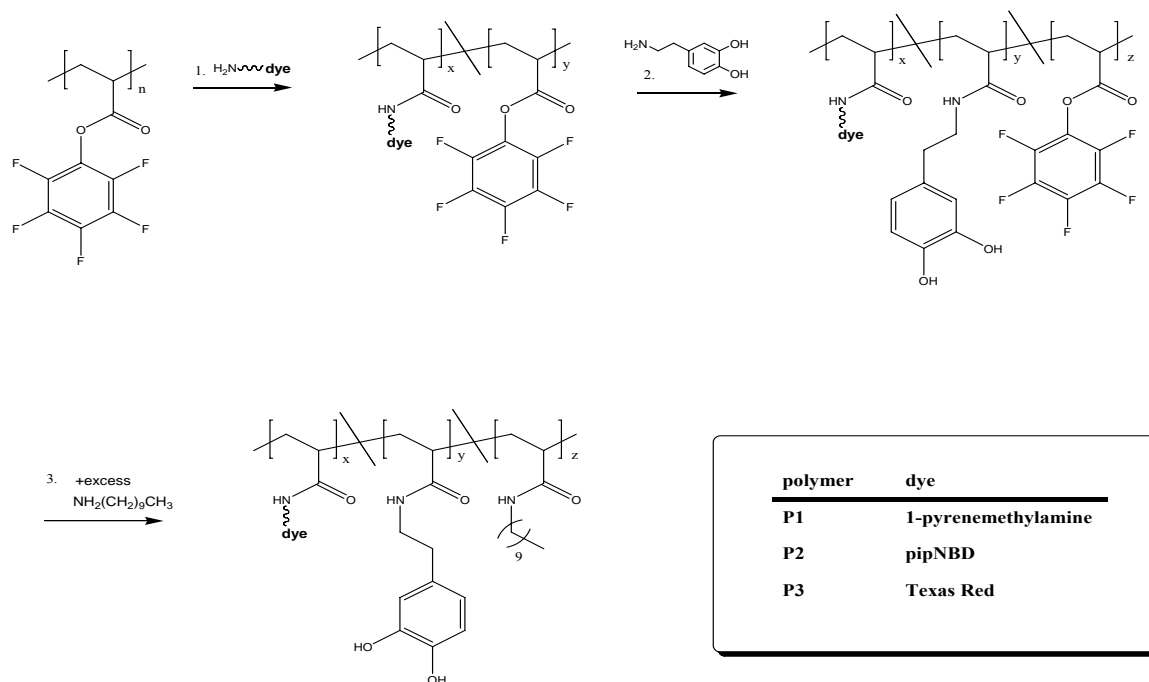


Figure 6.1. Stepwise synthesis of the multifunctional polymeric ligand containing a dye. The active ester units of the polymer are successively exchanged by 1-pyrenemethylamine (**P1**), pipNBD (**P2**) and Texas Red (**P3**), respectively. The polymer contains 3-hydroxytyramine as anchors for the nanoparticles, alkyl chains for solubility and dye molecules.

The architecture of the polymeric ligand is of major importance, because it provides the basis of a comprehensive toolbox to construct supramolecular assemblies of organic-inorganic hybrid nanomaterials. Moreover, this strategy of functionalization can be extended by introducing suitable anchor groups for nanomaterials other than metal oxides.^[20a]

The fact that active ester polymers react fast and quantitatively with amines to form the corresponding poly(acrylamides), opens the possibility to obtain multifunctional polymeric materials.^[19] Active ester polymers based on pentafluorophenylacrylates exhibit some outstanding features compared to the commonly used poly (N-hydroxysuccinimide-acrylates): better solubility and higher reactivity, as we have already described elsewhere.^[20b]

The synthesis of the multifunctional polymeric ligand starting from this precursor polymer is shown in Figure 6.1.

The active ester polymer was prepared by free radical polymerization yielding a polymer with molecular weight $M_n = 29.7$ kg/mol and $M_w = 58.5$ kg/mol (PDI = 1.96). This pre-polymer was then transformed into the multifunctional polymeric ligand by substituting with amino-

group containing functionalities. Polymers **P1**, **P2**, and **P3** were prepared by a stepwise substitution of the active ester groups: firstly by addition of fluorescent dyes (1-pyrenemethylamine **PyMA**, piperazinyl-4-chloro-7-nitrobenzofurazane **pipNBD**, and Texas Red, respectively), secondly by reaction with the 3-hydroxytyramine anchor groups and, finally, by quenching with decylamine. In summary, the resulting polymer exhibits three different properties: (i) a fluorescent dye as a functional demonstrator molecule (ii) 3-hydroxytyramine as anchor groups for attachment onto the metal oxide nanoparticles and (iii) a long alkyl chain to increase solubility in nonpolar solvents. The obtained multifunctional polymers have been analyzed by $^1\text{H-NMR}$, FT-IR and GPC in order to determine the composition of the polymers. Within the polymers **P1**, **P2**, and **P3** the respective dye contents were determined to 10 mol%, while 10 mol% of 3-hydroxytyramine were incorporated. The remaining 80 mol% was N-decylacrylamide repeating units.

For the *in-situ* functionalization of the TiO_2 nanocrystals, TiCl_4 was injected into the solution of the polymeric ligand in benzyl alcohol. The solution was stirred for two days at 80°C under argon atmosphere. Post-functionalization was achieved by sealing a mixture of TiO_2 nanowires (synthesized from conc. NaOH and titanium isopropoxide) and 10 ml of polymeric ligand in benzyl alcohol. In both cases the product was repeatedly washed with CH_2Cl_2 to remove the unreacted ligand. The functionalized TiO_2 nanocrystals were characterized by TEM, XRD, $^1\text{H-NMR}$, confocal laser scanning microscopy (CLSM) and fluorescence spectrophotometry.

6.2. Results and discussion

Transmission electron micrographs of synthesized TiO_2 nanowires and TiO_2 nanoparticles are shown in Figure 6.2. An overview of the nanowires is given in Figure 6.2a. These nanowires have been used for post-functionalization. Figure 6.2(b and c) show the TEM images of the *in situ* synthesized functionalized TiO_2 nanoparticles (using **P1**, **P2**, and **P3**) at low magnification as well as at high resolution, respectively. At low magnification Figure 6.2b it can be seen that the sample consists almost exclusively of nanometer-sized TiO_2 particles arranged in a partly agglomerated fashion on a TEM grid.^[21] Even though it is difficult to identify isolated, individual TiO_2 particles because of the presence of the polymeric ligand, we present a HRTEM image of an isolated particle in Figure 6.2c.

Crystallinity and phase of the as-synthesized TiO₂ nanoparticles were confirmed by XRD

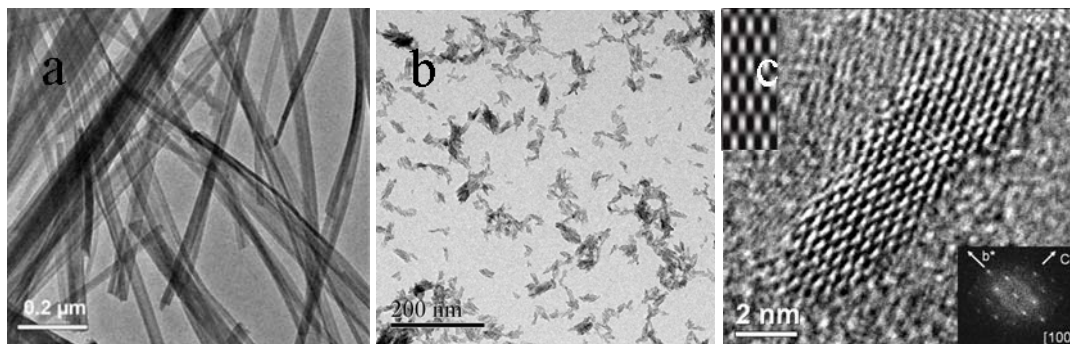


Figure 6.2. Transmission electron micrographs of (a) synthesized TiO₂ nanowires, (b) nanoparticles (overview image) and (c) HRTEM image of an individual nanoparticle. The Fourier Transform (FFT) is given in the lower right corner. A theoretical HRTEM image of the [100] zone is shown given in the upper left corner.

(Figure 6.3) and TEM (see inset of Figure 6.2c), revealing the characteristic diffraction patterns of anatase. Figure 6.2c shows a HRTEM image of a nanoparticle (diameter \approx 2 nm, length \approx 12 nm) in [100] view together with the Fourier transform (FFT) in the lower right corner. The distances calculated are in good agreement with the theoretical values of anatase reflection of the [100] zone ($d_{\text{exp}}/d_{\text{theo}}$ [Å]: (011) = 3.57/3.51; (004) = 2.40/2.38; (020) = 1.94/1.89). The theoretical HRTEM image of the [100] zone (given in the upper left corner) has been calculated by a multi-slice method for a thickness of 2 nm at Scherzer focus and resembles the experimentally derived image nicely.

The crystallinity and the morphology of the TiO₂ nanoparticles are independent of the polymeric ligand **P1**, **P2**, or **P3** used in the synthesis. The X-ray diffraction (XRD) pattern of the as-synthesized polymer functionalized TiO₂ nanoparticles is shown in Figure 6.3. All reflections could be indexed to anatase with (101) as the strongest reflection (the calculated reflection positions are given as ticks on the abscissa for comparison). The width of the (004) in comparison to the (101) reflection is indicative of the preferred particle growth along the *c* direction. In the powder pattern no traces of other TiO₂ polymorphs could be detected, i.e. the crystalline material can be considered single phase. The peak broadening is due to the nanosized particles. A Pawley-fit^[22] of the XRD combined with Scherrer's formula^[23] delivered a particle size of 2 nm in *a* as well as in *b* direction and 12 nm in *c* direction. This is in good agreement with the particle shown in Figure 6.2c.

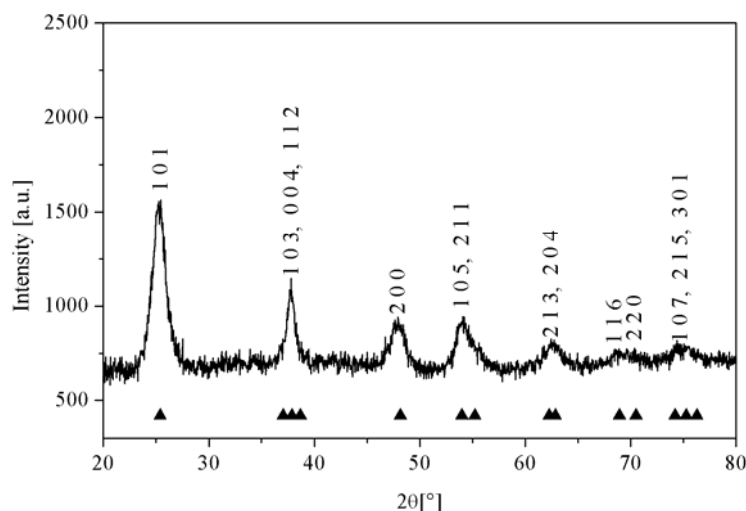


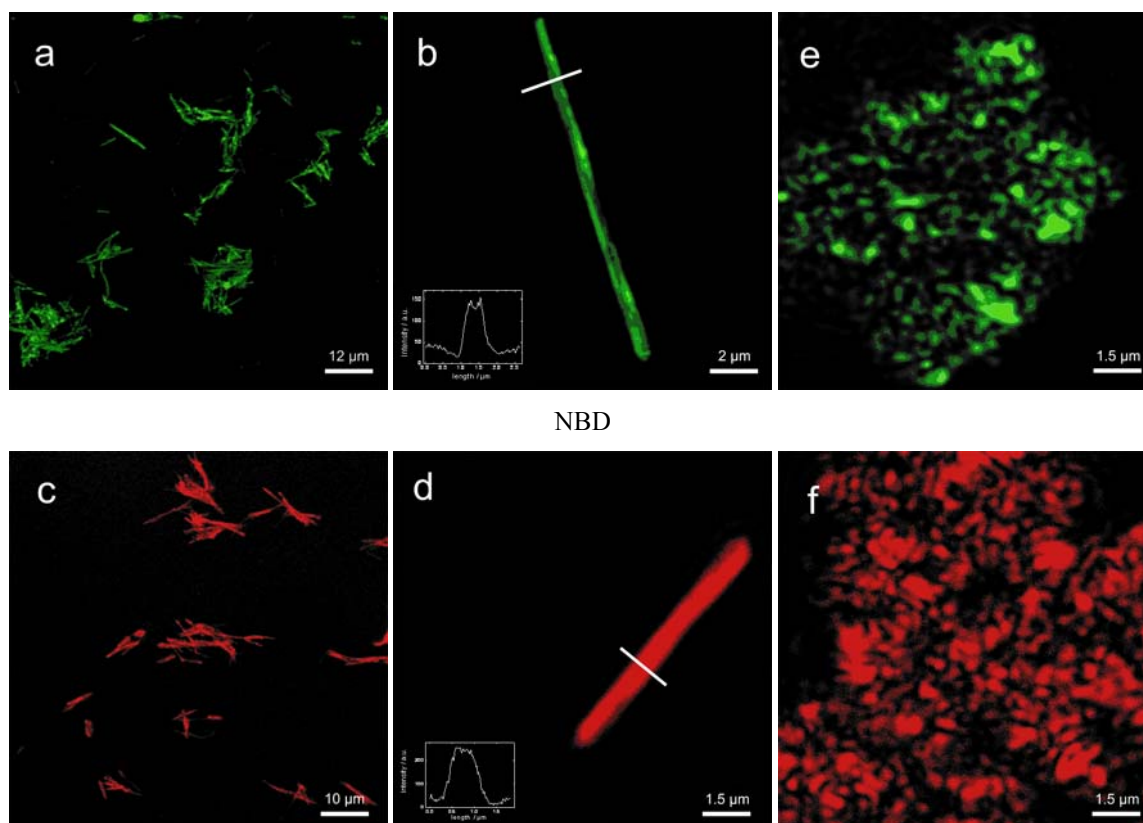
Figure 6.3. X-ray diffraction pattern of *in-situ* functionalized TiO₂ nanoparticles. The pattern can be fully indexed to anatase, indices of the reflections are marked. Calculated positions of the anatase reflections are indicated by black ticks.

It is noteworthy that all particles exhibit such a good crystallinity, despite the low reaction temperature of 80 °C and the presence of the chelating ligand (10% dopamine).

Figure 6.4 shows the confocal laser scanning microscopy images of TiO₂ nanowires and nanoparticles after surface functionalization with **P2** and **P3**, respectively.

A 10 µl droplet of the sample was placed and dispersed carefully on a thin glass slide and the solvent was evaporated. **P2**-functionalized nanowires and nanoparticles were imaged using an argon laser with an excitation wavelength of 488 nm, for the **P3**-functionalized nanowires and nanoparticles the 543 nm line of a helium/neon laser was used. A 40x (NA 1.25) oil immersion objective was used for the imaging of all samples.

Overview images of as functionalized TiO₂ nanowires with polymeric ligands **P2** and **P3** are shown in Figure 6.4(a and c), while a single isolated nanowire can be seen in Figure 6.4(b and d). The corresponding *in-situ* functionalized nanoparticles using polymeric ligands **P2** and **P3** are shown in Figure 6.4(e and f). It is obvious from the fluorescence profiles (given in the inset of Figure 6.4(c and d) and images that the nanowires are fully coated by polymer ligands covalently bound to TiO₂ nanowires. The TiO₂ nanoparticles shown in Figure 6.4(e and f) also exhibit the respective fluorescent colors.



NBD

Texas Red:

Figure 6.4. Confocal Laser Scanning Microscopy images of TiO₂-nanowires (a-d) and *in situ*-functionalized nanoparticles (e and f). TiO₂ nanowires coated with **P2** (NBD, a and b) and **P3** (Texas Red, c and d), and TiO₂ nanoparticles *in situ*-functionalized with **P2** (NBD, e) and **P3** (Texas Red, f), respectively. The fluorescence profiles for post-functionalized TiO₂ nanowires are given in the inset of b and d.

It is difficult to comment on the actual size of the *in-situ* functionalized nanoparticles because it was beyond the resolution limits of CLSM. TiO₂ nanocrystals with surface bound dopamine have been used for biotin-avidin functionalization coupling. Dopamine binding is a standard method for the surface functionalization of metal oxides^[20] where the dopamine group preferentially binds to the edges of the TiO₂ nanocrystals (which have a higher surface energy).^[5a]

In contrast, full surface coverage, protection and concomitant functionalization with better control on solubility in organic solvents (Figure 6.5) can be achieved using the novel

copolymer ligand containing a large number of dopamine groups covalently linked to the polymer backbone where the nanoparticles are partly sheathed by surface bound anchor groups and partly by steric shielding through the polymer ligand. The versatile use of the functional polymeric ligands as an immobilizer for metal oxide nanowires and nanoparticles is demonstrated by the attachment of three different fluorescent dyes: pyrene (**P1**), NBD (**P2**) and Texas Red (**P3**), respectively. In order to detect the immobilization of the functional polymers on the TiO₂ surfaces, fluorescence spectra have been measured.

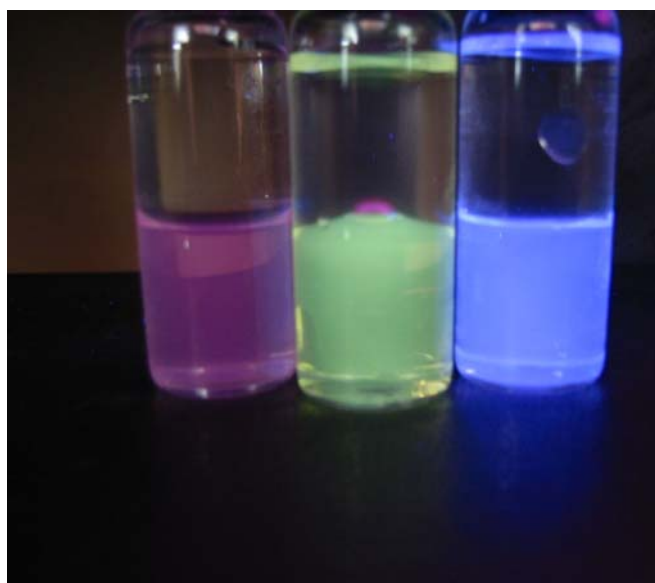


Figure 6.5. Digital camera photograph demonstrating the solubility of functionalized TiO₂ nanoparticles in chloroform/water under illumination with UV light ($\lambda = 365$ nm).

Figure 6.6 shows the fluorescence spectra of TiO₂ nanoparticles coated with **P1** (solid line), **P2** (dashed line) or **P3** (dotted line). All samples were dissolved in CHCl₃ for emission spectroscopy. A digital photograph giving evidence of the solubility in CHCl₃ is given in Figure 6.6 TiO₂ nanoparticles carrying the **P1** pyrene fluorophore were excited at 345 nm. TiO₂ nanoparticles coated with **P2** were excited at 460 nm, and the fluorescent spectra for **P3** were recorded with an excitation wavelength of 488 nm. Clearly, the expected emission spectra of the respective dye can be seen, proving the flexible application of our functional polymeric ligands. The functional polymeric ligands have been used for post- and *in-situ*-

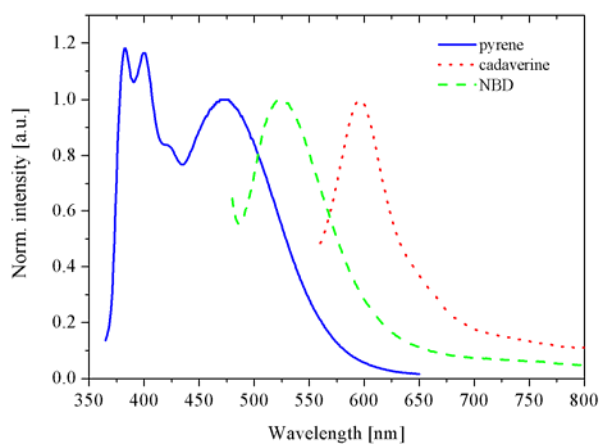


Figure 6.6. Fluorescence spectra of TiO_2 nanoparticles coated with **P1** (pyrene, solid line), **P2** (NBD, dashed line) or **P3** (Texas red, dotted line). TiO_2 nanoparticles carrying the **P1** pyrene fluorophore were excited at 345 nm. TiO_2 nanoparticles coated with **P2** were excited at 460 nm, and the fluorescent spectra for **P3** were recorded with an excitation wavelength of 488 nm.

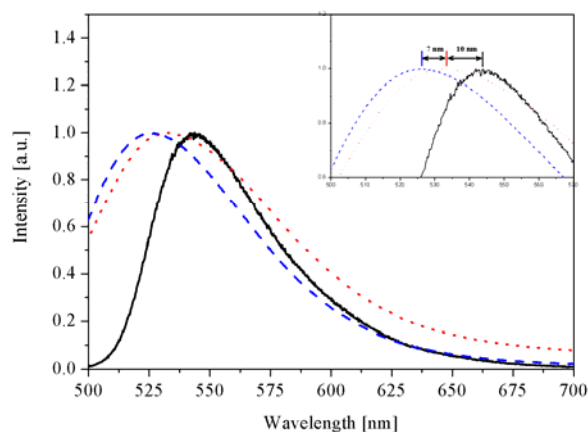


Figure 6.7. Fluorescence spectra of NBD depending on the preparation conditions. Solid line; emission spectrum of **P2** dissolved in CHCl_3 , TiO_2 particles coated with **P2** show a 10 nm blue-shifted maximum, whereas TiO_2 particles with the polymeric ligands (**P2**) show a blue shift of 17 nm with respect to **P2**.

functionalization of TiO₂ nanoparticles. Therefore, we investigated the fluorescence of **P2** depending on the synthetic procedure. The results are summarized in Figure 6.7. The solid line in Figure 6.7 shows the emission spectrum of **P2** dissolved in CHCl₃ as a reference. TiO₂ nanowires which have been coated with **P2** show a fluorescent spectrum with a 10 nm blue-shifted maximum whereas TiO₂ nanoparticles which were synthesized using the polymeric ligand (**P2**) show a blue shift of 17 nm with respect to **P2** in emission maximum. This can be understood as follows. The nanoparticles are coated with the polymer which results in a non-uniform environment for the dye molecules. As a result, the hydrophilic TiO₂ surface induces a slight blue-shift. This also explains the larger blue-shift for the *in situ*-functionalized nanoparticles as compared to post-functionalized nanowires, as the nanoparticles exhibit a larger surface-to-volume ratio.

6.3. Conclusion

In conclusion, we have demonstrated for the first time that reactive polymer ligands containing dopamine serve as robust anchor on the surface of titanium dioxide nanoparticles. Compared to the binding of molecules to the surface of oxide particles using dopamine the novelty and superiority of the polymeric ligand system presented here is based on its multifunctionality, as it incorporates metal chelating ligands, a functional molecule (pyrene, NBD, and Texas Red) and additional entities which allow tailoring the solubility of inorganic nanocrystals in different organic solvents for various potential applications. As a possible extension of the work presented we envisage the immobilization of proteins to metal oxide surfaces using nitrilotriacetic acid (NTA) as an anchor ligand,^[24] i.e. our simple strategy should provide a useful way to link biofunctional molecules in almost any solvent to the surface of metal oxide particles, which may have a high affinity to dopamine or any other linker group which may replace the dopamine ligand in the polymer. This strategy is extremely versatile and offers new opportunities for optoelectronic and/or biological applications of metal oxide nanoparticles. Finally, this strategy allows the arrangement of inorganic nanoparticles to build up supramolecular structures, e.g. by introducing biotin/streptavidin linker units as functional molecules.

6.4. Experimental

Piperaziny1-NBD **pipNBD** was synthesized according to the literature [1] by reaction of NBD chloride (Fluka) with an excess of piperazine in THF. 1-Pyrenemethylamine hydrochloride **PyMA** and Texas Red were commercially available (Aldrich).

The poly (active ester) poly(pentafluorophenylacrylate) **PFA** was prepared as reported earlier.^[20b] GPC analysis of the obtained polymer (THF, light scattering detection) gave the following values: $M_n = 29.7$ kg/mol; $M_w = 58.5$ kg/mol, where the number of repeating units (246) is based on the M_w value.

For the synthesis of the multifunctional poly(acrylamides), poly(active ester) poly(pentafluorophenylacrylate) (700 mg, 2.94 mmol repeating units) was dissolved in a mixture of 9 ml dry DMF and 0.7 ml triethylamine. The calculated amount of dye dissolved in dry DMF was added and the resulting solution stirred for 4 hours at 50°C. After that 3-hydroxytyramine hydrochloride (57 mg, 0.3 mmol) in 3 ml DMF and 1ml triethylamine was added and the clear solution kept for 2 hours at 50°C. In the final step the remaining active ester groups were quenched with an excess of decylamine (500 mg, 3.2 mmol). The polymer was isolated by precipitation in methanol, isolated and finally dried in a vacuum oven at 40°C for 1 hour.

100 mg of functional polymer ligand was dissolved in 20 ml of benzyl alcohol in a glovebox. The vial was sealed and taken out of the box. 0.8 ml of $TiCl_4$ was slowly injected through the septum to the benzyl alcohol-ligand solution under vigorous stirring at room temperature. With continuous stirring the solution was heated to 80°C for 24 hours. The resulting brown suspension was centrifuged and the precipitate was thoroughly washed twice with CH_2Cl_2 . The product was dried in air at room temperature.

1 g of Titanium isopropoxide (ACROS) was taken in a teflon vessel and 6 ml of analytical grade Ethanol (99.8 %) were added into it. The teflon vessel was kept in a desiccator. The precipitation of TiO_2 was initiated under moist atmosphere induced by placing a petri dish filled with water at the bottom of the desiccator. The diffusion experiment was stopped after 12 hours, followed by the addition of 25 ml of 10 M NaOH aqueous solution. Then the reaction vessel was sealed into a stainless steel hydrothermal bomb, which was placed in an oven maintained at 160 °C for 20 hours. After the autoclave was naturally cooled to room temperature, the obtained sample was filtered and repeatedly washed with 0.1 M HNO_3 , 1 N

HCl and deionized water. The product was dried under vacuum for 3 hours. Finally soft, fibrous powder with white colour was obtained. Then 10 mg of TiO₂ nanowires were dispersed in 10 ml of benzyl alcohol and sonicated for 15 minutes. In a separate vial 10 mg of polymer ligand were dissolved in 10 ml of benzyl alcohol. Both, suspension and solution were mixed under inert conditions and stirred at 60°C for four hours. Then polymer functionalized nanowires were isolated and purified by repeated washing with CH₂Cl₂ using centrifugation.

For confocal laser scanning microscopy, 10 µl of the sample was placed and dispersed carefully on a thin glass slide washed in piranha solution and the solvent was evaporated. NBD-functionalized nanowires were imaged using an argon laser with an excitation wavelength of 488 nm, for the Texas Red-functionalized nanowires the 543 nm line of a helium/neon laser was used. A 40x (NA 1.25) oil immersion objective was used for the imaging of all samples.

Instrumentation:

The resulting products were characterized by an inverted laser scanning microscope (Leica TCS SL, Leica Microsystems, Bensheim, Germany). X-ray powder diffraction in reflection geometry, (Siemens D8 powder diffractometer, Cu-K α radiation). High-resolution transmission electron microscopy (Philips TECNAI F30 electron microscope; field-emission gun, 300 kV extraction voltage) equipped with a high-angle annular dark-field detector (HAADF), a Gatan imaging filter (GIF), and an energy dispersive X-ray analysis (EDX) system.

6.5. References

- [1] S. Banerjee, M. G. C. Kahn, S. S. Wong, *Chem. Eur. J.* **2003**, *9*, 1898-1908.
- [2] P. D. Cozzoli, A. Kornowski, H. Weller, *J. Am. Chem. Soc.* **2003**, *125*, 14539-14548.
- [3] K. Ausman, R. Piner, O. Lourie, R. S. Rouff, M. D. Korobov, *J. Phys. Chem. B* **2000**, *104*, 8911-8915.
- [4] (a) R. Nudelman, O. Ardon, Y. Hadar, Y. Chen, J. Libman, A. Shanzer, *J. Med. Chem.* **1998**, *41*, 1671-1678.
- [5] (a) N. M. Dimitrijevic, Z. V. Saponjic, B. M. Rabatic, T. Rajh, *J. Amer. Chem. Soc.* **2005**, *127*, 1344-1345. (b) O. V. Salata, *J. Nanobiotechn.* **2004**, *2-3*, 1-6.
- [6] (a) G. Ramakrishna, H. N. Ghosh, *J. Phys. Chem. B* **2001**, *105*, 7000-7008.
(b) W. J. E. Beek, R. A. J. Janssen, *J. Mater. Chem.* **2004**, *14*, 2795-2800.
(c) E. W. McFarland, J. Tang, *Nature* **2003**, *421*, 6, 616-618.
- [7] J. W. Huang, S. J. Bai, *Nanotechnol.* **2005**, *16*, 1406-1410.
- [8] T. Paunesku, T. Rajh, G. Wiederrecht, J. Maser, T. Vogt, N. Stojicevic, M. Protic, B. Lai, J. Oryhon, M. Thurnauer, G. Woloschak, *Nature Mater.* **2003**, *2*, 343-346.
- [9] C. Xu, K. Xu, G. Gu, R. Zheng, H. Liu, X. Zhang, Z. Guo, B. Xu, *J. Am. Chem. Soc.* **2004**, *126*, 9938-9939.
- [10] G. Kickelbick, U. Schubert, *Synthesis, Functionalization and Surface Treatment of Nanoparticles*, Ed.: M. I. Baraton, American Scientific Publishers, Stevenson Ranch, CA, **2003**.
- [11] (a) C. Sanchez, G. S. Illia, F. Ribot, T. Lalot, C. R. Mayer, V. Cabuil, *Chem. Mater.* **2001**, *13*, 3061-3083. (b) M. Anderson, L. Österlund, S. Ljungström, A. Palmqvist, *J. Phys. Chem. B* **2002**, *106*, 10674-10679. (c) S. Yin, Y. Aita, M. Komatsu, J. Wang, Q. Tang, S. Sato, *J. Mater. Chem.* **2005**, *15*, 674-682.
- [12] S. Hore, E. Palomares, H. Smit, N. J. Bakker, P. Comte, P. Liska, K. R. Thampi, J. M. Karoon, A. Hinsh, J. R. Durrant, *J. Mater. Chem.* **2005**, *15*, 412-418.
- [13] A. Hagfeldt, M. Grätzel, *Acc. Chem. Res.* **2000**, *33*, 269-277.
- [14] B. S. Lele, A. J. Russell, *Biomacromolecules* **2004**, *5*, 1947-1955.
- [15] E. Palomares, R. Vilar, A. Green, J. R. Durrant, *Adv. Funct. Mater.* **2004**, *14*, 111-115.

- [16] M. Winterer, *Nanocrystalline Ceramics, Synthesis and Structure*, Springer, Heidelberg **2002**, Springer Series in Materials Science, Volume 53.
- [17] (a) J. H. Schattka, D. G. Shchukin, J. G. Jia, M. Antonietti, R. A. Carusa, *Chem. Mater.* **2002**, *14*, 5103-5108. (b) L. X. Chen, T. Rajh, Z. Y. Wang, M. C. Thurnauer, *J. Phys. Chem. B* **1997**, *101*, 10688-10697.
- [18] (a) J. L. Dalsin, L. Lin, S. Tosatti, J. Vörös, M. Textor, P. B. Messersmith, *J. Am. Chem. Soc.* **2005**, *127*, 34-35.
- [19] N. M. Dimitrijevic, Z. V. Saponjic, B. M. Rabatic, T. Rajh, *J. Am. Chem. Soc.* **2005**, *127*, 1344-1345.
- [20] (a) I. Potavova, R. Mruk, S. Prehl, R. Zentel, T. Basche, A. Mews, *J. Am. Chem. Soc.* **2003**, *125*, 320-321. (b) M. Eberhardt, R. Mruk, P. Theato, R. Zentel, *Europ. Polym. J.* **2005**, *41*, 1569-1575.
- [21] TiO₂ nanoparticles which were functionalized in a similar manner have been shown by light scattering experiments to possess a hydrodynamic radius of approx. 80 nm, which is indicative of a partial agglomeration in solution and compatible with the slight agglomeration in the TEM image in Figure 6.2b.
- [22] Cerius2; 4.2ms ed.; *accelrys inc.*
- [23] P. G. Scherrer, *Nachr.* **1918**, *2*, 98.
- [24] M. N. Tahir, P. Théato, W. E. G. Müller, H. C. Schröder, A. Janshoff, J. Zhang, J. Huth, W. Tremel, *Chem. Comm.* **2004**, 2848-2849.

7. From Single Molecules to Nanoscopically Structured Functional Materials: Au Nanocrystal Growth on TiO₂ Nanowires Controlled by Surface Bound Silicatein

7.1. Introduction

The chemical construction of organized inorganic matter by using inorganic nanoparticles as building blocks offers a new and promising approach to functional materials with complex architectures and properties.^[1] The multiscale ordering, interlinking and interfacing of preformed nanoparticles may be directed by using artificially structured synthetic templates or through the programmed assembly based on self-encoding elements such as streptavidin-biotin^[2] and antibody-antigen complexes,^[3] complementary DNA strands^[4] or electrostatic self organization.^[5] Alternatively, artificial structuring can be achieved by using (meso)porous templates such as silica, synthetic opals,^[6] foams,^[7] emulsions^[8] or polymer sponges.^[9] The exploitation of these strategies remains a significant challenge as the properties and functions of materials are controlled not only by the nature of their building blocks, i.e. atoms, molecules and nanoparticles, but also through their organization to complex assemblies at various length scales.

Recently there has been much interest in the fabrication of ordered two- and three-dimensional devices by using nanotubes/wires as building blocks.^[10] Nanotubes/wires with various electronic and mechanical properties can be synthesized using a variety of methods, depending on the nature of constituent material. Nanotube/wire-nanoparticle hybrid materials, in which nanoparticles are attached to the walls of nanotubes/wires, may combine the unique structural and electronic properties of nanotubes/wires and the outstanding properties of nanoparticles which can tune their electronic structures via their size and morphology. In the past most efforts towards such hybrid materials focused on carbon nanotubes, prototype guest particles being Au^[11] or Pt^[11a,c] and semiconductors such as CdSe.^[12] This is surprising, as carbon nanotubes are very inert and therefore difficult to functionalize. Nanotubes/wires from compounds other than carbon e.g. TiO₂,^[13] V₂O₅,^[14] or WS₂^[15] can be expected to exhibit unique properties depending on the constituent compounds and their morphologies.. In

particular, oxidic nanotubes/wires would combine the versatile physical and chemical properties of ceramic materials and the tube/wire morphology.

A straightforward procedure to attach colloids onto the surface of nanotubes/wires is to grow the nanoparticles stabilized with capping ligands in solution and to anchor them to the outer tube/wire surface by chemical interactions in the final step.^[16] Whereas this synthetic approach has to rely on sophisticated stabilizing ligands to control nanoparticle size and binding to the surface.^[17] Biological systems are able to control nucleation processes highly precisely and reproducibly to produce an amazing diversity of nanostructured particle morphologies.^[18] Therefore it is a logical approach to use “biological surfaces”, e.g. biofunctionalized nanowires, as templates for the growth of nanoparticles on the wire surface. Biological methods using bacteria or proteins for the synthesis of metal^[19] and semiconductor^[20] nanoparticles still represent a relatively unexplored and underexploited alternative. The use of polypeptides or proteins seems advantageous because some bacteria and peptides have been shown to form and bind metal or semiconductor nanocrystals. Recently we reported the immobilization of silicatein, an enzyme involved in the biosilicification processes in marine sponges, onto self-assembled monolayers, and we demonstrated the catalytic activity of surface bound silicatein for the formation of SiO₂ from tetraethoxysilane (TEOS)^[21] and ZrO₂ from ZrF₆²⁻.^[22] In this communication, we report a facile procedure for the surface functionalization of TiO₂ nanowires by immobilization of His-tagged enzyme and the fabrication of Au nanoparticles onto the TiO₂ nanowires due to the bioreduction of HAuCl₄ mediated by the immobilized enzyme. The enzyme under consideration is versatile in its catalytic functions as reported by Morse^[23,24] and us.^[22] The methodology can be further extended to make core shell materials of metal and metal oxide. Surface functionalization was achieved using a polymeric ligand which can be used for the *in-situ- and post-functionalization* of TiO₂^[25] as well as for other metal oxides such as Fe₂O₃.^[26] The architecture of the polymeric ligand is of major importance, because it provides the basis of a comprehensive toolbox to construct supramolecular assemblies of organic-inorganic hybrid nanomaterials. Polymeric ligands offer an enhanced binding efficiency compared to low molecular weight ligands due to their multifunctional interaction with the surface, as demonstrated by Whitesides et al.^[27] The fact that active ester polymers react fast and quantitatively with amines to form the corresponding poly (acrylamides) opens the possibility to obtain multifunctional polymeric materials.^[28] Compared to the commonly used poly (N-

hydroxysuccinimide-acrylates) active ester polymers based on pentafluorophenylacrylates exhibit better solubility and higher reactivity, as we have already described elsewhere.^[28b]

The synthesis of the multifunctional polymeric ligand starting from this precursor polymer is illustrated in Figure 7.1. The active ester polymer was prepared by free radical polymerization yielding a polymer with molecular weight $M_n = 29.7$ kg/mol and $M_w = 58.5$ kg/mol (PDI = 1.96). This precursor -polymer was then transformed into the multifunctional polymeric ligand by substituting with amino-group containing functionalities.

The polymeric ligand was prepared by a stepwise substitution of the active ester groups:

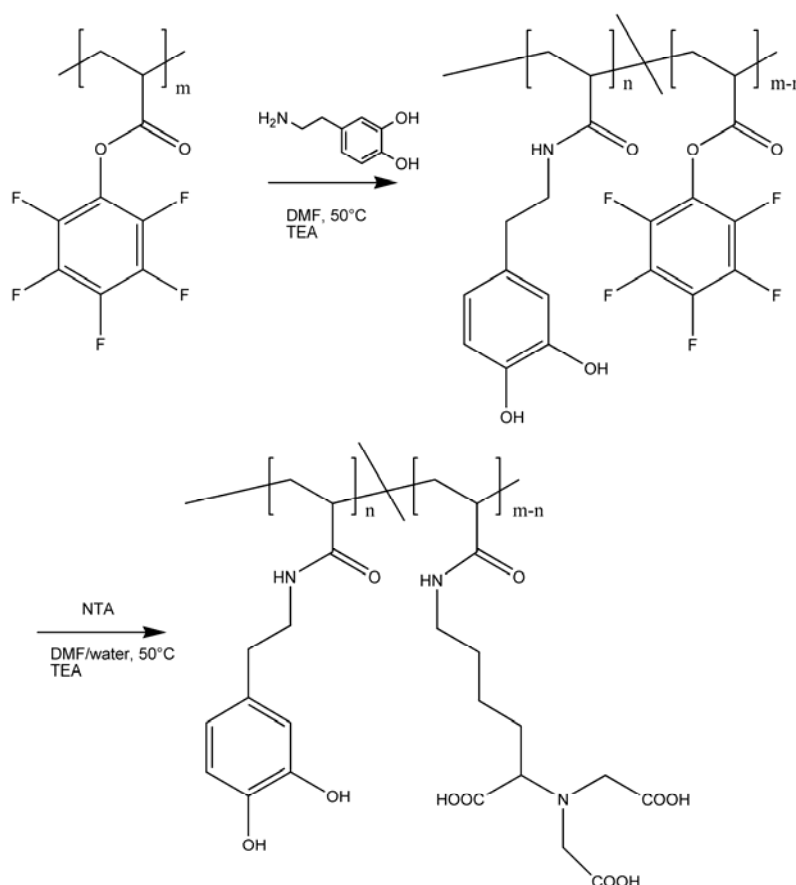


Figure 7.1. Synthesis of a multifunctional polymeric ligand containing nitrilotriacetic acid

firstly, by addition of 3-hydroxytyramine as anchor group for the attachment onto TiO_2 nanoparticles, secondly, amino-functionalized nitrilotriacetic acid (NTA) in water and triethylamine were added and the resulting mixture was kept at 50°C for 6 hours, finally, adjusting the pH of the solution to 2 with H_2SO_4 . The polymeric ligand was characterized by

$^1\text{H-NMR}$, GPC and FT-IR in order to determine its composition. Within the polymeric ligand the NTA contents were determined to 80 mol%, while 20 mol% of 3-hydroxytyramine were incorporated. The resulting polymer exhibits two different properties: (i) An NTA linker to immobilize His-tagged protein ^[29] (ii) 3-hydroxytyramine as anchor group for an attachment onto the TiO_2 nanoparticle surface.^[30]

Functionalization of TiO_2 nanowires was achieved by sealing a mixture of TiO_2 nanowires and 10 ml of polymeric ligand in benzyl alcohol under inert conditions and stirring at 60 °C for 4 hours. The product was repeatedly washed with CH_2Cl_2 to remove unreacted ligand. The functionalized TiO_2 nanowires were characterized by TEM, FT-IR¹H-NMR, and UV-vis spectroscopy.

7.2. Results and discussion

Functionalization of TiO_2 nanowires using polymeric ligand was characterized by FT-IR as shown in Figure 7.2.

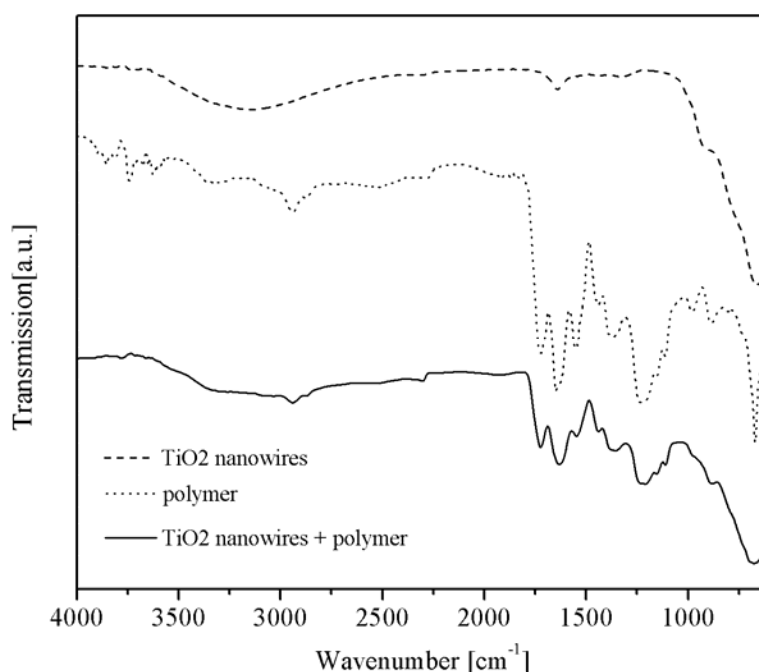


Figure 7.2. FT-IR spectra (a) TEM image of TiO_2 nanowires (dashed line), b) polymeric ligand (dotted dashed line) and c) TiO_2 nanowires functionalized with polymeric ligand (solid line).

Binding of silicatein to the surface of the TiO₂ nanowires functionalized with polymeric ligand incorporating NTA in the back bone of polymer was confirmed by confocal laser scanning microscopy (CLSM, Leica TCS SL with an argon laser) using fluorophore labelled antibodies against silicatein.^[31]

The fluorescence of the dye molecules was excited at 488 nm and detected from 504 - 514 nm using a 20-fold dry objective. An advantage of CLSM is that (i) detection of protein using fluorophore labelled antibodies is very specific, i.e. this antibody does not bind to any other component, and (ii) a large surface area can be seen. The scheme in Figure 7.3a illustrates the identification of surface bound silicatein.

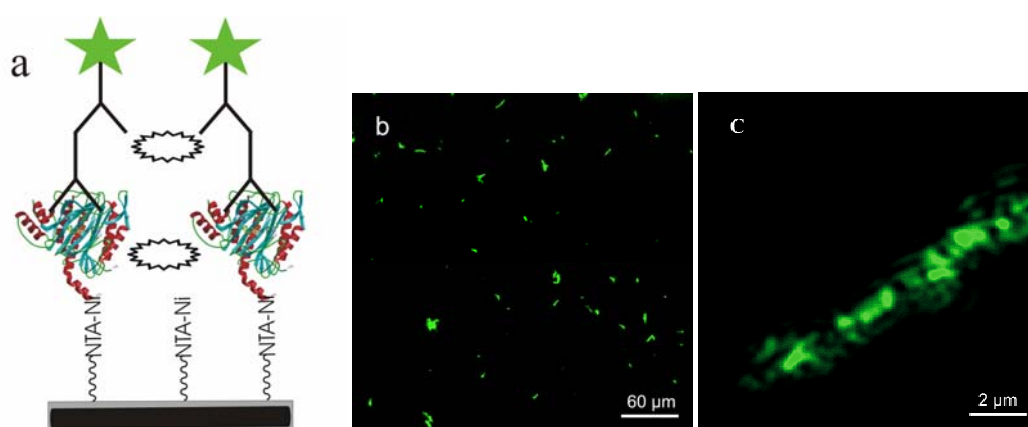


Figure 7.3. (a) Antigen capture assay. (A) TiO₂/silicatein complex (globular symbol = silicatein, oval dentate symbol = non-specific BSA (Bovine Serum Albumine), and Y symbol = specific monoclonal anti silicatein of *S. domuncula*). Assay visualized by recognition of antigen/antibody by fluorophore Cy2 coupled to antibodies detecting the mouse F_{AB}. Upon immobilization of fluorophore-labeled Ab (antibodies) onto the TiO₂/polymer/silicatein surface, the surface bound silicatein can be visualized by using Confocal laser scanning microscopy (CLSM). (b) Overview image showing many functionalized and immobilized silicatein TiO₂ nanowires. (c) HRCLSM image showing the presence of several adjacent fluorescence spots which indicates the binding of several silicatein molecules on a TiO₂ nanowire.

Figure 7.3(b and c) show the CLSM image of immobilized silicatein after exposing the surface to fluorophore labelled antibodies. Monoclonal antibodies raised against the silicatein immobilized onto the functionalized TiO₂ nanowires were used.^[31] The functionalized nanowires with immobilized silicatein were reacted with solutions containing mAb-aSilic; the

immunocomplexes were then stained with fluorophore-labeled (Cy2-label) secondary goat anti-rabbit antibodies. The surface bound silicatein strongly reacted with the antibodies as illustrated in Figure 7.3(b and c).

Due to the presence of Cy2, they appeared green and fluoresced at 520 nm. The high magnification image in Figure 7.3c (overview) indicates that several silicatein molecules are immobilized onto the backbone of functionalized TiO₂ nanowires. The high resolution CLSM (HR-CLSM) image in Figure 7.3c shows the morphology of silicatein which looks globular as already reported using AFM and CLSM.^[21,22,32]

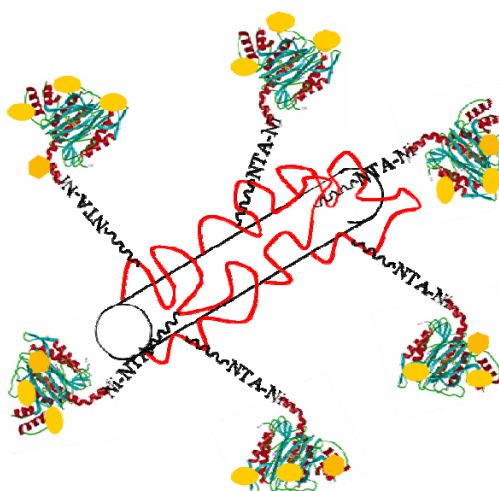


Figure 7.4. Schematic presentation of the TiO₂ nanowire/Au nanocrystals fabrication. In the first step the TiO₂ nanowire is functionalized with the multifunctional polymer ligand (red) by complexation through the catechol groups. The NTA tripod ligand is bound to the side groups of the polymer. In the next step silicatein containing HIS-tag is attached to the NTA ligand by Ni²⁺ complexation through the His-tag. Finally, tetrachloroauric acid is reduced by the sulfhydryl groups of immobilized silicatein. The Au nanocrystals are chemically bonded to the amino groups at the protein periphery.

It is difficult to comment on the actual size of the silicatein because it is beyond the resolution limits of CLSM. In our control experiment where functionalized TiO₂ nanowires were exposed to fluoro-labelled antibodies and no fluorescence was observed. The fabrication of the TiO₂ nanowires decorated with Au nanocrystals is illustrated in Figure 7.4. In the first step the TiO₂ nanowire is functionalized with the multifunctional polymer ligand (red) to the surface of the TiO₂ nanowire (white) by complexation through the hydroxyl groups of

dopamine thus tailoring the surface of TiO₂ nanowires with the NTA tripod ligand attached to the polymer. Secondly silicatein, containing the His-tag, was immobilized to the NTA ligand using Ni²⁺ complexation through the His-tag. Finally, tetrachloroauric acid is reduced by the surface bound silicatein. The growing Au nanocrystals are chemically bonded to the protein by complexation/surface binding. Upon addition of aqueous chloroauric acid to a solution of the silicatein functionalized TiO₂ nanowires, the color of the solution changed from pale yellow to red, which indicates the formation of gold nanoparticles by the reductive action of the protein. The UV-vis spectrum in Figure 7.5 recorded 3 hours after mixing the solutions at room temperature showed the appearance of a surface plasmon resonance band at about 570 nm and shifts to longer wavelengths with time (Figure 7.5).

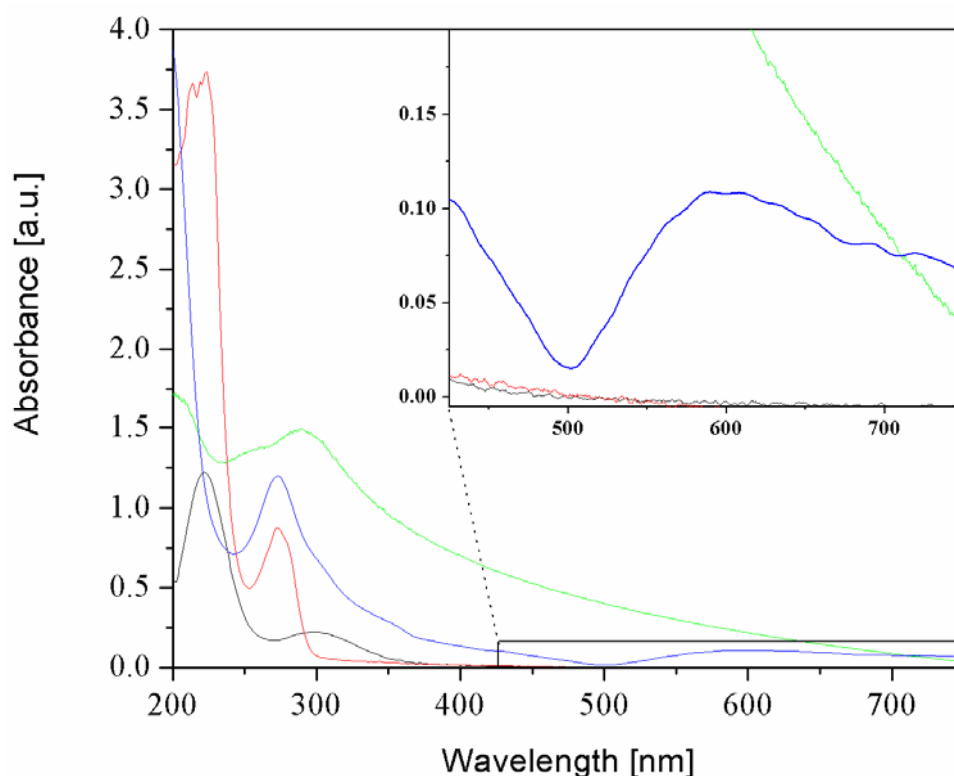


Figure 7.5. UV-vis absorption spectrum of a) synthesized TiO₂ nanowires (green line), b) polymeric ligand (red line), c) HAuCl₄ solution (black line) and d) polymer functionalized TiO₂ nanowires with immobilized silicatein and bio-reduced Au nanoparticles (blue line).

This shift is accompanied by an increase in the near-infrared (NIR) region of the electromagnetic spectrum. As a comparison, the UV-vis spectra of the synthesized TiO₂ nanowires (green line), the polymeric ligand (red line), and the HAuCl₄ solution (black line)

were measured. Clearly, the absorption at 275 nm of the polymeric ligand (red line) shows the presence of aromatic catechol groups and the absorption at 220 nm shows the presence of carbonyl groups. The blue shift of 15 nm in the absorption of the carbonyl groups (red line) indicates the His-tagged binding of the protein through Ni complexation by the NTA groups. A broad plasmon absorption band ranging from 520 – 700 nm for the composite (inset of Figure 7.5) indicates the aligned attachment of Au nanoparticles in the TiO₂/Au nanocomposites. The UV-vis absorption of the functionalized TiO₂ nanowires carrying no protein and AuCl₄⁻ did not show any plasmon absorption band which indicates that only polymer functionalized TiO₂ nanowires cannot reduce tetrachloroauric acid. In contrast, the polymeric ligand reduces AuCl₄⁻ in solution at the expense of the free hydroxyl groups of dopamine, whereas the surface bound polymeric ligand exhibits no reducing properties because all hydroxyl groups are involved in surface binding. Moreover, free silicatein can reduce AuCl₄⁻ efficiently to Au nanoparticles. These results indicate that Au reduction is restricted to protein functionalized TiO₂ nanowires only.

Our findings are compatible with the formation of anisotropic particles whose aspect ratio increases with time^[19c,19e] due to a uniaxial plasmon coupling or indicate the formation of spherical gold nanoparticles that aggregate with time (or a combination of both processes). Since recombinant silicatein does not contain any reducible saccharide groups, SH groups of cysteine or OH groups of tyrosine within the protein mantle must be considered to be involved in reduction of AuCl₄⁻ to Au⁰ and the subsequent growth of Au nanoparticles. As electron transfer can occur easily over distances of 20 Å and more,^[33] this reduction does not require the SH groups to be located at the periphery of protein. The amino groups arranged at the outer surface of silicatein may be assumed to act as coordinating centers for the surface binding of the gold colloids.

The HRSEM image of TiO₂ nanowires decorated with Au nanocrystals in Figure 7.6 (inset top left) shows that the TiO₂/Au hybrid is composed of hierarchically templated assemblies of Au nanoparticles and TiO₂ nanowires. The individual TiO₂/gold nanocomposites with a uniform TiO₂ backbone are clearly seen with a high aspect ratio in Figure 7.6. A high resolution view in the inset (bottom right) of Figure 7.6 reveals a triangular or hexagonal morphology of Au nanoparticles with a uniform statistical distribution across the TiO₂ nanowire.

The morphology of the TiO₂/Au composite was confirmed by TEM microscopy. Figure 7.7a shows an overview TEM image of the as synthesized TiO₂ nanowires. It reveals TiO₂

nanowires with diameters of 25-50 nm, wire lengths of up to a few micrometers. Figure 7.7b shows an overview image of several TiO₂ nanowires decorated homogeneously over their entire length with Au nanoparticles.

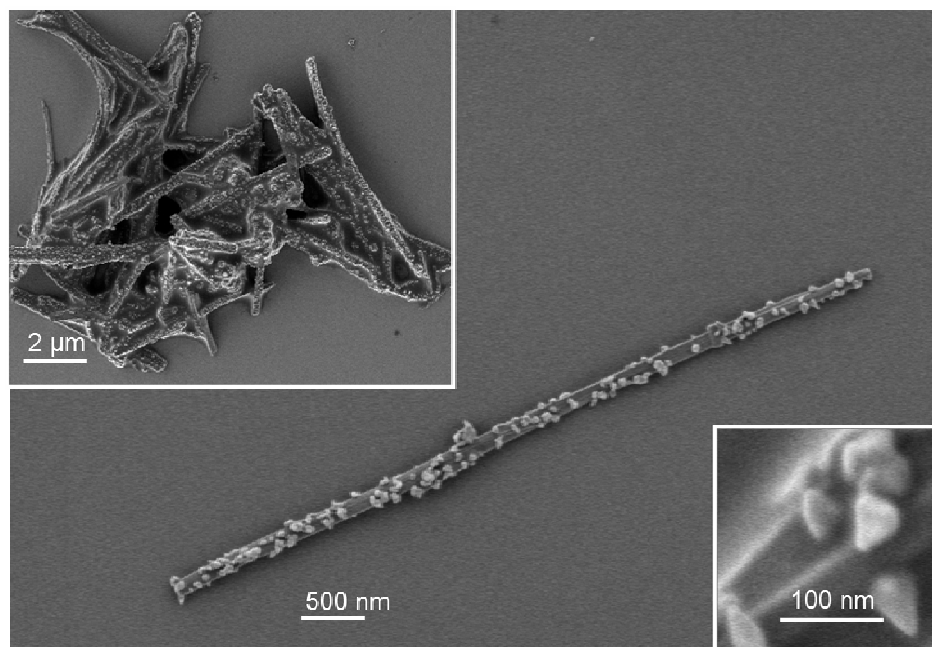


Figure 7.6. HR-SEM image demonstrating the hierarchical structure of the TiO₂ nanowire/Au nanoparticle composite. Overview images of the TiO₂/Au nanocomposites (top left) and a magnified view (right bottom) are given as insets.

The corresponding EDX spectrum is in Figure 7.7c clearly confirms the presence of Au, along with Ti and O. The TEM image of nanocrystals in Figure 7.7d, however, appears to be composed of triangular platelets inverted with respect to each other, i.e. in agreement with the results from the HRSEM image in Figure 7.6. Some of the nanocrystals grown in the presence of surface bound silicatein exhibit triangular morphology. The HRTEM image of one particle (Figure 7.7e) exhibits the view down $\langle 110 \rangle$ with clearly visible grain boundaries. A typical electron diffraction pattern of a 20 nm sized gold nanocrystal viewed along $\langle 110 \rangle$ zone is given in Figure 7.7f. This triangular crystal shape^[19e,34] is very unusual; except for one case^[19e] the limited number of examples reported so far have been obtained by chemical/photochemical methods. Shape control of inorganic materials in biological systems is achieved either by growth in constrained environments such as membrane vesicles,^[35] or through functional molecules such as polypeptides that bind specifically to inorganic surfaces.^[36] Specific polypeptide repeat sequences in proteins secreted by the bacterium *E.*

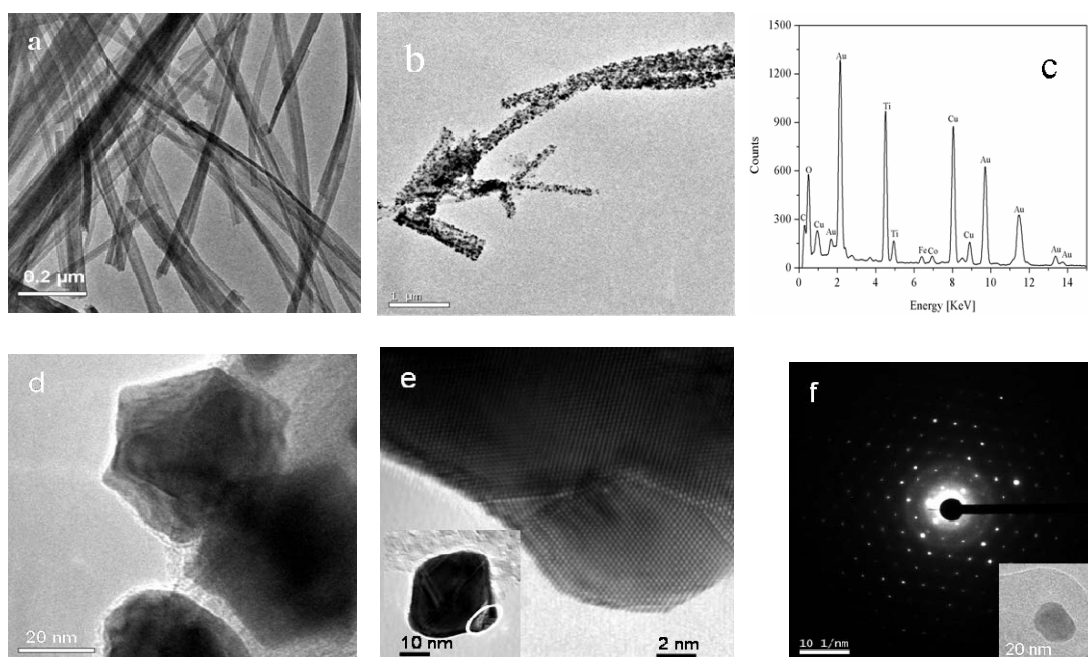


Figure 7.7. (a) TEM image of TiO₂ nanowires. (b) Overview image of TiO₂ nanowires decorated with Au nanocrystals, obtained by reduction with surface bound silicatein. (c) EDX spectrum of a TiO₂ nanowire decorated with Au nanocrystals, indicating the presence of Ti, O and Au. (d) Magnified view of a single TiO₂ nanowire with Au nanocrystals attached. (e) HRTEM of a crystal edge, (marked by a circle in the inset) showing the polycrystalline nature of the nanocrystal. (f) Nano-electron diffraction (NED) of an Au nanocrystal shown in the inset.

coli have been shown to induce growth of flat, triangular gold nanocrystals in low yield relative to the total nanoparticle formation.^[36]

Therefore, a possible explanation for the formation of surface bound nanotriangles is based on the chirality of the nucleation centers at the surface of the protein. Whereas hexagonal crystals are *achiral*, because they have an inversion center in the center of the Au hexagons, triangular crystals are *chiral*, because the inversion symmetry is lost during the formation of the triangular crystal. An S₃ axis of the hexagon is maintained as the high symmetry element, i.e. chiral information contained in the silicatein structure is transmitted to the nucleating gold nanocrystals during the AuCl₄⁻ → Au reduction and the subsequent Au nucleation at the outer surface of the protein and maintained during the nanocrystal growth.

This is compatible with the observation that triangular nanocrystals were also formed by reduction of AuCl_4^- in presence of lemon grass extract,^[19e] which presumably contains a multitude of yet unidentified proteins. In contrast, no triangular (or even pronounced) Au nanocrystal morphologies were observed when Au precursor compounds were reduced chemically and attached to histidin-rich peptides on the surface of carbon nanotubes.^[16,37] These findings suggest that the morphology of the Au nanocrystals is determined by the coordination and simultaneous reduction during nucleation process in the presence of the protein rather than by the chemical reduction in solution and subsequent binding to the polypeptide chain.

In summary, we have fabricated a functional nanocomposite by immobilized silicatein, a hydrolytic protein involved in the biomineralization of SiO_2 , on the surface of TiO_2 nanowires with the aid of a reactive polymeric ligand, which simultaneously serves as an anchor to the oxide surface and as a chelating ligand for the binding of the protein. The strategy of using such polymeric multifunctional ligands offers at least two advantages over the use of small (low-molecular weight) molecules as ligands: (i) Our polymeric ligand can be prepared by a two step synthesis, whereas a multistep synthesis is required for a low-molecular weight ligand which is compatible in function to our polymeric ligand.^[38] (ii) Polymeric ligands provide multidentate properties for binding, whose surface bonding is much stronger than that of monodentate low-molecular weight ligands.

7.3. Conclusion

The surface bound protein not only retains its original hydrolytic properties,^[21,22] but also acts as a reductant for AuCl_4^- in the synthesis of hybrid TiO_2/Au nanocomposites. The fabrication of hybrid materials using functional nano-biocomposites is without precedence. The advantage of applying biological and chiral “recognition” to the synthesis of metal nanoparticles on one-dimensional building blocks such as nanowires/nanotubes is not only the efficient and reproducible in nanoparticle production, it may be viewed also an environmentally friendly alternative to chemical methods for nanoparticle synthesis.

We believe that this procedure can be generalized for various metals and semiconductors and other nanotube/nanowire materials such as WS_2 . The biofunctionalization of the highly rigid oxide/chalcogenide wires/tubes also opens possibilities for the programmed assembly of

strictly one-dimensional building blocks based on self-encoding elements such as streptavidin-avidin and antibody-antigen complexes, complementary DNA strands or electrostatic self organization.

7.4. Experimental

The poly (active ester) poly (pentafluorophenylacrylate) **PFA** was prepared as reported earlier [28b]. GPC analysis of the obtained polymer (THF, light scattering detection) gave the following values: $M_n = 29.7$ kg/mol; $M_w = 58.5$ kg/mol, where the number of repeating units (246) is based on the M_w value.

For the synthesis of the multifunctional poly (acrylamides), poly (active ester) **PFA** (110 mg, 0.46 mmol repeating units) was dissolved in 3 ml dry DMF. A solution of 3-hydroxytyramine hydrochloride (10.5 mg, 0.055 mmol) in 1.5 ml DMF and 0.1ml triethylamine was added and the clear mixture stirred for 1 hour at 50°C. In the next step amino-functionalized **NTA** (120 mg, 0.46 mmol) in 0.9 ml MilliQ water and 2.1 ml triethylamine were added and the resulting mixture kept at 50°C for 6 hours. The slight excess of **NTA** was used to ensure complete conversion of the remaining active ester groups. After removal of the DMF the pH of the solution was adjusted to 3 and the crude viscous product was cleaned by dialysis in MilliQ water, isolated and finally dried in a vacuum oven at 40°C for 1 hour. 64 mg of a white polymeric powder were obtained. Recombinant silicatein was prepared as described. [39]

The TiO₂ nanowires were synthesized following a modified procedure given by Bruce and co-workers. [40] In brief, 1 g of Titanium isopropoxide (ACROS) was taken in a Teflon vessel and 6 ml of analytical grade Ethanol (99.8 %) were added into it. The Teflon vessel was kept in a desiccator. The precipitation of TiO₂ was initiated under moist atmosphere induced by placing a Petri dish filled with water at the bottom of the desiccator. The diffusion experiment was stopped after 12 hours, followed by the addition of 25 ml of 10 M NaOH aqueous solution. Then the reaction vessel was sealed into a stainless steel hydrothermal bomb, which was placed in an oven maintained at 180 °C for 20 hours. The obtained sample was filtered and repeatedly washed with 0.1 M HNO₃, 1 N HCl and de-ionized water. The product was dried under vacuum for 3 hours.

Then 5 mg of TiO₂ nanowires were dispersed in 10 ml of benzyl alcohol and sonicated for 15 minutes. In a separate vial were dissolved 10 mg of polymer ligand in 10 ml of benzyl alcohol. Both suspension and solution were mixed under inert conditions and stirred at 60°C for four hours. Then polymer functionalized nanowires were isolated and purified by repeated washing with CH₂Cl₂ using centrifugation, followed by drying under vacuum and dispersing under water.

To immobilize the silicatein, Ni^{2+} was bound to NTA group, the TiO_2 nanowires functionalized with polymeric ligand containing NTA in the backbone were treated with 1 mmol NaOH for 10 minutes using continuous stirring which were then centrifuged, washed with 18.2 MilliQ water, and followed by rotating the TiO_2 nanowires in a solution of NiSO_4 (40 mmol) for 1 hour. Then TiO_2 nanowires containing complexed Ni^{2+} were taken out washed with (150 mmol) solution of NaCl and deionized water and dried in a stream of N_2 . Then silicatein solution (30 nmol) in 3-(N-morpholino) propane sulfonic acid (MOPS) buffer was introduced to the Ni^{2+} bound TiO_2 nanowires for 1 hour. Then silicatein immobilized TiO_2 nanowires were washed with MOPS buffer and deionized water to get rid of unbound protein.. The immobilization of silicatein was monitored by CLSM. To check the specific immobilization or activity of enzyme, silicatein immobilized TiO_2 nanowires in water were added to 1 ml of aqueous solution of HAuCl_4 (10^{-3} M) in 2 ml of polyethylene vial. The suspension of silicatein coated TiO_2 nanowires and gold acid solution was immediately placed on rotator (biocentrifuge). The protein immobilized TiO_2 precursor suspension was mixed on the rotator at a speed of 1000 rpm for 24 hours under normal conditions. The “bioreduction” of tetrachloroauric acid was monitored by UV-visible spectroscopy. Following this reaction period; the biomass was centrifuged at 3000 rpm for 10 min and repeatedly washed with sterile distilled water before doing all subsequent characterization.

7.5. References

- [1] S. Mann, S. A. Davis, S. R. Hall, M. Li, K. H. Rhodes, W. Shenton, S. Vaucher, B. Zhang, *Dalton's Trans.* **2000**, 3753-3753.
- [2] (a) S. Connolly, D. Fitzmaurice, *Adv. Mater.* **1999**, *11*, 1202-1205.
- [3] W. Shenton, S. A. Davis, S. Mann, *Adv. Mater.* **1999**, *11*, 449-452.
- [4] (a) C. A. Mirkin, R. L. Lesinger, R. C. Mucic, J. J. Storhoff, *Nature* **1996**, *382*, 607-609. (b) P. Alivisatos, K. P. Johnsson, X. Peng, T. E. Wilson, C. J. Loweth, M. Bruchez, P. G. Schultz, *Nature* **1996**, *382*, 609-612. (c) E. Dujardin, L. B. Hsin, C. R. C. Wang, S. Mann, *Chem. Comm.* **2001**, 1264-1265. (d) A. N. Shipway, I. Willner, *Chem. Comm.* **2001**, 2035-2045.
- [5] A. K. Boal, T. H. Galow, F. Alhan, V. M. Rotello, *Adv. Funct. Mater.* **2001**, *11*, 461-465.
- [6] (a) Y. A. Vlasov, N. Yao, D. J. Morris, *Adv. Mater.* **1999**, *11*, 165-169. (b) B. T. Holland, C. F. Blanford, T. Do, A. Stein, *Chem. Mater.* **1999**, *11*, 795-805 (c) G. Subramania, V. N. Manoharan, J. D. Thorne, D. J. Pine, *Adv. Mater.* **1999**, *11*, 1261-1265 (d) F. Fleischhaker, A. C. Arsenault, Z. Wang, V. Kitaev, F. C. Peiris, G. von Freymann, I. Manners, R. Zentel, G. Ozin, *Adv. Mater.* **2005**, *17*, 2455-2458.
- [7] (a) F. Carn, F. A. Colin, M. F. Achrad, H. Deleuze, Z. Saadi, R. Backov, *Adv. Mater.* **2004**, *16*, 140. (b) S. Mandal, S. K. Arumugam, S. D. Adyanthaya, R. Pasricha, M. Sastry, *J. Mater. Chem.* **2004**, *14*, 43-47.
- [8] B. zu Pultitz, K. Landfester, H. Fischer, M. Antonietti, *Adv. Mater.* **2001**, *13*, 500-503.
- [9] M. Breulmann, S. A. Davis, S. Mann, H. P. Hentze, M. Antonietti, *Adv. Mater.* **2000**, *12*, 502-507.
- [10] (a) M. R. Diehl, S. N. Yaliraki, R. A. Beckman, M. Barahona, J. R. Heath, *Angew. Chem. Int. Ed.* **2002**, *41*, 353-356. (b) A. Bachthold, P. Hadley, T. Nakanishi, C. Decker, *Science* **2001**, *294*, 1317-1320. (c) Y. Cui, Q. Q. Wie, H. K. Park, C. M. Lieber, *Science* **2001**, *293*, 1289-1292. (d) W. U. Huynh, J. J. Dittmer, A. P. Alivisatos, *Science* **2002**, *295*, 2425-2427. (e) P. G. Collins, M. S. Arnold, P. Avouris, *Science* **2001**, *292*, 706-708.
- [11] (a) B. C. Satishkumar, M. G. Chapline, E. M. Vogl, A. Govindaraj, C. N. R. Rao, *J. Appl. Phys D: Appl. Phys.* **1996**, *29*, 3173-3176. (b) S. Fullam, D. Cottell, H. Rensmo,

- D. Fitzmaurice, *Adv. Mater.* **2000**, *12*, 1430-1432. (c) H. Shoi, M. Shim, S. Bangsaruntip, H. Dai, *J. Am. Chem. Soc.* **2002**, *124*, 9058. (d) K. Jiang, A. Eitan, L. S. Schadler, P. M. Ajayan, R. W. Siegel, N. Grobert, M. Mayne, M. Reyes, H. Terrones, M. Terrones, *Nano Lett.* **2003**, *3*, 275-278. (e) A. V. Ellis, K. Vijayamohanan, R. Goswami, N. Chakrapani, L. S. Ramanathan, P. M. Ajayan, G. Ramanath, *Nano Lett.* **2003**, *3*, 279-282.
- [12] (a) S. Banerjee, S. S. Wong, *Nano Lett.* **2002**, *2*, 195-199. (b) J. M. Haremza, M. A. Hahn, T. D. Krauss, S. Chen, J. Calcines, *Nano Lett.* **2002**, *2*, 1253-1256.
- [13] G. Armstrong, A. R. Armstrong, J. Canales, P. G. Bruce, *Chem Comm.* **2005**, 2454-2456.
- [14] (a) M. E. Spahr, P. Bitterli, R. Nesper, M. Müller, F. Krumeich, H. U. Nissen, *Angew. Chem. Int. Ed. Engl.* **1998**, *37*, 1263-1266. (b) F. Krumeich, H. J. Muhr, M. Niederberger, F. Bieri, B. Schnyder, R. Nesper, *J. Am. Chem. Soc.* **1999**, *121*, 8324-8331.
- [15] a) A. Rothschild, G. L. Frey, M. Homyonfer, R. Tenne, M. Rappaport, *Mat. Res. Innovat.* **1999**, *3*, 145-149. b) A. Rothschild, J. Sloan, R. Tenne, *J. Am. Chem Soc.* **2000**, *122*, 5169-5179. c) H. A. Therese, J. Li, U. Kolb, W. Tremel, *Solid State Sci.* **2005**, *7*, 67-72.
- [16] H. Matsui, S. Pan, G. E. Douberly, Jr., *J. Phys. Chem. B* **2001**, *105*, 1683-1686.
- [17] O. Masala, R. Seshadri, *Ann. Rev. Mater. Res.* **2004**, *34*, 41-81.
- [18] (a) S. Mann, *Biomineralization*, Oxford University Press, New York, **2001**. (b) E. Bäuerlein, *Biomineralization*; Wiley-VCH, Cambridge, **2004**.
- [19] (a) M. Field, C. J. Smith, D. D. Awschalom, N. H. Mendelson, E. L. Mayes, S. A. Davis, D. Mann, *Appl. Phys. Lett.* **1998**, *73*, 1739-1741. (b) T. Klaus, R. Joerger, E. Olsson, C. G. Granqvist, *Proc. Natl. Acad. Sci.* **1999**, *96*, 13611-13614. (c) E. Dujardin, L. B. Hsin, C. R. C. Wang, S. Mann, *Chem. Comm.* **2001**, 1264-1265. (d) R. R. Naik, S. J. Stringer, G. Agarwal, S. E. Jones, M. O. Stone, *Nature Mater.* **2002**, *1*, 169-172. (e) S. S. Shankari, A. Rai, B. Ankamwar, A. Singh, A. Ahmad, M. Sastry, *Nature Mater.* **2004**, *3*, 482-488. (f) S. Senapati, A. Ahmad, M. I. Khan, M. Sastry, R. Kumar, *Small* **2005**, *1*, 517-520.
- [20] (a) W. Shenton, T. Douglas, M. Young, G. Stubbs, S. Mann, *Adv. Mater.* **1999**, *11*, 253-256. (b) J. D. Hartgering, E. Beniash, S. I. Stupp, *Science* **2001**, *294*, 1684-1688. (c) S. W. Lee, C. Mao, C. E. Flynn, A. M. Belcher, *Science* **2002**, *296*, 892-895.

- (d) C. Mao, D. J. Solis, B. D. Reiss, S. T. Kottmann, R. Y. Sweeney, A. Hayhurst, G. Georgiou, B. Iverson, A. M. Belcher, *Science* **2004**, *303*, 213-217. (e) D. Rautaray, A. Ahmad, M. Sastry, *J. Mater. Chem.* **2004**, *14*, 2333-2340. (f) V. Bansal, D. Rautaray, A. Ahmad, M. Sastry, *J. Mater. Chem.* **2004**, *14*, 3303-3305.
- [21] M. N. Tahir, P. Théato, W. E. G. Müller, H. C. Schröder, A. Janshoff, J. Zhang, J. Huth, W. Tremel, *Chem. Comm.* **2004**, 2848-2849.
- [22] M. N. Tahir, P. Théato, W. E. G. Müller, H. C. Schröder, A. Borejko, S. Faiß, A. Janshoff, J. Huth, W. Tremel, *Chem. Comm.* **2005**, 5533-5535.
- [23] (a) K. Shimizu, J. N. Cha, G. D. Stucky, D. E. Morse, *Proc. Natl. Acad. Sci. USA* **1998**, *95*, 6234-6238. (b) J. N. Cha, K. Shimizu, Y. Zhou, S. C. Christiansen, B. F. Chmelka, G. D. Stucky, D. E. Morse, *Proc. Natl. Acad. Sci. USA* **1999**, *96*, 361-365.
- [24] J. N. Cha, K. Shimizu, Y. Zhou, S. C. Christiansen, B. F. Chmelka, G. D. Stucky, J. H. Choi, J. C. Weaver, W. Yang, D. E. Morse, *Adv. Mater.* **2005**, *17*, 314-318.
- [25] M. Niederberger, G. Garnweitner, F. Krumeich, R. Nesper, H. Cölfen, M. Antonietti, *Chem. Mater.* **2004**, *16*, 1202-1208. (b) N. M. Dimitrijevic, Z. V. Saponjic, B. M. Rabatic, T. Rajh, *J. Am. Chem. Soc.* **2005**, *127*, 1344-1345.
- [26] M. N. Tahir, M. Eberhardt, P. Theato, S. Faiß, A. Janshoff, T. Gorelik, U. Kolb, W. Tremel, *Angew. Chem.* **2005**, *118*, 922-926. *Angew. Chem. Int. Ed.* **2006**, *45*, 908-912.
- [27] (a) J. L. Dalsin, L. Lin, S. Tosatti, J. Vörös, M. Textor, P. B. Messersmith, *Langmuir* **2005**, *21*, 640-646. (b) M. Mammen, S. H. Gu, Z. Yang, J. Gao, C. K. Choi, G. M. Whitesides, *Angew. Chem.* **1998**, *110*, 2908-2953. *Angew. Chem. Int. Ed.* **1998**, *37*, 2754-2794.
- [28] (a) I. Potavova, R. Mruk, S. Prehl, R. Zentel, T. Basche, A. Mews, *J. Am. Chem. Soc.* **2003**, *125*, 320-321. (b) M. Eberhardt, R. Mruk, P. Theato, R. Zentel, *Europ. Polym. J.* **2005**, *41*, 1569-1575.
- [29] (a) G. B. Sigal, C. Bamdad, A. Barberis, J. Strominger, G. M. Whitesides, *Anal. Chem.*, **1996**, *68*, 490-497. (b) I. T. Dorn, K. R. Neumaier, R. Tampe, *J. Am. Chem. Soc.* **1998**, *120*, 2753-2763.
- [30] N. M. Dimitrijevic, Z. V. Saponjic, B. M. Rabatic, T. Rajh, *J. Am. Chem. Soc.* **2005**, *127*, 1344-1347.

- [31] W. E. G. Müller, M. Rothenberger, A. Borejko, W. Tremel, A. Reiber, H. C. Schröder, *Cell Tissue Res.* **2005**, *321*, 285-297.
- [32] A. Pisera, *Microsc. Res. Technique* **2003**, *62*, 312-326.
- [33] Electron Transfer in Biology and the Solid State, M. K. Johnson, R. B. King, D. M. Kurtz, C. Kotal, M. L. Norton, R. A. Scott (Eds.), *Adv. Chem. Ser.* 226, American Chemical Society, Washington **1990**.
- [34] (a) A. Ahmad, S. Senapati, M. I. Khan, R. Kumar, M. Sastry, *Langmuir* **2003**, *19*, 3550-3553. (b) Y. Sun, Y. Xia, *Science* **2002**, *298*, 2176-2179. (c) Y. Sun, B. Mayers, Y. Xia, *Nano Lett.* **2003**, *3*, 675-679. (d) S. Chen, D. L. Carroll, *Nano Lett.* **2002**, *2*, 1003-1007. (e) R. Jin, Y. W. Cao, C. A. Mirkin, K. L. Kelly, G. C. Schatz, J. G. Zheng, *Science* **2001**, *294*, 1901-1903. (f) R. Jin, Y. C. Cao, E. Hao, G. S. Metraux, G. C. Schatz, C. A. Mirkin, *Nature* **2003**, *425*, 487-490.
- [35] N. Kröger, R. Deutzmann, M. Sumper, *Science* **1999**, *286*, 1129-1132.
- [36] S. Brown, M. Sarikaya, E. A. Johnson, *J. Mol. Biol.* **2000**, *299*, 725-735.
- [37] R. Djalali, Y. F. Chen, H. Matsui, *J. Am. Chem. Soc.* **2002**, *124*, 13660-13661.
- [38] H. W. Gu, P. L. Ho, K. W. Tsang, L. Wang, B. Xu, *J. Am. Chem. Soc.* **2003**, *125*, 15702-15703.
- [39] W. E. G. Müller, A. Krasko, G. L. Pennec, R. Steffen, M. S. A. Ammar, M. Wiens, I. M. Müller, H. C. Schröder, *Progr. Mol. Subcell Biol.* **2003**, *33*, 195-222.
- [40] A. R. Armstrong, G. Armstrong, J. Canales, P. G. Bruce, *Angew. Chem* **2004**, *116*, 336-2338. *Angew. Chem. Int. Ed.* **2004**, *43*, 2286-2288.

8. Overcoming the Insolubility of Molybdenum Disulfide Nanoparticles Through a High Degree of Sidewall Functionalization Using Polymeric Chelating Ligands

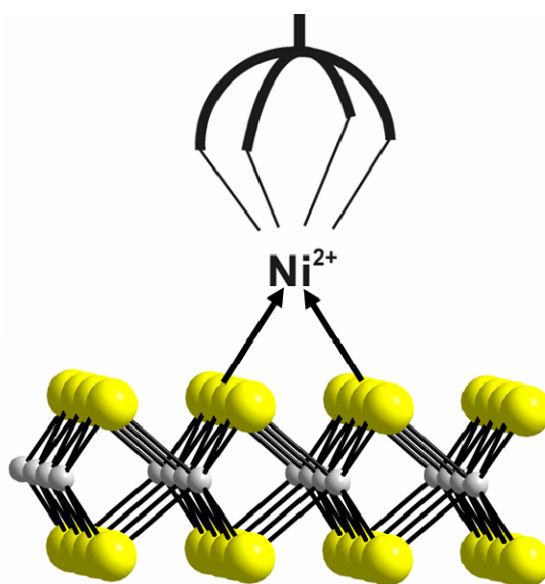
8.1. Introduction

The covalent attachment of functional ligands such as photo- or redox active molecular compounds to inorganic nanoparticle surfaces is an important first step in the design of new materials. These applications, however, usually require designated molecules to be immobilized on the nanoparticle. A wide variety of molecular surface chemical linkages have been devised for oxide surfaces based on siloxane,^[1] carboxylic acid,^[2] acetyl acetate,^[3] phosphonate^[4] or catecholate functional groups.^[5] Carbon nanotubes, which are chemically inert, can be surface activated by oxidative treatment with anchor groups such as hydroxyl (-OH), carboxyl (-COOH), or carbonyl (>C=O)^[6] that are necessary to tether metal ions to the tube. Besides metal oxides and carbon nanotubes^[7] metal chalcogenide nanoparticles^[8] and nanotubes,^[9] firstly reported by Tenne and co-workers in 1992, have opened up an exciting new area of research into nanomaterials with sheet structures, which – unlike single layer graphite – are multiple layer structures. These MQ₂ (Q = S, Se, Te) species, termed inorganic fullerenes (IF) and inorganic nanotubes, are akin to carbon nanotubes in that they exhibit analogous mechanical^[10] and electronic^[11] properties. Their excellent lubrication properties^[12] are related to their crystal structures which are characterized by weak van der Waals forces between the individual MQ₂ slabs containing metal atoms sandwiched between two inert chalcogen layers. It is the inertness of the chalcogen surface layer and the associated shielding of the molybdenum atoms from nucleophilic attacks by organic ligands which are the main obstacles for the functionalization of MoS₂ nanoparticles.

In principle, a functional surface ligand consists of an anchor group that attaches to the nanocrystal, functionality, and a spacer in between. The purpose of the functionality is to render the particles soluble or to provide the proper reactivity when the IFs are used as chemical agents, e.g. to disperse them in polymers or in oils. For example, aliphatic chains provide solubility of the particles in non-polar solvents,^[13] while deprotonated carboxylic functions will lead to charged particles that are soluble in water.^[14] Some strategies employed for carbon nanotubes, but unsuccessful for metal chalcogenides, are polymer wrapping^[15] or

coating with surfactants.^[16] A functionalization of chalcogenide nanoparticles and nanotubes can serve not only to improve their solubility, and therefore, dispersion, but also to create attractive van der Waals interactions between a nanotube and a polymer addend or transfer the properties of functional ligands to the chalcogenide nanoparticle.

While thiolated organic molecules serve as excellent anchors to link the functional molecules on metallic nanoparticles such as Au, Pt or Co,^[17,18] amines and/or thiols are prototype organic anchor groups for inorganic semiconductors such as CdSe, ZnS or ZnO, which have reasonable affinities to nanoparticle surfaces with vacant metal cation M^{2+} sites.^[18] Catechol-type chelating ligands^[18,19] (e.g. dopamine), on the other hand, are robust anchor groups for most early transition metal oxide particles such as TiO_2 ,^[20] ZrO_2 ,^[21] Al_2O_3 ,^[22] Cr_2O_3 ,^[23] or Fe_2O_3 ,^[24] where the catechol group preferentially binds to the edges of the oxide nanocrystals which have a higher surface energy. These general principles of coordination chemistry are not new and have been used extensively for many years in the classic scheme of qualitative inorganic analysis with organic dyes.^[18,19]



1

The sandwich-type structure of the metal dichalcogenide particles, however, requires a different strategy. As the established strategies proved unsuccessful to generate individually functionalized chalcogenide nanoparticles or nanotubes, we have employed functional surface ligands which can serve as linkers between the nanoparticles and an appropriate “metal docking site”.

We report a facile method for the functionalization of IF-MoS₂ nanoparticles that employs nitrilotriacetic acid (NTA)^[25] as a robust anchor to immobilize functional molecules on the outer sulfur layer. Since a direct anchoring of organic ligands to the sulfur surface is not possible, a transition metal cation with a high sulfur affinity and octahedral coordination is used, whose coordination sphere is blocked completely on one side with an umbrella-type chelating ligand,^[26] whereas the other part of the coordination sphere remains open for docking to the sulfur layer (**1**). Recently we have used a modified tetradentate NTA ligand for the immobilization of proteins to self-assembled monolayers,^[27] where the two vacant coordination sites of the transition metal (Ni²⁺) ion are used for binding to the “histidine-tag” of the protein, whereas they are binding to the sulfur layer of the IF-MoS₂ in the present case. The resulting functionalized IF-MoS₂ particles can be dispersed in water and organic solvents and they were characterized by high-resolution transmission electron microscopy (HRTEM), FT-IR, TGA, UV-vis, and confocal laser scanning microscopy (CLSM). The IF-MoS₂ particles were prepared as described previously by a MOCVD method.^[28]

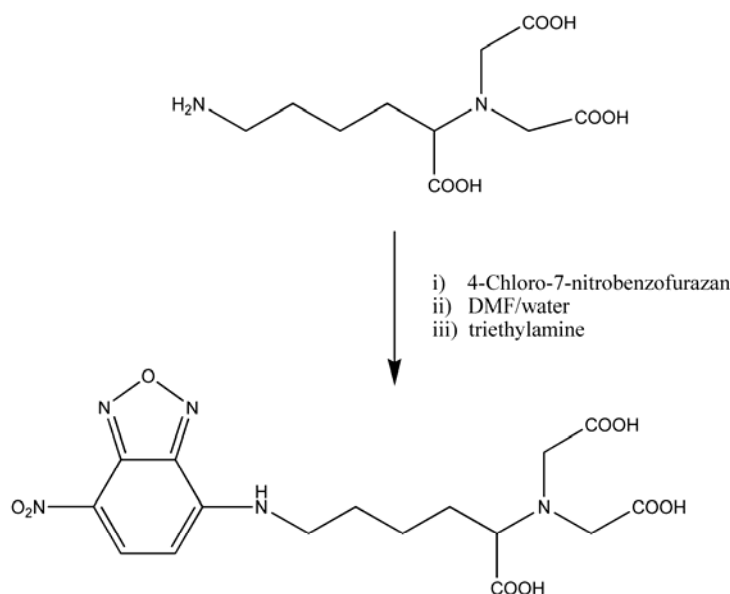


Figure 8.1. NTA ligand functionalized with a fluorescent 7-nitrobenzofurazan

Surface functionalization was achieved (i) using a NTA ligand functionalized with a fluorescent 7-nitrobenzofurazan unit (Figure 8.1) and (ii) using a polymeric ligand carrying an NTA group and a catechol type of ligand, which has been used as anchor groups for the functionalization of metal oxides.^[20]

The architecture of the polymeric ligand is of special importance, because it provides the basis of a toolbox to construct supramolecular assemblies of organic-inorganic hybrid nanomaterials.

The multifunctional polymers that are necessary to realize such systems can be prepared by a flexible synthetic route starting from reactive precursor polymers. As such reactive precursor polymers active ester polyacrylates can be used. The fact that active ester polymers react fast and quantitatively with amines to form the corresponding poly (acrylamides) opens the possibility to obtain multifunctional polymeric materials.^[29] Compared to the commonly used poly (N-hydroxysuccinimide-acrylates) active ester polymers based on pentafluorophenylacrylates exhibit better solubility and higher reactivity, as described by Theato et al. recently,^[29b] thus opening the possibility to work under mild conditions.

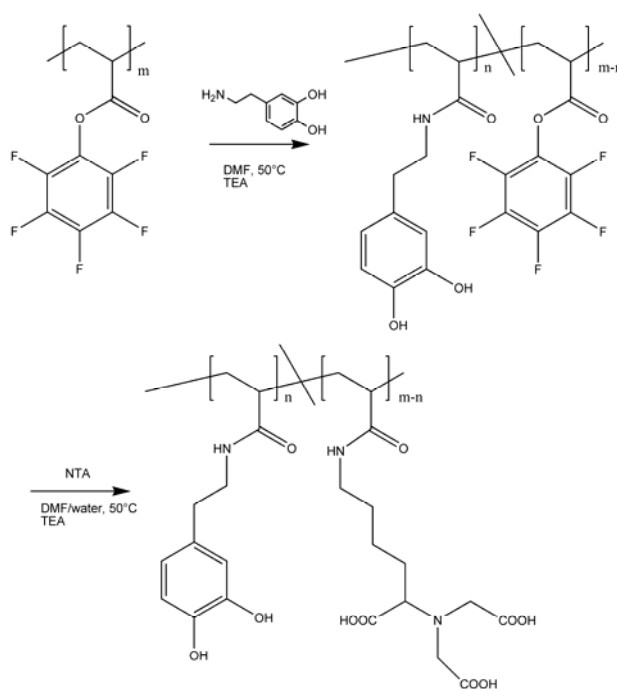


Figure 8.2. Synthesis of the block copolymer with catechol-type side groups for metal oxide binding and umbrella-type nitrilotriacetic acid ligands blocking on side of the coordination sphere of metals bonded to the S atoms of the MoS₂ surface layer, thereby preventing a precipitation of MoS₂ nanoparticles due to cross-linking.

Free radical polymerization of pentafluorophenylacrylate yielded the polymeric active ester poly(pentafluorophenylacrylate) **PFA** with a molecular weight $M_n = 29.7$ kg/mol and $M_w = 58.5$ kg/mol (PDI = 1.96). This pre-polymer was then transformed into the multifunctional polymeric ligand by substitution with amino functionalized molecules as outlined in Figure 8.2. In a first step 3-hydroxytyramine as anchor group for the attachment onto TiO_2 nanowires was covalently bound to the polymer backbone, secondly, amino-functionalized nitrilotriacetic acid (**NTA**) was introduced. All polymer analogous reactions were carried out in a mixture of water, DMF and triethylamine at 50°C .

8.2. Results and discussion

The resulting polymer exhibits two different properties: (i) An NTA linker which can be used to coordinate to Ni^{2+} cations which, in turn, can use their vacant coordination sites for binding to the surface S atoms of IF-MoS₂ nanoparticles, (ii) 3-hydroxytyramine as anchor group for an attachment onto the surface of metal oxides. The obtained multifunctional polymer has been analyzed by ¹H-NMR, FT-IR and GPC in order to determine its composition. Within the polymeric ligand the NTA content was determined to be 80 mol%, while 20 mol% of 3-hydroxytyramine were incorporated.

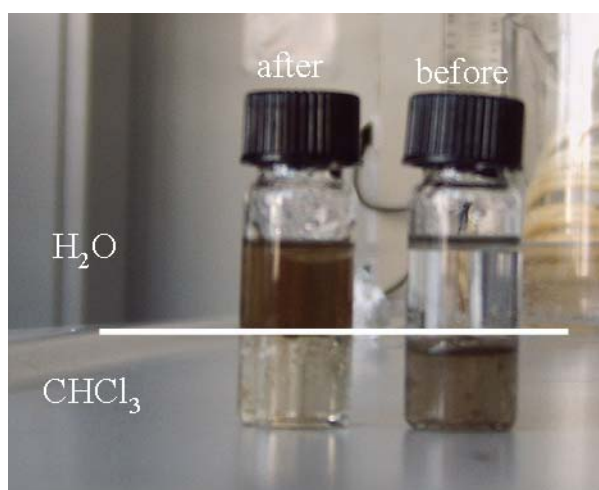


Figure 8.3. Photograph of a solutions/dispersions of IF-MoS₂ before (right) and after (left) surface functionalization in water (top layer) and in CHCl_3 (bottom layer).

A first indication concerning the surface functionalization of IF-MoS₂ is based on the solubility of the functionalized IF-MoS₂ nanoparticles in water and chloroform. Because of its hydrophobicity, IF-MoS₂ is completely insoluble in water, whereas it can be dispersed in nonpolar solvents like chloroform. After surface functionalization using polymeric ligand containing NTA/Ni²⁺ (for surface binding) and polar (hydroxal, carbonyl) groups, IF-MoS₂ can be transferred from apolar chloroform to the polar aqueous phase as shown in Figure 8.3. The dark-brown color of the solution arises from the ligand-to-metal charge-transfer interaction of IF-MoS₂ and between the ligand and surface bound metal Ni²⁺ ions as well. The solubility properties of the functionalized IF-MoS₂ nanoparticles are mainly determined by the functional groups of the surface ligand. Figure 8.4a shows the HRTEM image of a large functionalized MoS₂ particle with a diameter of approx. 70 nm. The EDX spectrum of the circled area marked in Figure 8.4b shows the presence of a significant nickel content validating the surface binding of NTA. Further evidence of the sidewall functionalization was obtained by IR spectroscopy (Figure 8.5(a and b)) for polymer functionalized IF-MoS₂ (Figure 8.5a) and IF-MoS₂ nanoparticles carrying NTA ligands only (Figure 8.5b).

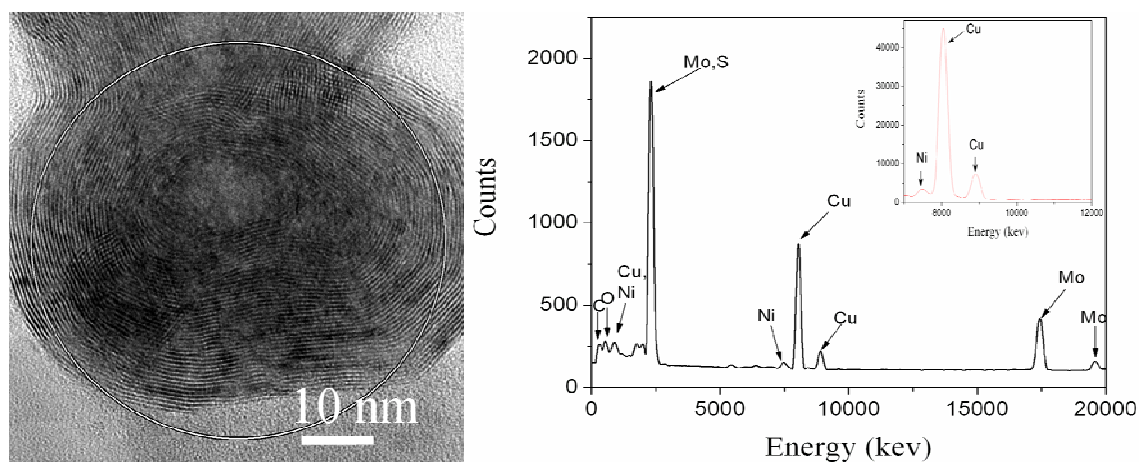


Figure 8.4. (a) HRTEM image of a surface functionalized IF-MoS₂ particle. (b) EDX spectrum of the area marked by a circle in (a).

The most prominent bands in the 3500-3300 cm⁻¹ region arise from NH₂ stretching vibrations of the NTA ligand, the bands at 2920 (2917) and 2850 (2852) cm⁻¹ can be assigned to the stretching vibrations of the CH₂ groups, the absorption band at 1750 cm⁻¹ to the C=O stretches of the tricarboxylate anchor group and the adsorption band at 1600 cm⁻¹ to the aromatic ring of the 3-hydroxytyramine.

The UV-vis spectrum of the functionalized MoS₂ particles (with catechol side groups attached to the polymer backbone) in water (Figure 8.5c) shows the characteristic broad absorption band of IF-MoS₂ at about 495 nm.

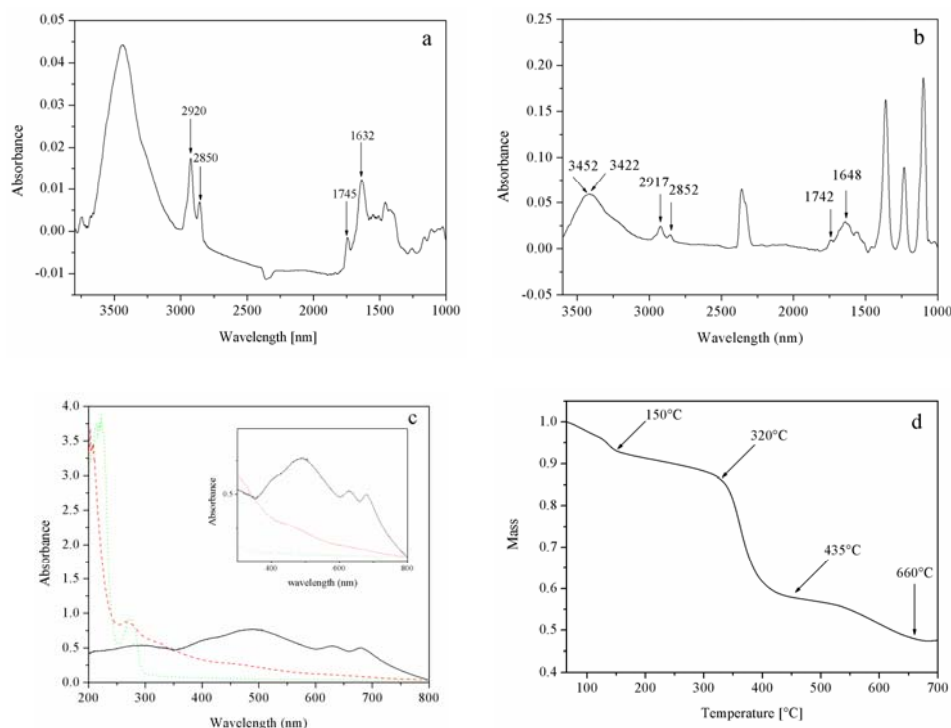


Figure 8.5. (a) FT-IR spectrum of polymer functionalized IF-MoS₂ nanoparticles. (b) FT-IR spectrum of NTA functionalized IF-MoS₂ nanoparticles. (c) UV-Vis absorption spectrum of a IF-MoS₂ dispersion (solid line), the polymer (dotted line) and the functionalized IF-MoS₂ nanoparticles (dashed line). (d) Determination of the

The band at 280 nm for the naked polymer arises from the catechol side chains, while the strong absorption at 225 nm can be assigned to the C=O groups of the NTA moieties. The 490 nm band of IF-MoS₂ is still visible as a shoulder in the MoS₂ composite (inset in Figure 3c); the pronounced blue-shift of the C=O absorption from 225 nm to 205 nm in the IF-MoS₂/polymer composite indicates the surface binding of the NTA groups through the Ni²⁺ cations. In order to estimate the amount of polymer attached to the IF-MoS₂ surface, we performed a thermogravimetric analysis (TG). The IF-MoS₂/polymer composite exhibits three thermal responses. The thermal decomposition of the polymer begins

at 150 °C and is finished after 435 °C. The final step around 650 °C may be related to a crystallization of the MoS₂ nanoparticles. The associated weight loss indicates that the amount of the polymer shell is comparable to that of MoS₂ itself (Figure 8.5d). An IF-MoS₂ particle, which has an average diameter of 30 nm and approx. 20 layers, has a mass of about 23×10^6 g/particle, which is 400 times the molar mass of a polymer molecule (58.5×10^3 g/mol).

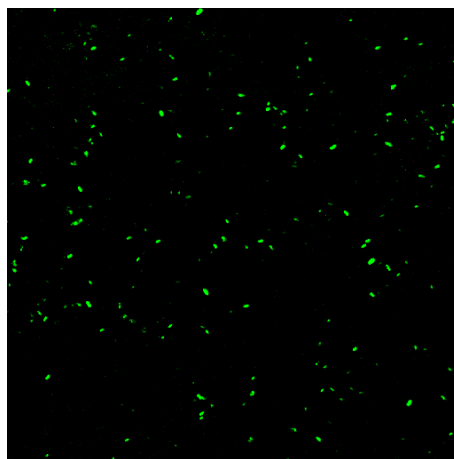


Figure 8.6. Fluorescence spectrum of IF-MoS₂ nanoparticles coated with a NBD fluorophore coupled to the NH₂ group of the NTA ligand. MoS₂ nanoparticles coated with NTA-NBD were excited at 488 nm.

Therefore, each MoS₂ particle is covered by about 400 polymer molecules. We can assume that most of the NTA anchor groups are attached to the surface. With an approximate surface area of 5000 nm² of an IF-MoS₂ particle we derive a surface area of approx. 13 nm² for a polymer molecule, if full surface coverage is assumed. For a polymer with ~ 250 monomer units, which carry an 80% NTA content, 6.5 Å² can be estimated as the surface volume covered by a single monomer unit. However, as the polymer is not likely to be wrapped smoothly around the surface, a somewhat lower coverage may be possible. In summary, the small surface area value obtained for a single monomer unit indicates a full surface coverage by the polymer.

Figure 8.6 shows the confocal laser scanning microscopy (CLSM) image of IF-MoS₂ after surface functionalization with a benzofurazene derivative (NBD, see Figure 8.1) of NTA exhibiting strong fluorescence when bound to primary or secondary amine groups. A 10 µl droplet of the sample was placed and dispersed carefully on a thin glass slide and the solvent

was evaporated. The fluorescence of the NBD dyes was excited at 488 nm and detected from 504 - 514 nm. A 40x (NA 1.25) oil immersion objective was used for the imaging. It is reasonable from the fluorescence images that the nanoparticles are fully coated by NTA ligands covalently bound to the IF-MoS₂ particle surface. It is, however, difficult to comment on the actual size of the functionalized nanoparticles because they are beyond the resolution limits of CLSM.

It is unclear so far, whether the Ni²⁺/NTA units are bound to the close packed sulfur surface layer of the MoS₂ nanocrystals or to defects present at the surface. The chemical reactivity of MoS₂ is associated with the edges of the sandwich layer whereas the basal planes are less reactive.

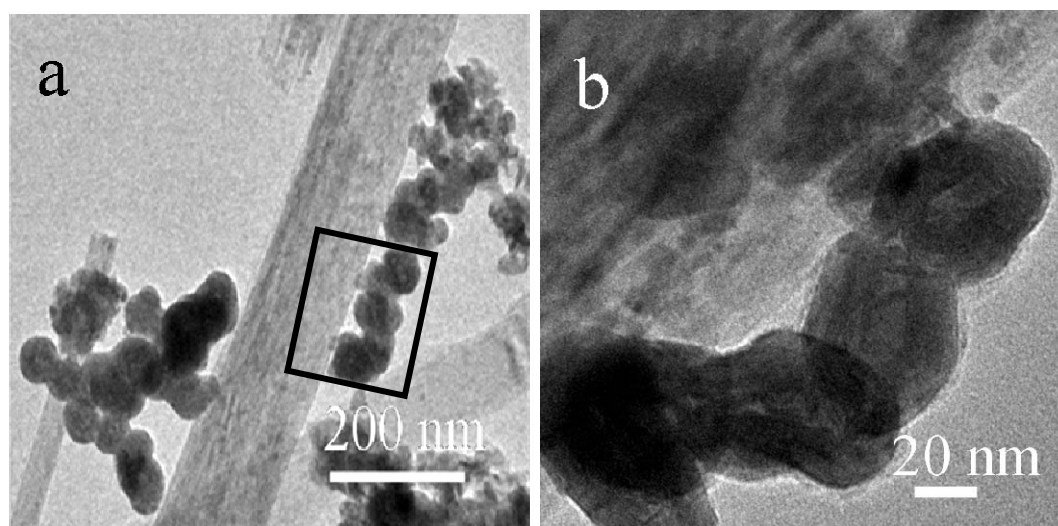


Figure 8.7. (a) TEM image of IF-MoS₂ particles immobilized on a TiO₂ nanorods by surface wall functionalization. (b) Magnified image of the rectangle marked in (a).

Therefore the edges form the sites where gases adsorb on MoS₂ in hydrodesulfurization catalysis,^[30] and it seems logical to expect that the edges (because of their higher surface energy) are the seat of surface binding as well. Similarly, catechol is known to bind preferentially to the edges of the TiO₂ nanocrystals (which have a higher surface energy).^[31] However, full surface coverage, protection and concomitant functionalization may be envisioned using the novel copolymer ligand containing a large number of NTA anchor groups covalently linked to the polymer backbone, thus sheathing the nanoparticles, partly by surface bound anchor groups and partly by steric shielding through the polymer ligand.

A final clue concerning the surface functionalization of IF-MoS₂ is based on the decoration of TiO₂ nanorods with IF-MoS₂ particles, using the catechol groups to bind to the TiO₂ nanorods. In the first reaction step the polymer ligand immobilized on the IF-MoS₂ nanoparticles and free catecholate groups were used to bind to undercoordinated surface sites of the TiO₂ nanorods. Figure 8.7(a and b) show TEM images of a TiO₂ nanorod with several IF-MoS₂ particles attached, whereas no unbound IF-MoS₂ particles are detectable in the sample. Without the presence of reactive ligands the wetting properties of TiO₂ and MoS₂ would preclude an aggregation of the hydrophobic MoS₂ particles on the hydrophilic TiO₂ surfaces. We note the aggregation behaviour of IF-MoS₂ particles at the TiO₂ surface, which may be rationalized by the simultaneous binding of several MoS₂ particles to a single multifunctional polymer ligand (due to the high NTA content of 80%).

8.3. Conclusion

In summary, we have used the principles of coordination chemistry and multipod ligand design to achieve the functionalization of highly inert MoS₂ nanoparticles through a high degree of surface binding. For this purpose we have used the tetradentate NTA ligand which was coupled either to a fluorescent ligand for detection purposes or to a reactive polymer, which simultaneously serves as an anchor to the sulfide (via the NTA groups) and the oxide surfaces (via the catecholate groups) of IF-MoS₂ and TiO₂. We believe that this functionalization protocol can be generalized for various layered chalcogenide nanoparticles. The functionalization of fullerene-type chalcogenide nanoparticles opens several new fields for this class of materials which have been pursued actively during the past few years for the related carbon nanotubes and various oxide materials: (i) the functionalization of chalcogenide nanotubes for the attachment of electronically active components (metal and semiconductor nanoparticles, light harvesting ligands for solar cell applications) to the sidewalls of the tubes, (ii) dispersion of nanotubes, e.g. for the integration in composites which is of interest because of their exceptional mechanical properties. (iii) Furthermore, it allows the fabrication of thin films by surface binding of chalcogenide particles to oxide surfaces, which might allow their use as lubricants on seemingly incompatible ceramic materials.

8.4. Experimental

IF-MoS₂ nanoparticles were synthesized according to the method recently reported by us.^[28] The active ester polymer **PFA** was prepared by free radical polymerization as reported earlier.^[29b] The obtained polymer had a molecular weight of $M_n = 29.7$ kg/mol; $M_w = 58.5$ kg/mol, where the number of repeating units (246) is based on the M_w value. These data were obtained by gel permeation chromatography (GPC) analysis in THF (light scattering detection). The functional polymeric ligand was synthesized by stirring a mixture of **PFA** (110 mg, 0.46 mmol repeating units) in 3 ml of dry DMF and 3-hydroxytyramine hydrochloride (10.5 mg, 0.055 mmol) in 1.5 ml of DMF and 0.1 ml of triethylamine at 50 °C for 1 hour. After that amino-functionalized **NTA** (120 mg, 0.46 mmol) in 0.9 ml of MilliQ water and 2.1 ml of triethylamine were introduced and the resulting mixture heated at 50 °C for additional 6 hours. **NTA** was added in a slight excess to ensure complete quenching of the polymeric active ester groups. DMF was removed and the obtained polymeric product cleaned by dialysis in MilliQ water. Finally the ligand was isolated and dried in a vacuum oven at 40 °C for 1 hour yielding 64 mg of a white polymeric powder.

¹H-NMR (DMSO-d₆): 7.5 – 6.5 ppm (3H, br m), 6.5 – 4.0 ppm (1H, br s), 3.96 – 3.19 (5H, br m), 3.17 – 2.66 (5H, br s), 1.87 – 0.34 (8H, br m). ¹⁹F-NMR (DMSO-d₆): no signals found. FT-IR (ATR mode): 3200 – 2400 cm⁻¹: COOH (**NTA**); 3045 cm⁻¹: arom. C=C-H (dopamine); 1639 cm⁻¹: N-H (prim. amide); 1199 cm⁻¹: C-N (prim. amide)

For the functionalization, 3 mg of IF-MoS₂ nanoparticles were dispersed in 2 ml of ethanol and sonicated for 15 minutes. In a separate vial 20 mg of polymer ligand or 20 mg of Lysine nitriloacetic acid (**NTA**) were dissolved in 10 ml of H₂O followed by the addition of 2 ml of 0.01 M NaOH and 2 ml of 40 mmol aqueous solution of NiSO₄. Both suspension and solution were mixed under inert conditions and stirred at 60°C for 4h. The polymer functionalized IF-MoS₂ particles were isolated and purified by repeated washing with H₂O using centrifugation to remove the unbound polymer and water soluble salt. To immobilize the IF-MoS₂ onto TiO₂ nanowires, 1 ml of polymer ligand functionalized IF-MoS₂ were mixed under inert condition in a glove box with pre-suspended TiO₂ nanorods (1 mg/ml) in H₂O. The TiO₂ nanowires coated with functionalized IF-MoS₂ nanoparticles were then centrifuged and dried under vacuum. The product was used as such for characterization.

Instrumental Analyses. The products obtained after functionalization and binding onto to nanowires were analyzed by FT-IR, UV-visible, confocal laser scanning microscopy (CLSM) and high resolution transmission electron microscopy (HRTEM). The morphology of the MoS₂ nanoparticles and onions was characterized by a high-resolution transmission electron microscopy (FEI Tecnai F30 ST operated at an extraction voltage of 300kV, equipped with an EDXA (energy dispersive X-ray spectrometer) and by selected area electron diffraction techniques (SAED). For transmission electron microscopic (TEM) studies, carbon film coated copper grids containing a drop of suspension of the sample in ethanol was used. The laser scanning microscope (Leica TCS SL, Leica Microsystems, Bensheim, Germany) with inverted laser was used for fluorescence images. UV-vis absorption spectra were taken with an Omega-10 spectrometer (Bruins Instruments).

8.5. References

- [1] (a) P. Ghosh, T. G. Spiro, *J. Am. Chem. Soc.* **1980**, *102*, 5543-5549. (b) D. C. Bookbinder, M. S. Wrighton, *J. Electrochem. Soc.* **1983**, *130*, 1080-1086. (c) W. E. Ford, M. A. Rodgers, *J. Phys. Chem.* **1988**, *92*, 3822-3841.
- [2] S. Anderson, E. C. Constable, M. P. Dare-Edwards, J. B. Goodenough, K. R. Seddon, R. D. Wright, *Nature* **1979**, *280*, 571-573.
- [3] T. A. Heimer, S. T. Dárcangelis, F. Farzad, J. M. Stipkala, G. J. Meyer, *Inorg. Chem.* **1996**, *35*, 5319-5324.
- [4] (a) P. Pechy, F. P. Rotzinger, M. K. Nazeeruddin, O. Kohle, S. M. Zakeeruddin, R. H. Baker, M. Grätzel, *Chem. Comm.* **1995**, 65-66. (b) G. Alberti, F. Marmottini, S. M. Mascaros, R. Vivani, *Angew. Chem.* **1994**, *106*, 1655-1658. *Angew. Chem. Int. Ed. Engl.* **1994**, *33*, 1594-1597. (c) A. Clearfield, C. Y. O. Avila, *ACS. Symp. Ser.* **1992**, *499*, 178-193. (d) M. Nagtegaal, J. Küther, J. Ensling, P. Gütllich, W. Tremel, *J. Mater. Chem.* **1999**, *9*, 1115-1120.
- [5] (a) T. E. Wolff, J. M. Berg, R. H. Holm, *Inorg. Chem.* **1981**, *20*, 174-180. (b) C. Bianchini, D. Masi, C. Mealli, A. Meli, G. Martini, F. Laschi, P. Zanello, *Inorg. Chem.* **1987**, *26*, 3683-3693.
- [6] Y. Li, C. Xu, B. Wei, X. Zhang, M. Zheng, D. Wu, P. M. Ajayan, *Chem. Mater.* **2002**, *14*, 483-485.
- [7] S. Iijima, *Nature* **1991**, *354*, 56-58.
- [8] R. Tenne, L. Margulis, M. Genut, G. Hodes, *Nature* **1992**, *360*, 444-446.
- [9] Y. Feldman, E. Wasserman, D. J. Srolovitz, R. Tenne, *Science* **1995**, *267*, 222-225.
- [10] R. Tenne, M. Homyonfer, Y. Feldman, *Chem. Mater.* **1998**, *10*, 3225-3238.
- [11] (a) G. Seifert, H. Terrones, M. Terrones, G. Jungnickel, T. Frauenheim, *Phys. Rev. Lett.* **2000**, *85*, 146-149. (b) G. Seifert, H. Terrones, M. Terrones, T. Frauenheim, *Solid State Comm.* **2000**, *115*, 635-638.
- [12] (a) L. Rapoport, Y. Bilik, Y. Feldman, M. Homyonfer, S. R. Cohen, R. Tenne, *Nature* **1997**, *387*, 791-793. (b) M. Chhowalla, G. A. J. Amaratunga, *Nature* **2000**, *407*, 164-167.
- [13] C. B. Murray, D. J. Morris, M. G. Bawendi, *J. Am. Chem. Soc.* **1993**, *115*, 8706-8715.
- [14] W. C. H. Chan, S. Nie, *Science* **1998**, *281*, 2016-2019.

- [15] M. J. O. Connell, P. Boul, L. M. Ericson, C. B. Huffmann, Y. H. Wang, E. Haroz, C. Kuper, J. M. Tour, K. D. Ausman, R. E. Smalley, *Chem. Phys. Lett.* **2001**, *342*, 265-271.
- [16] M. J. O'Connell, S. M. Bachilo, C. B. Huffman, V. C. Moore, M. S. Strano, E. H. Haroz, K. L. Rialon, P. J. Boul, W. H. Noon, C. Kittrell, J. Ma, R. H. Hauge, R. B. Weisman, R. E. Smalley, *Science* **2002**, *297*, 593-596.
- [17] M. Brust, M. Walker, D. Bethell, D. J. Schiffrin, R. Whyman. *Chem. Comm.* **1994**, 801-802.
- [18] G. Jander, E. Blasius, *Lehrbuch der analytischen und präparativen anorganischen Chemie*, Hirzel, Stuttgart **1970**.
- [19] G. Ebner, D. Schelz, *Textilfärberei und Farbstoffe*, Springer, Berlin, **1988**.
- [20] (a) N. T. Lucas, J. M. Hook, A. M. McDonagh, S. B. Colbran, *Eur. J. Inorg. Chem.* **2005**, 496-503. (b) C. R. Rice, M. D. Ward, M. K. Nazeeruddin, M. Grätzel, *New J. Chem.* **2000**, *24*, 651-652. (c) M. N. Tahir, M. Eberhardt, P. Theato, S. Faiß, A. Janshoff, T. Gorelik, U. Kolb, W. Tremel, *Angew. Chem.* **2006**, *118*, 922-926.
- [21] (a) Y. Bingwen, C. V. McNeff, P. W. Carr, A. V. McCormick, *J. Am. Ceram. Soc.* **2005**, *88*, 707-713. (b) C. V. McNeff, Y. Bingwen, S. Dwight, US Pat. US 2005023613.
- [22] (a) R. Laucournet, C. Pagnoux, T. Chartier, J. F. Baumard, *J. Eur. Ceram. Soc.* **2001**, *21*, 869-878. (b) G. S. Tulevski, Q. Miao, M. Fukuto, R. Abram, B. Ocko, R. Pindak, M. L. Steigerwald, C. R. Kagan, C. Nuckolls, *J. Am. Chem. Soc.* **2004**, *126*, 15048-15050.
- [23] L. Vermeulen, D. D. Baets, Eur. Pat. EP657297.
- [24] C. Xu, K. Xu, G. Gu, R. Zheng, H. Liu, X. Zhang, Z. Guo, B. Xu, *J. Am. Chem. Soc.* **2004**, *126*, 9938-9939.
- [25] (a) D. Kröger, M. Liley, W. Schiweck, A. Skerra, H. Vogel, *Biosensors & Bioelectronics*, **1999**, *14*, 155-161. (b) G. B. Sigal, C. Bamdad, A. Barberis, J. Strominger, G. M. Whitesides, *Anal. Chem.* **1996**, *68*, 490-497. (c) I. T. Dorn, K. R. Neumaier, R. Tampe, *J. Am. Chem. Soc.* **1998**, *120*, 2753-2763. (d) S. Hutschenreiter, L. Neumann, U. Rädler, L. Schmitt, R. Tampe, *ChemBioChem* **2003**, *4*, 1340-1344.
- [26] (a) C. Mealli, S. Midollini, L. Sacconi, Luigi. *Chem. Comm.* **1975**, 765-766. (b) C. Bianchini, C. Mealli, A. Orlandini, L. Sacconi, *Inorg. Chem.* **1980**, *19*, 2968-2975. (c)

- R. Alsfasser, S. Trofimenko, A. Looney, G. Parkin, H. Vahrenkamp, *Inorg. Chem.* **1991**, *30*, 4098-4100. (d) R. Alsfasser, M. Ruf, S. Trofimenko, H. Vahrenkamp, *Chem. Ber.* **1993**, *126*, 703-10. (e) M. A. Halcrow, B. Chaudret, S. Trofimenko, *Chem. Comm.* **1993**, 465-7. (f) S. Trofimenko, *Chem. Rev.* **1993**, *93*, 943-980. (g) S. Trofimenko, *Scorpionates: The Coordination Chemistry of Polypyrazolylborate Ligands*, Imperial College Press, London, **1999**.
- [27] (a) M. N. Tahir, P. Théato, W. E. G. Müller, H. C. Schröder, A. Janshoff, J. Zhang, J. Huth, W. Tremel, *Chem. Comm.* **2004**, 2848-2849. (b) M. N. Tahir, P. Théato, W. E. G. Müller, H. C. Schröder, A. Borejko, S. Faiß, A. Janshoff, J. Huth, W. Tremel, *Chem. Commun.* **2005**, 5533-5535.
- [28] J. Etzkorn, H. A. Therese, F. Rucker, N. Zink, U. Kolb, W. Tremel, *Adv. Mater.* **2005**, *17*, 2372-2375.
- [29] (a) I. Potavova, R. Mruk, S. Prehl, R. Zentel, T. Basche, A. Mews, *J. Am. Chem. Soc.* **2003**, *125*, 320-321. (b) M. Eberhardt, R. Mruk, P. Theato, R. Zentel, *Europ. Polym. J.* **2005**, *41*, 1569-1575.
- [30] K. Suzuki, M. Soma, T. Onishi, K. Tamaru, *J. Electron Spectros. Relat. Phenom.* **1981**, *24*, 283-286.
- [31] T. L. Villareal, A. Rodes, J. M. Perez, R. Gomez, *J. Am. Chem. Soc.* **2005**, *127*, 12601-12611.

9. Facile Synthesis and Characterization of Monocrystalline Cubic ZrO₂ Nanoparticles

9.1. Introduction

Zirconia is a special transition-metal oxide that possesses the bifunctional characteristics of weak acid and weak base properties.^[1, 2] The P-type semiconductor exhibits abundant oxygen vacancies on its surface. The high ion-exchange capacity and redox activities make it useful in many catalytic processes as catalyst,^[3] supporter,^[4] and promoter or in solid fuel cells.^[5] Zirconia-based ceramics are found in a remarkable variety of technological and commercial applications such as catalysts,^[3] oxygen sensors,^[6] high dielectric constant materials for very large scale integrated circuits, and as gate dielectrics in metal oxide-semiconductor devices.^[7] ZrO₂ has three polymorphs, of which the monoclinic phase is thermodynamically stable up to 1100 °C, the tetragonal phase exists in the temperature range 1100 -2370 °C, and the cubic phase is found above 2370 °C.^[8] Cubic ZrO₂ is a well known material with extreme refractoriness,⁹ high mechanical strength and fracture toughness,^[10] thermal insulation,^[11] wear and erosion resistance,^[12] chemical durability, and alkali resistance,^[13] which finds use in a variety of fields, in particular in constructional ceramics,^[14] biological ceramics,^[15] functional high temperature coatings,^[16] or heterogeneous catalytic processes.^[17] Several chemical and physical methods have been devised to synthesize cubic ZrO₂, such as thermal decomposition,^[18] chemical evaporation,^[19] sol-gel methods,^[20] and hydrothermal techniques.^[21] It is difficult to obtain cubic ZrO₂, because reactions towards ZrO₂ lead typically to mixed phases or the cubic phase has to be stabilized by rare earth oxides at high temperatures.^[22] Here we report on the facile synthesis and characterization of cubic ZrO₂ nanoparticles with control on morphology and crystallinity by a hydrothermal method. The reaction temperature we used is the lowest ever used in the synthesis of cubic ZrO₂ nanoparticles.

In a typical reaction 1 g of Zirconium isopropoxide (ACROS) was taken in a Teflon vessel and 6 ml of analytical grade Ethanol (99.8 %) were added. The Teflon vessel was kept in desiccator. The precipitation of ZrO₂ was initiated under moist atmosphere induced by

placing a petri dish filled with water at the bottom of the desiccator. The diffusion experiment was stopped after 12 hrs, followed by the addition of 25 ml of NaOH aqueous solution. Then the reaction vessel was sealed into a stainless steel hydrothermal bomb, which heated at 180 °C for 18 hrs. After the autoclave was cooled down to room temperature, the products were filtered and repeatedly washed with 0.1 M HNO₃, 1 N HCl and deionized water. After drying under vacuum (3h) a white soft and fibrous powder was obtained.

Samples obtained by hydrothermal synthesis with sodium hydroxide in concentrations of 10mol (10M), 5mol (5M) and 3mol (3M) were investigated by high resolution electron microscopy (HRTEM, FEI Tecnai F30 ST equipped with a field emission gun at 300 kV), electron diffraction (ED, 10 μm C2 aperture using a beam of approx. 20 nm in diameter) and X-ray powder diffraction (Bruker D8 powder diffractometer operated in θ -2 θ mode, Cu radiation, Sol-X detector). EDX measurements were carried out with an energy dispersive x-ray spectroscope (EDAX, Tilburg, and The Netherlands) with an ultra thin polymer window and Si/Li detector. Data processing was performed with self-made scripts in the program DM3 (Gatan). Further characterization was performed by Raman spectroscopy (Jobin Yvon LabRAM HR800 confocal Raman system equipped with an optical microscope Olympus BX41 and Peltier-cooled CCD detector, 638.17 Å He-Ne Laser) and fluorescence and photoluminescence spectroscopy (Bruins Omega-10 spectrometer and ISA Fluoromax-II fluorometer). The specific surface area was measured using the Brunauer–Emmett–Teller (BET) nitrogen-gas adsorption.

9.2. Results and discussion

TEM images of ZrO₂ nanoparticles (3M) are given in Figure 9.1a together with a diffraction pattern of the [100] zone (Figure 9.1b). Elongated platelets of approx. 400-500 nm length (*c* axis) and 100-200 nm width (*b* axis) are oriented with the (100) face on the carbon support film as indicated in the sketch given in Figure 9.1c. A tilt around the *b* axis delivers two patterns of the [100] zone with an angle of about 20° between them. This directly points to a twinning along the *a*-axis of the monoclinic structure (Figure 9.1c) and confirms the monoclinic angle of ~100° (90+20/2°) (monoclinic ZrO₂: P2₁/c, *a* = 5.17Å, *b* = 5.20 Å, *c* = 5.14 Å, β= 99.7°, ICSD 94887). The twinned domains have collinear *b* and *c* axes. The crystals show the smallest growth rate in the *a* direction where the twinning occurs and the

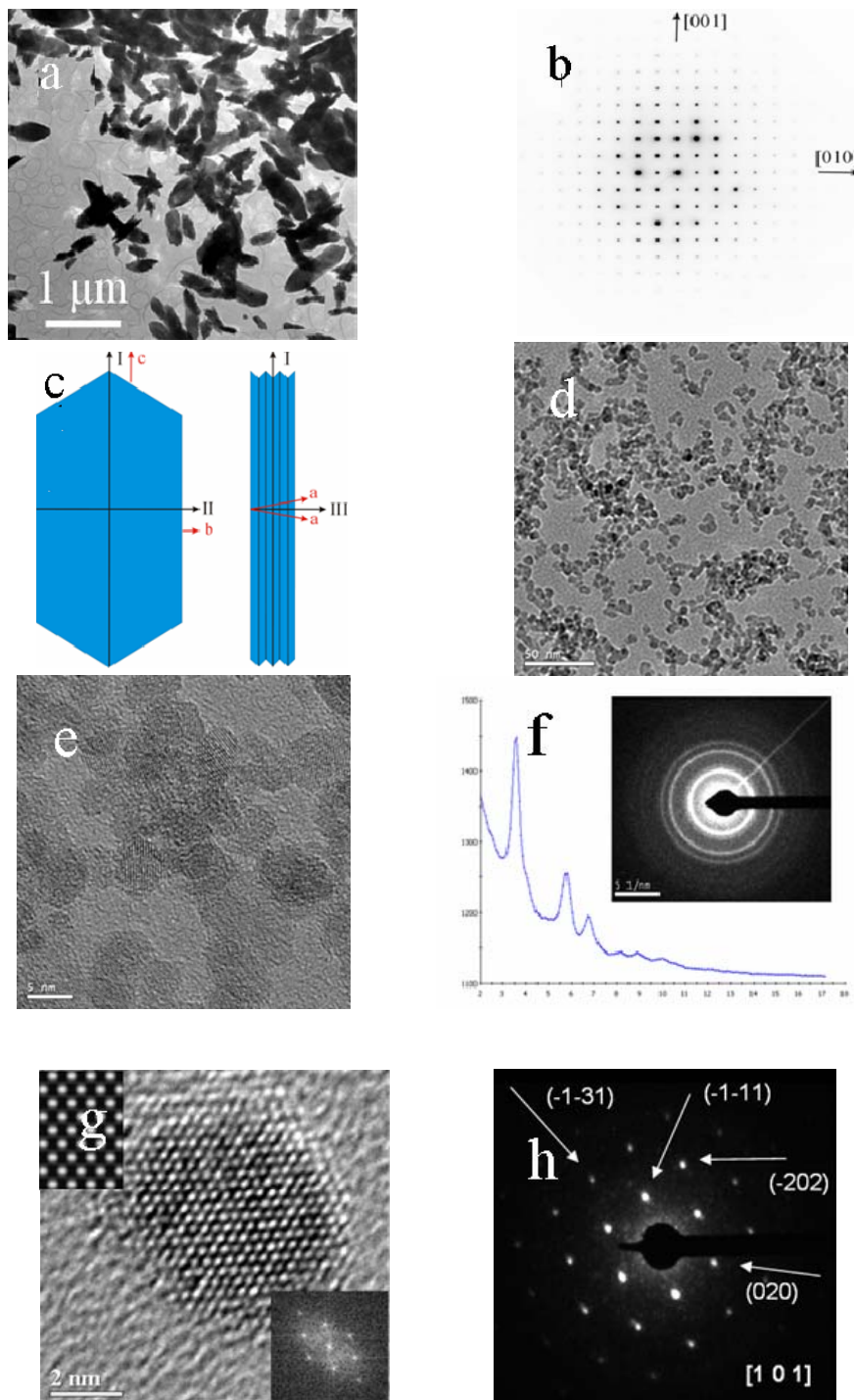


Figure 9.1. TEM images of ZrO_2 nanoparticles a) overview 3M NaOH, b) diffraction pattern, c) growth of crystal d) and e) overview of cubic ZrO_2 nanoparticles with 10M NaOH, f) TEM powder diffraction, g) HRTEM of single nanoparticle, simulated HRTEM image (top left side) and FFT (bottom right side) h) HRTEM diffraction pattern

highest growth rate in c direction where a zigzag border is visible. The TEM images of 5M ZrO_2 nanoparticles delivered particles identical to 3M ZrO_2 . TEM images of 10M ZrO_2 together with the corresponding diffraction patterns are shown in Figure 9.1(d-h). Figure 9.1(d and e) show spherical agglomerated ZrO_2 nanoparticles in a size range of 6-7 nm. The corresponding electron powder diffraction pattern (Figure 9.1f) fully agrees with the d values calculated for cubic ZrO_2 . For a tetragonal structure one additional reflection would be observed (black arrow).

The elemental composition of 10 M ZrO_2 has been confirmed by EDX spectroscopy. The HRTEM image of a single nanoparticle (Figure 9.1g) confirms the cubic structure. The electron diffraction pattern of the [101] zone of the same particle nicely agrees with the Fourier Transform (FFT) of the HRTEM image shown as an inset (bottom). In a second inset (top) a multi slice simulation^[23] of the HRTEM for the view down [101] is provided at Scherzer focus assuming a thickness of 7 nm.

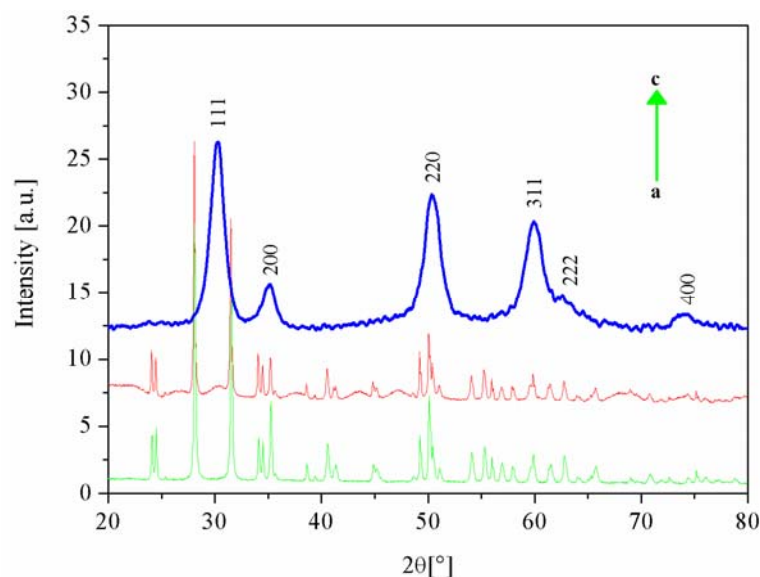


Figure 9.2. XRD powder pattern of as synthesized ZrO_2 nanoparticles from a) 3M NaOH, b) 5M NaOH c) 10M NaOH

The XRD pattern of 3M ZrO_2 (Figure 9.2) could be indexed unambiguously to monoclinic ZrO_2 . The narrow linewidths indicate the high crystallinity of the material. Based on the XRD pattern, samples of 5M ZrO_2 contain a mixture of the monoclinic and cubic phases, whereas the XRD pattern of 10 M ZrO_2 shows only broad reflections originating from cubic ZrO_2 nanoparticles. The particle size analysis based on Scherrer's formula^[24] of 10M ZrO_2 delivered $5 \times 5 \times 5$. Since it was not possible to clearly distinguish between cubic and tetragonal ZrO_2

based on the XRD data only, the formation of bulk quantities of the cubic phase was confirmed by Raman spectroscopy.^[22]

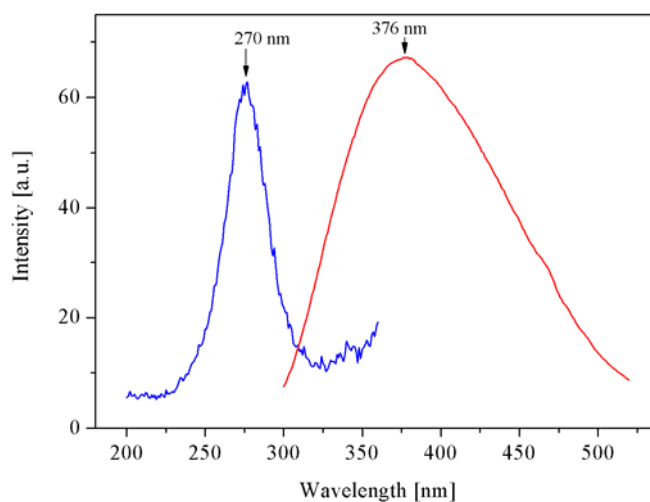


Figure 9.4. Photoluminescence spectrum of ZrO_2 nanoparticles synthesized using 10M NaOH excited at $\lambda = 270$ nm. (red color), the excitation spectrum of the

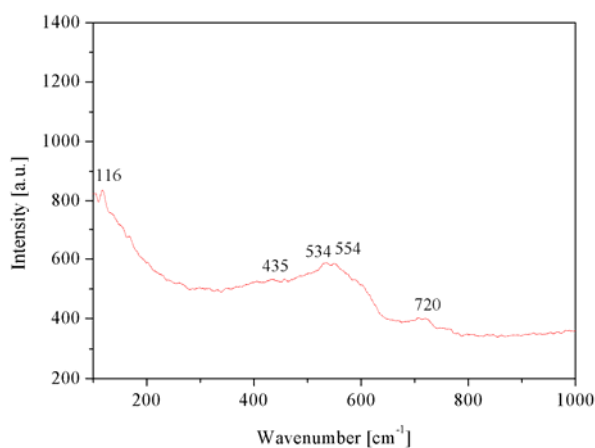


Figure 9.3. Raman spectrum of cubic ZrO_2 nanoparticles synthesized using 10M NaOH.

The cubic to tetragonal phase transition in doped zirconia occurs by elongation of the crystallographic c axes and a concomitant displacement of the oxygen atoms from the ideal

anion sites in the fluorite structure. Raman spectroscopy is sensitive to the polarizability of the oxygen ions, and therefore it can be used to determine the symmetry of a crystal system.

The Raman spectrum for cubic ZrO_2 is characterized by a broad band near $530-670\text{ cm}^{-1}$ and additional poorly defined features related to the disordered oxygen sublattice whereas tetragonal ZrO_2 delivers because of the symmetry reduction several well-defined sharp bands.^[25]

The Raman spectrum of 10M ZrO_2 (Figure 9.3) with a broad band between 530 and 640 cm^{-1} and a maximum at 550 cm^{-1} is in accordance with the presence of cubic ZrO_2 . A very weak band at 116 cm^{-1} may indicate the presence of small impurities from the tetragonal phase. Fluorescence spectra were measured with several excitation wavelengths between 245 and 290 nm . While the fluorescence intensity changes to some extent with the excitation wavelength, the fluorescence band position and the band shape remained about the same for excitation wavelengths below 290 nm . This indicates that the fluorescence involves the same initial and final states even when the excitation wavelength is varied between 245 and 290

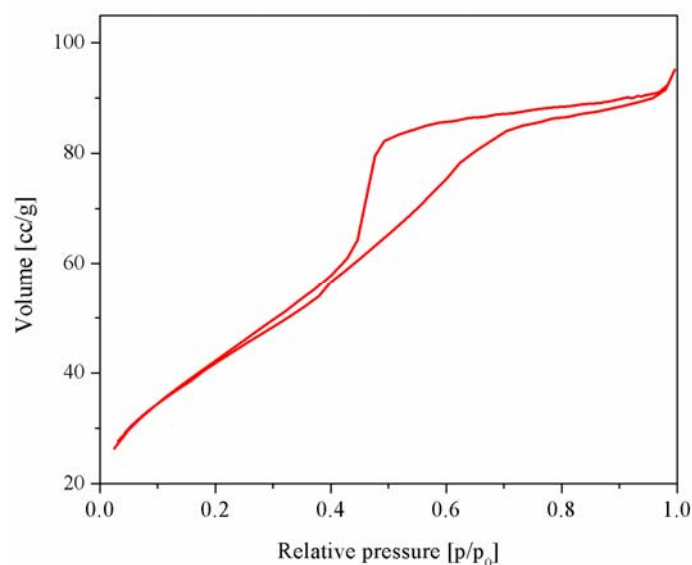


Figure 9.5. BET isotherm at 675K: N_2 on ZrO_2 10M NaOH.

nm. This result can be explained by fast relaxation from the final state reached by photo-excitation to those states from which the fluorescence originates.

Figure 9.4 show one representative fluorescence spectrum with excitation wavelength of 270 nm . The spectrum features a broad fluorescence band centered on 376 nm . The broad band and the substantial red shift of the band maximum compared to the band gap (5.6 eV) of the bulk

material^[26] strongly indicate that the fluorescence involves extrinsic states. Because the particle size distribution is very narrow, the broad fluorescence band seems to be mostly caused by the small particle size leading to an inhomogeneous broadening from a distribution of surface or defect states.

The BET surface area ($300 \text{ m}^2/\text{g}$) of measured for the cubic ZrO_2 nanoparticles (Figure 9.5) are significantly higher compared to the reported values.^[27] i.e. respectively. This could be attributed to the small particle size. The approximation between the measured and the model surface area confirms the observation from TEM, i.e. the product being composed of loosely aggregated agglomerates with a very open microstructure; as a result, almost the whole surface of each spherical particle is accessible to the N_2 molecules.

9.3. Conclusion

In summary, ZrO_2 nanoparticles have been synthesized using hydrothermal methods under mild conditions. The morphology, structure and properties of as synthesized nanoparticles were characterized using HRTEM, XRD, Raman spectroscopy, UV-vis, PL spectroscopy and BET measurements. Depending on the reaction conditions, ZrO_2 nanoparticles could be produced in form of the pure monoclinic and cubic polymorphs. The formation of both, the monoclinic and the cubic structure was confirmed by electron microscopy and Raman spectroscopy. Under the reaction conditions used in this work, the phase formation can be controlled, i.e. making the formation of the high-temperature cubic phase preferred over that of the thermodynamically stable low-temperature cubic phase. Furthermore, the crystallinity and morphology of the resulting ZrO_2 nanoparticles can be adjusted. The cubic ZrO_2 nanoparticles have a high surface area ($300 \text{ m}^2/\text{g}$) and exhibit strong photoluminescence in the UV region. This suggest that the as synthesized ZrO_2 nanoparticles may find use as luminescent labels and light emitting molecular substances in nanoscale photoluminescent or nano-optoelectronic devices and as optical memory materials in optical memory systems.

9.4. Experimental

1 g of Zirconium isopropoxide (ACROS) was taken in a Teflon vessel and 6 ml of analytical grade Ethanol (99.8 %) were added into it. The Teflon vessel was kept in desiccator. The precipitation of ZrO_2 was initiated under moist atmosphere induced by placing a petri dish filled with water at the bottom of the desiccator. The diffusion experiment was stopped after 12 hrs, followed by the addition of 25 ml of 10 M NaOH aqueous solution. Then the reaction vessel was sealed into a stainless steel hydrothermal bomb, which was placed in an oven maintained at 180 °C for 18 hrs. After the autoclave was naturally cooled to room temperature, the obtained sample was filtered and repeatedly washed with 0.1 M HNO_3 , 1 N HCl and deionized water. The samples were dried under vacuum for 3 hrs. Finally soft, fibrous powder with white colour was obtained.

High resolution (HRTEM) images were obtained with a transmission electron microscope FEI Tecnai F30 ST equipped with a field emission gun at 300 kV. The samples were prepared by drop casting from ethanol on Cu-grids with amorphous carbon support film. Diffraction patterns have been taken with a 10 μm C2 aperture using a beam of approx. 20 nm in diameter. EDX measurements were carried out with an energy dispersive x-ray spectroscopy (EDAX, Tilburg, and The Netherlands) with an ultra thin polymer window and Si/Li detector. Data processing was performed with self-made scripts in the program DM3 (Gatan).

X-ray powder diffraction in reflection geometry, (Siemens D8 powder diffractometer, $CuK\alpha$ radiation).

Raman microspectroscopy was performed with a LabRAM HR800 (Jobin Yvon, Horiba). This confocal Raman system is based on a dispersive spectrometer with notch-filter and focus length of 800 mm. It is equipped with an optical microscope Olympus BX41 and Peltier-cooled CCD detector (charge-coupled device). The spectra were excited with a 638.17 Å emission of a He-Ne laser. UV-vis absorption spectra were taken with an Omega-10 spectrometer (Bruins Instruments), and photoluminescence (PL) spectra were taken with a Fluoromax-II fluorometer (ISA).

9.5. References

- [1] C. L. Su, J. R. Li, D. H. He, *Appl. Catal. A* **2000**, *202*, 81-89.
- [2] M. S. Wong, D. M. Antonelli, J. Y. Ying, *Nanostruct. Mater.* **1997**, *9*, 165-168.
- [3] A. Caballero, J. J. Morales, A. M. Cordon, J. P. Holgado, J. P. Espinos, A. R. G. Elipe, *Journal of Catalysis* **2005**, *235*, 295-301.
- [4] Y. M. Li, D. H. He, Z. X. Cheng, C. L. Su, J. R. Li, Q. M. Zhu, *J. Mol. Catal. A: Chem.* **2001**, *175*, 267-275.
- [5] P. Egger, G. D. Soraru, S. Dire, *Journal of the European Ceramic Society* **2004**, *24*, 1371-1374.
- [6] E. C. Subbarao, H. S. Maiti, *Adv. Ceram.* **1988**, *24*, 731-747.
- [7] G. D. Wilk, R. M. Wallace, *Appl. Phys. Lett.* **2000**, *76*, 112-114.
- [8] a) T. Chraska, A. H. King, C. C. Berndt, *Materials Science and Engineering* **2000**, *A286*, 169-178.
- [9] R. A. Synowicki, T. E. Tiwald, *Thin Solid Films* **2004**, *248*, 455-456,
- [10] E. S. Lukin, E. V. Anufrieva, N. A. Makarov, N. A. Popova, A. L. Kuteinikova, *Refractories and Industrial Ceramics* **2004**, *45*, 421-423.
- [11] M. J. Maloney, *Eur. Pat. Appl.* **2000**, *23pp*, EP 992603.
- [12] O. Hiroshi, S. Miyuki, K. Toshio, *Jpn. Kokai Tokkyo Koho.* **2001**, *8pp*, JP 2001316178.
- [13] T. Limin, *Applied Optics* **2002**, *41*, 3804-3808.
- [14] R. C. Garvie, R. C. J. Hannink, N. A. McKinnon, *Eur. Pat. Appl.* **1980**, *51pp*. EP 13599 19800723.
- [15] X. X. Feng, L. R. Fang, Z. Y. Zeng, *Wuji Huaxue Xuebao* **2005**, *21*, 965-970.
- [16] E. Celik, E. Avci, Y. S. Hascicek, *Surface and Coatings Technology* **2002**, *161*, 179.
- [17] (a) Y. Yamada, A. Ueda, H. Shioyama, T. Maekawa, K. Kanda, K. Suzuki, T. Kobayashi, *Meas. Sci. Technol.* **2005**, *16*, 229-233. (b) M. J. Maloney, *Eur. Pat. Appl.* **2000**, *23 pp*, EP 992603 A1 20000412.
- [18] J. C. Ray, P. Pramanik, S. Ram, *Mater. Lett.* **2001**, *48*, 281-291.
- [19] L. A. Tietz, C. B. Carter, D. K. Lathrop, S. E. Russek, R. A. Buhrman, J. R. Michael, *J. Mater. Res.* **1989**, *4*, 1072-1081.

- [20] Y. W. Zhang, Z. G. Yan, F. H. Liao, C. S. Liao, C. H. Yan, *Mater. Res. Bull.* **2004**, *39*, 1763-1777.
- [21] G. Xu, Y. W. Zhang, C. S. Liao, C. H. Yan, *Solid State Ionics* **2004**, *166*, 391-396.
- [22] C. M. Wang, S. Azad, S. Thevuthasan, V. Shutthanandan, D. E. McCready, C. H. F. Peden, *J. Mater. Res.* **2004**, *19*, 1315-1319.
- [23] S. Diego, Cerius 4.6, *Accelrys Inc.*
- [24] P.G. Scherrer, *Nachr.* **1918**, *2*, 98-100.
- [25] C. N. Chervin, B. J. Clapsaddle, H. W. Chiu, A. E. Gash, J. H. Satcher, S. M. Kauzlarich, *Chem. Mater.* **2005**, *17*, 3345-3351.
- [26] J. Petry, W. Vandervorst, T. Conard, *Mater. Sci. Engineer. B* **2004**, *109*, 56.
- [27] A. Ahniyaz, T. Fujiwara, T. Fujino, M. Yoshimura, *Journal of Nanoscience and nanotechnology* **2004**, *4*, 233-238.

10. Mineralisation of CdS on Gold Colloids Using Metal-Organic-Inorganic Architecture

10.1. Introduction

Nanocomposites have attracted the attention of technologists over the last decade because of their prominent roles in basic science and technical applications. Their unique optical, electronic, and magnetic properties have urged the researchers to refine their synthetic arsenal in order to fabricate sophisticated systems with ever higher quality and complexity.^[1,2,3] Significant effort has focused on the ability to obtain control of the nanoscale structures via innovative synthetic approaches. The properties of nano-composite materials depend not only on the properties of their individual parents but also on their morphology and interfacial characteristics. Core-shell structures provide one method to modify the properties of nanoparticles.^[4,5,6,7] Such core-shell nanoparticles have become attractive because of the advantages provided by combining the properties of different materials in a well-defined fashion. The synthesis of semiconductor-metal composites with core-shell structure provided a new way to tailor the optical and electronic properties of semiconductor and metal nanoparticles.^[8] Such composite nanoparticles often exhibit improved physical and chemical properties over the single parent components, making them attractive from both scientific and technological viewpoints.^[9,10,11]

Gold nanoparticles constitute a specific class of such systems, since they are the fundamental building blocks for nanotechnology with applications ranging from catalysis to optical devices.^[12] On the other hand, CdS semiconductor nanoparticles are widely investigated due to their potential applications in many fields.^[13,14] Combining these two nanomaterials provides a model for further understanding the core-shell heterostructure and their properties. There has been little research related to the Au core and chalcogenide shell system. For example, Kamat and Shanghavi reported the synthesis of Au particles of 20 nm coated by CdS nanoclusters of around 4 nm, where a bleaching of the surface plasmon band and charge separation were observed.^[15] It is still difficult to grow semiconductor shells on metal particles directly due to the large lattice mismatch between metals and semiconductors.

We have used self-assembled monolayers (SAMs) of thiols on gold surfaces for a variety of new functionalizations. Using suitable thiols we have attached polymerization catalysts on

colloid surfaces,^[16] Thiol monolayers on planar gold surfaces were used to immobilize protein as biocatalyst to mediate the biocatalytically templated synthesis of inorganic minerals such as SiO_2 ,^[17] TiO_2 and ZrO_2 .^[18] The use of thiol monolayer surfaces on gold in templating the crystallization of inorganic minerals such as calcium carbonate^[19,20] has been extended by us to the use of thiol-coated colloids as crystallization nuclei.^[21,22] This has opened a new dimension to surface-templated crystallizations since a dispersed, spherical colloid offers a very different geometry from a large, planar Au(111) surface. Using self-assembled monolayers with suitable surface functionality (the ω group on the long chain) compatible with the envisioned application of the colloids on metal colloids offers a facile procedure to synthesize hybrid materials.^[23] However, the reactive ω group must be inert towards the metal surface or should be protected to avoid the crosslinking of metal nanoparticles. As an example, SH when used as an ω group offers a surface which is compatible for the inorganic metal sulfides. However, if dithiols are added to a gold colloid solution, immediate precipitation results owing to the cross-linking of the gold colloids.

This drawback can be circumvented by using a strategy borrowed from peptide chemistry that uses a protection group for the thiol functionality which can easily be removed in a second reaction step.^[24] The half protected dithiol is illustrated in Figure 10.1. The gold colloids were prepared by phase transfer catalysis method employed by Brust et al.^[25]

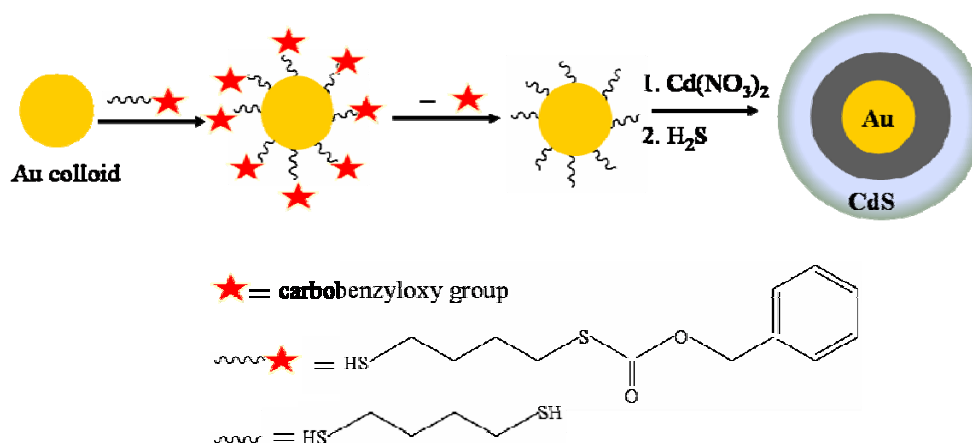


Figure 10.1. Schematic illustration of the synthesis of thiol functionalized Au colloids.

The thiols have been assembled on gold colloids in a toluene solution. The colloids are precipitated by and washed with methanol followed by redissolving them in CH_2Cl_2 where

the protecting group is removed with aq. NH_3 . These ‘sticky’ colloids are then dissolved in THF and 3 ml of $\text{Cd}(\text{NO}_3)_2$ (3 mmol) in a desiccator and exposed to H_2S aqueous solution.

10.2. Results and discussion

Figure 10.2 shows the absorption spectra of as-synthesized gold colloids, gold colloids surface-modified with deprotected thiol, gold colloids with a CdS shell grown on the deprotected thiol after 2, 8, and 16 hours as well as the absorption spectrum of CdS nanoparticles mineralized

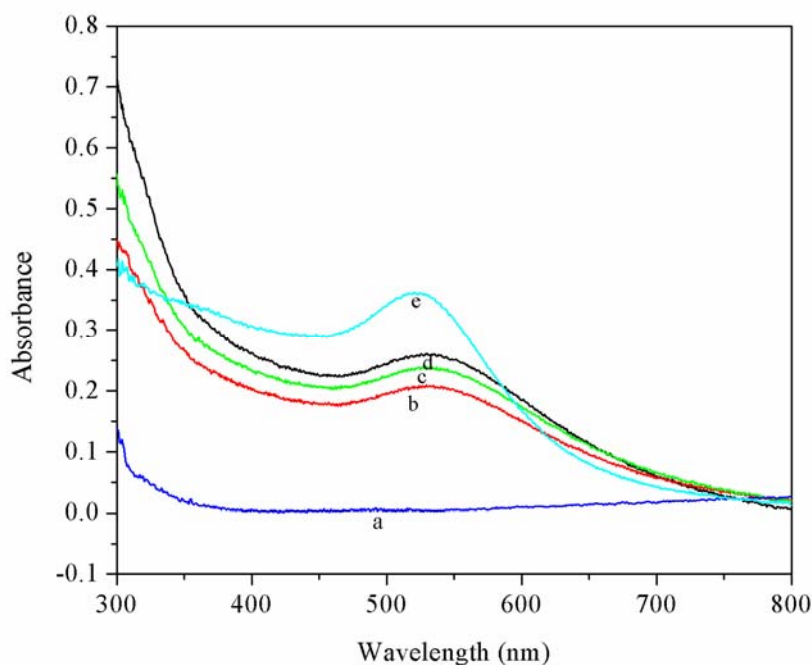


Figure 10.2. UV-vis absorption spectra of (a) CdS precipitated in the absence of Au colloids (16 hours) b) Au-CdS nanocomposites (2 hours) c) Au-CdS nanocomposites (8hours) d) Au-CdS nanocomposites (16hours), e) thiol functionalized gold colloids.

in the absence of gold colloids. The as-synthesized Au colloids and the colloids carrying the half-protected thiol exhibit an absorption maximum around 520 nm corresponding to the surface plasmon band. The Au colloids with a CdS layer deposited on the unprotected thiols (Au/CdS colloids) exhibit a strong absorption in the UV and the visible region, with an absorption edge extending up to 700 nm. The absorption spectra recorded in Figure 10.2 did not indicate any aggregation of thio-capped gold particles. The absorption of the Au/CdS

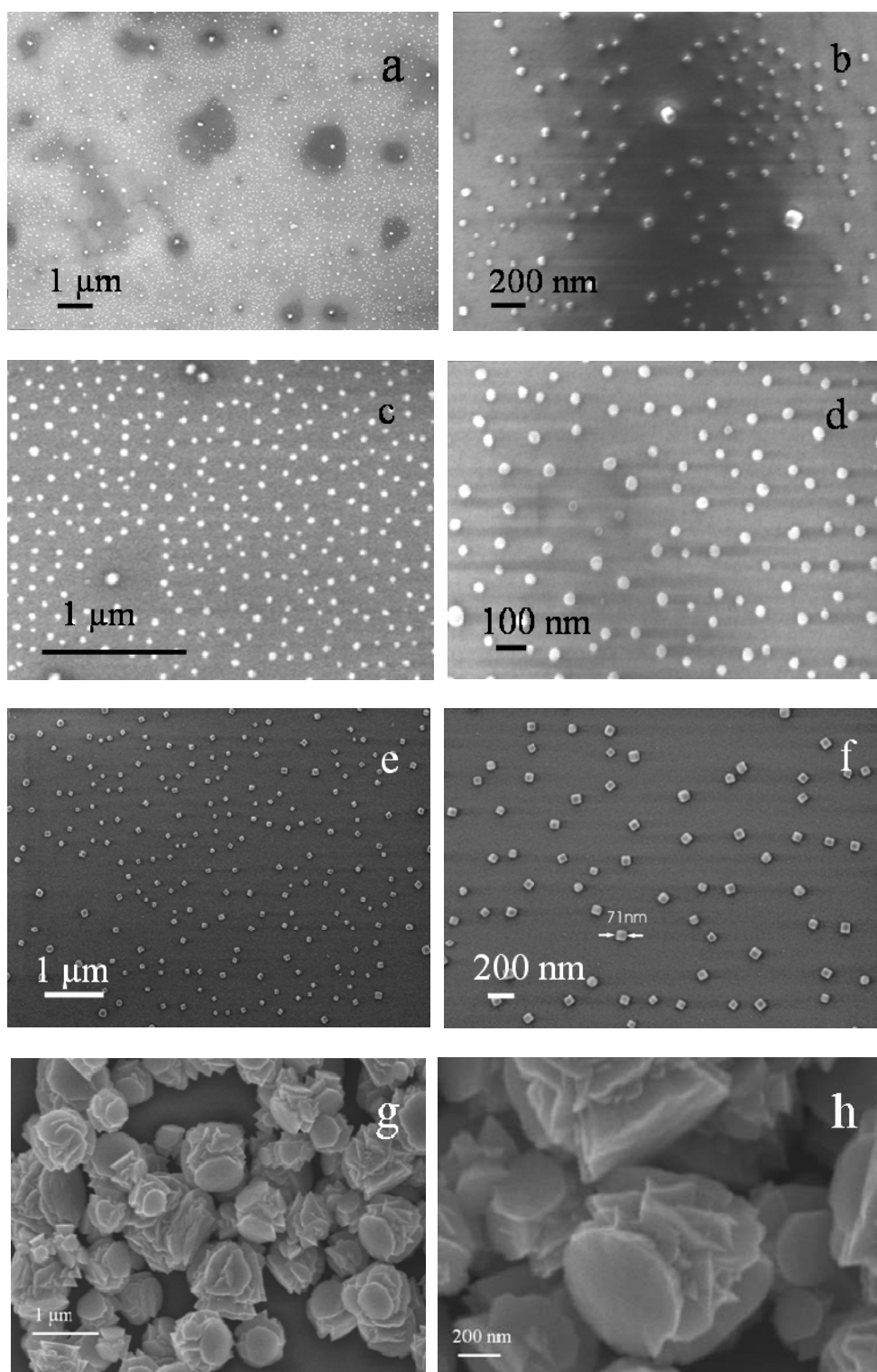


Figure 2. SE micrographs of Au/CdS nanocomposites grown on functionalized Au-colloids, (a and b) 2 hours, (c and d) 8 hours, (e and f) 16 hours, whereas (e and f) show the SE micrograph of CdS precipitated in the absence of Au colloids

nanoparticle system displays a Au plasmon absorption band with an absorption maximum at 533 nm. The absorption spectrum of the CdS nanoparticles mineralized in the absence of gold colloids shows only absorption edge around 400 nm. The sharp increase in the absorption at wavelengths below 450 nm confirms the formation of CdS nanoclusters around colloidal templates. It is interesting to note that the absorption of Au/CdS nanoparticles in the visible region is greatly increased and the surface plasmon absorption band is red shifted by about 13 nm as compared to the gold colloids. This suggests that the absorption properties of Au/CdS are not the result of a simple addition of the spectra of two nanoclusters, but indeed, the CdS shell influences the surface plasmon absorption of the gold core. Such an influence of a semiconductor shell on the electronic properties of the core material has recently been reported for a variety of semiconductor systems.

Figure 10.3 shows SEM micrographs of CdS nanoparticles grown from THF solutions in the presence of deprotected thiol after time intervals of 2, 8, and 16 hours, respectively. The CdS shell on the functionalized gold colloids shows a steady increase in size with time. As can be seen from Figure 10.3(a and b), Au-CdS nanocomposites were formed within two hours of reaction time are monodispers with an average particles size of ~ 23 nm. Increasing the reaction time to 8 hours leads to an increase of the particles size to ~ 48 nm while the cubic particle morphology is retained (Figure 10.3(c and d)). Cube-shaped nanoparticles Figure 10.3(e and f) with an average size of ~ 71 nm were formed when the reaction time was increased to 16 hours, beyond this time limit no distinct change of size and morphology was observed. Although we are unable to establish whether particle growth is initiated by a single colloidal particle, the uniform size and morphology of the CdS nanoparticles suggests that the nucleation and growth are caused by an identical sequence of processes. In a control experiment, where the crystallization was carried out in the absence of colloids, we have determined that it is the colloid that leads in the morphologies displayed in Figure 10.3(a-f). CdS precipitated in the absence of thiol functionalized gold colloids forms CdS particles with flower shaped morphology (Figure 10.3(g and h)). In a second control experiment we have shown that the crystallization in the absence of functionalized colloids, but in the presence of the thiol alone leads to similar results, i.e. the well defined particle morphologies shown in Figure 10.3(a-f) are caused by a template effect of the functionalized colloids and not by the inhibition of certain surfaces.^[26]

The initial growth of CdS starts in the solution as a result of interaction between Cd^{2+} ions and ω SH group of functionalized gold colloids. The further growth of the CdS shell results from

the formation of S^{2-} ions in the solution from the H_2S atmosphere inside the desiccator and their diffusion to the surface of the functionalized Au colloids carrying a surface bound Cd^{2+} cations. These first formed Au/CdS nanoparticles act as nuclei for further growth of CdS shell. As, with the passage of time, the weight of the Au/CdS nanoparticles increases the effect of gravitation pull causes them to fall on the glass substrate at the bottom of the reaction vessel.

The deposition of CdS continues even on the nanoparticles lying on the glass substrate. The uniform deposition of CdS ultimately leads nanoparticles with cubic morphology (which is typical for CdS nanoparticles) and diameters of approx. 70 nm. Hence one can assume that SH (ω group) functionalized gold colloids play a vital role in defining the shape of nanocomposites.

However, when the reaction temperature was increased from room temperature to 45 °C, nanowires with diameters of 50-60 nm and with length of several micrometers were exclusively grown on the substrate. Figure 10.4 shows the SEM micrographs of these nanowires. Figure 10.4a shows an overview image, whereas the Figure 10.4b is the high resolution (HRSEM) image of the resulting nanowires.

The temperature increase enhances the rate of diffusion of S^{2-} ions in solution which results a rapid growth of the CdS shell around gold colloids and hence a fast deposition of Au/thiol/CdS composites on the substrate in the form of clusters to produce some islands on

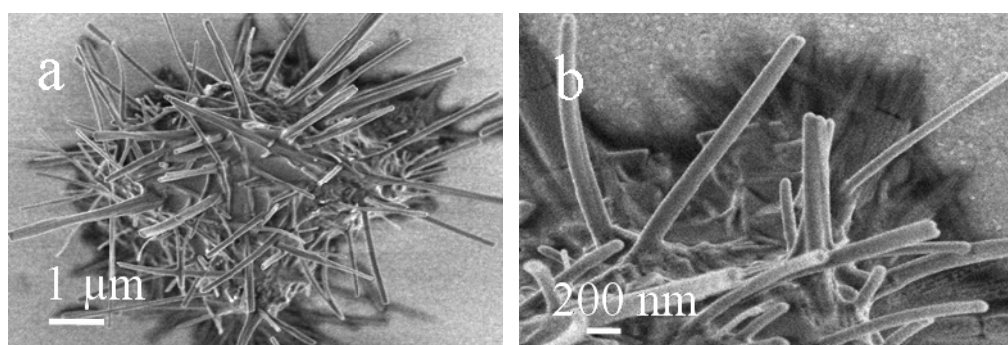


Figure 10.4. SE micrograph of CdS nanowires synthesized using thiol protected gold colloids at 45 °C. a) overview, b) HRSEM

the substrate at the bottom of reaction vessel. As the concentration of Cd^{2+} and S^{2-} ions decreases in solution, the anisotropic growth of nanowires takes place. A possible mechanism

for the anisotropic growth process of these nanowires could be related to the vapour-liquid-solid (VLS) growth of the nanowires proposed by Wagner for the growth of whiskers in the micrometer range,^[27] or the formation of asymmetric on-sided tipped semiconductor nanorods.^[28] In the former case, islands of metals, e.g. Au, are deposited on a substrate (e.g. a Si wafer) where they act as nuclei for the growth of micro- or nanocrystals at elevated temperature, whereas in the latter gold nanoparticles attached to the end of a CdSe nanocrystal are involved in the ripening process and the growth of nanorods from nanodots. However, as the Au colloids are covered with organic molecules and CdS deposited in the beginning, it is reasonable to consider Au/CdS clustered islands on the substrate to serve as the nucleation centres for the nanowires. This is supported by the fact that these nanowires grow only in the areas, where Au/CdS composites have already made these islands as obvious from the SE micrographs.

Sears' crystal growth theory can be used to explain the initialization of the one dimensional growth of nanowires as follows "if the supersaturation is below the value required for the formation of a crystal of some material with euhedral morphology, anisotropic one-dimensional growth in specific crystal directions take place".^[29] This is difficult to say whether the nanowires are Au/CdS nanocomposites or only of CdS in composition but under long exposure to electron beam of SEM, these curls showing no metal in inside.

10.3. Conclusion

In conclusion, gold colloids have been functionalized using half protected alkane thiol which is subsequently deprotected on the surface of gold colloids. These functionalized gold colloids were used to synthesize spherical or cubic shaped Au/CdS nanocomposites of uniform size depending on the reaction time. Nanowires were grown on the glass substrate by increasing the reaction temperature.

10.4. Experimental

The dithiols were prepared from *n*-dibromo alkanes using the Bunte Salt method.^[30,31] The protection of one of the thiol groups using the benzoyloxycarbonyl modification.^[32] Briefly, to the dithiol (5 g) in acetone (50 ml) with 2 M NaOH in water (60 ml), benzoyloxycarbonyl chloride (2.8 g) in acetone (20 ml) and 2 M NaOH (40 ml) in water were added simultaneously dropwise, over 30 min while cooling with ice. After stirring overnight at room temperature, the acetone was removed and the residue was worked up with diethyl ether. The organic layer was separated and chromatographed on silica to separate half protected thiol from the unprotected and diprotected compounds. Gold colloids were prepared in toluene following the method of Brust *et al.*¹¹ Deprotection could be carried out with aq. NH₃ (40 ml) in CH₂Cl₂ (40 ml), stirring overnight. The deprotected colloids in the organic layer were collected after removing the solvent and dissolved in THF for the crystallization experiments. Crystallization of CdS was carried out using an aqueous solution (3 mmol) of Cd(NO₃)₂ (3 ml) in THF (100 ml) and deprotected gold colloids (0.1 g) were added. After glass slides were placed at the bottom of the vessel it was exposed to an H₂S-atmosphere in a desiccator for 2, 8, and 16 hrs respectively. The solvent was removed and the glass slides were dried at room temperature.

10.5. References

- [1] M. Tamborra, M. Striccoli, R. Comparelli, A. Petrella, A. Agostiano, *Nanotechnol.* **2004**, *15*, S240-S244.
- [2] S. R. Ahmed, P. Kofinas, *J. Magn. Magn. Mater.* **2005**, *288*, 219-233.
- [3] E. H. Sargent, A. Shik, *J. Appl. Phys.* **2002**, *91*, 6679-6682.
- [4] X. G. Peng, M. C. Schlamp, A. V. Kadavanich, A. P. Alivisatos, *J. Am. Chem. Soc.* **1997**, *119*, 7019-7029.
- [5] S. U. Son, Y. Jang, J. Park, H. B. Na, H. M. Park, H. J. Yun, J. Lee, T. Hyeon, *J. Am. Chem. Soc.* **2004**, *126*, 5026-5027.
- [6] X. W. Teng, D. Black, N. J. Watkins, Y. L. Gao, H. Yang, *Nano Lett.* **2003**, *3*, 261-264.
- [7] H. Zeng, J. Li, Z. L. Wang, J. P. Liu, S. H. Sun, *Nano Lett.* **2004**, *4*, 187-190.
- [8] H. Kim, M. Achermann, L. Balet, J. A. Hollingsworth, V. I. Klimov, *J. Am. Chem. Soc.* **2005**, *127*, 544-546.
- [9] K. Mallik, M. Mandal, N. Pradhan, T. Pal, *Nano Lett.* **2001**, *1*, 319-322.
- [10] I. Honma, T. Sano, H. Komiyama, *J. Phys. Chem.* **1993**, *97*, 6692-6695.
- [11] Y. Lu, Y. D. Yin, Z. Y. Li, Y. A. Xia, *Nano Lett.* **2002**, *2*, 785-788.
- [12] C. Sanchez, G. S. Illia, F. Ribot, C. R. Mayer, V. Cabuil, T. Lalot, *Chem. Mater.* **2001**, *13*, 3061-3083.
- [13] N. V. Deshmukh, T. M. Bhave, A. S. Ethiraj, S. R. Sainkar, V. Ganesan, S. V. Bhoraskar, S. K. Kulkarni, *Nanotechnol.* **2001**, *12*, 290-294.
- [14] J. R. Lakowicz, I. Gryczynski, Z. Gryczynski, C. J. Murphy, *J. Phys. Chem. B* **1999**, *103*, 7613-7620.
- [15] P. V. Kamat, B. Shanghavi, *J. Phys. Chem. B* **1997**, *101*, 7675-7679.
- [16] M. Bartz, J. Küther, R. Seshadri, W. Tremel, *Angew. Chem.* **1998**, *110*, 2646-2649.
Angew. Chem. Int. Edn. Engl. **1998**, *37*, 2466-2468.
- [17] M. N. Tahir, P. Theato, W. E. G. Müller, H. C. Schröder, A. Janshoff, J. Zhang, J. Huth, W. Tremel, *Chem. Comm.* **2004**, *24*, 2848-2849.
- [18] M. N. Tahir, P. Theato, W. E. G. Müller, H. C. Schröder, A. Janshoff, S. Fiaß, J. Huth, W. Tremel, *Chem. Comm.* **2005**, 5533-5535.
- [19] J. Küther, R. Seshadri, W. Knoll, W. Tremel, *J. Mater. Chem.* **1998**, *8*, 641-650.

- [20] J. Küther, G. Nelles, R. Seshadri, M. Schaub, H. J. Butt, W. Tremel, *Chem. Eur. J.* **1998**, *4*, 1834-1842.
- [21] (a) J. Küther, R. Seshadri, W. Tremel, *Angew. Chem.* **1998**, *110*, 3196-3199. *Angew. Chem. Int. Ed.* **1998**, *37*, 3044-3047. (b) J. Küther, R. Seshadri, G. Nelles, W. Assenmacher, H. J. Butt, W. Mader, W. Tremel, *Chem. Mater.* **1999**, *11*, 1317-1325.
- [22] M. Bartz, J. Küther, G. Nelles, N. Weber, R. Seshadri, W. Tremel, *J. Mater. Chem.* **1999**, *9*, 1121-1125.
- [23] Y. Yang, M. Nogami, J. Shi, H. Chen, Y. Liuc, S. Qian, *J. Mater. Chem.* **2003**, *13*, 3026-3032.
- [24] M. Bartz, N. Weber, J. Küther, R. Seshadri, W. Tremel, *Chem. Comm.* **1999**, *20*, 2085-2086.
- [25] M. Brust, M. Walker, D. Bethell, D. J. Schiffrin, R. Whyman, *Chem. Comm.* **1994**, *7*, 801-802.
- [26] H. Zhang, D. Wang, H. Möhwald, *Angew. Chem.* **2006**, *118*, 262-265.
- [27] (a) R. S. Wagner, *Whisker Technology*, Wiley, New York, **1970**. (b) P. X. Gao, Z. L. Wang, *J. Phys. Chem. B* **2004**, *108*, 7534-7537.
- [28] T. Mokari, C. G. Sztrum, A. Salanti, E. Rabani, U. Banin, *Nature Mater.* **2005**, *4*, 855-863.
- [29] Y. Zhang, H. Jia, D. Yu, *J. Phys. D: Appl. Phys.* **2004**, *37*, 413-415.
- [30] H. Distler, *Angew. Chem.* **1967**, *11*, 520-529.
- [31] M. Bartz, J. Küther, R. Seshadri, W. Tremel, *Angew. Chem.* **1998**, *110*, 2646-2649. *Angew. Chem. Int. Ed.* **1998**, *37*, 2466-2468.
- [32] P. W. Scottl, I. T. Harrison, *J. Org. Chem.* **1981**, *46*, 1914-1915.

11. Summary and Conclusions

The present study displays new methods to make organic-inorganic hybrids nanomaterials in the micrometer and nanometer range. The main role of the design is based on the “bottom up” approach of nanotechnology using surface functionalization. Novel materials are synthesized by mimicking biomolecules, organic functional molecules and inorganic nanoparticles on a common platform. Such products can be used as raw material for the development of innovative devices or structures to benefit the society from revolutionary development in nanotechnology.

We have been able to present a novel NTA terminated alkanethiol which can successfully be self-assembled onto gold surfaces. These functionalized surfaces can immobilize histidine-tagged silicatein using the efficient chelating properties with Ni^{2+} . The results presented here demonstrate that silicatein, previously shown active for catalysing and structurally directing the polycondensation of silicon alkoxides in solution, when immobilized onto the surfaces is also capable of catalyzing and templating the polycondensation of monomeric silicon alkoxides to form silica structures on the surfaces.

A novel self-assembly of NTA on top of a “cushion” of reactive ester polymer has been successfully employed to make functionalized surfaces. These functionalized surfaces can immobilize histidine-tagged silicatein using the efficient chelating properties with Ni^{2+} . The results presented here demonstrate that silicatein, previously shown active for catalyzing and structurally directing the polycondensation of silicon alkoxides in solution as well as on surfaces can catalyze the deposition of titania and zirconia from aqueous solution. Furthermore, it became evident that silicatein exhibits a very general hydrolytic activity which seems independent of the coordination of the metal in the precursor compound. Finally, the results indicated that surface binding of crystallization promoters such as silicatein has an important impact on the morphology of the resulting products.

Silicatein, a protein related hydrolytic enzyme involved in the biomineralization of SiO_2 , was immobilized on the surface of TiO_2 nanowires with the aid of a reactive polymer, which simultaneously serves as an anchor to the oxide surface and as a chelating ligand for the binding of the protein.

The surface bound protein not only retains its original hydrolytic properties, but also acts as a reductant for AuCl_4^- in the synthesis of hybrid TiO_2 /silicatein/Au nanocomposites.

We have demonstrated for the first time that reactive polymer ligands containing dopamine serve as robust anchor on the surface of titanium dioxide nanoparticles. Compared to the binding of molecules to the surface of oxide particles using dopamine the novelty and superiority of the polymeric ligand system presented here is based on its multifunctionality, as it incorporates metal chelating ligands, a functional molecule (pyrene, NBD, and Texas Red) and additional entities which allow tailoring the solubility of inorganic nanocrystals in different organic solvents for various potential applications. As a possible extension of the work presented we envisage the immobilization of proteins to metal oxide surfaces using nitrilotriacetic acid (NTA) as an anchor ligand, i.e. our simple strategy should provide a useful way to link biofunctional molecules in almost any solvent to the surface of metal oxide particles, which may have a high affinity to dopamine or any other linker group which may replace the dopamine ligand in the polymer. This strategy is extremely versatile and offers new opportunities for optoelectronic and/or biological applications of metal oxide nanoparticles. Finally, this strategy allows the arrangement of inorganic nanoparticles to build up supramolecular structures, e.g. by introducing biotin/streptavidin linker units as functional molecules.

The formation of Au nanoparticles by the hydrolytic protein silicatein has been demonstrated. The reduction of AuCl_4^- species occurs by the action of sulfhydryl groups hidden below the surface groups of the protein. The gold nanoparticles resulting from the bioreduction by silicatein are stabilized by surface binding through the NH_2 groups of the basic amino acid residues of silicatein, as shown by fluorescence microscopy using a fluorophore attached to the protein by specific antigen-antibody interactions. The Au nanoparticles further aggregate to form Au nanocrystals as evidenced by transmission electron microscopy. The triangular shape of the nanocrystals obtained by using recombinant silicatein may be explained by chiral induction through the protein during the nucleation of the nanocrystals.

Rutile TiO_2 nanorods with dimensions of 15 x 80 nm have been synthesized under mild conditions in high yield in a facile and reproducible manner. Establishing a versatile procedure gave us not only the control on size, morphology and crystallinity, but also on surface functionalization. The reaction conditions used in the synthesis allow the *in situ*

functionalization of the rutile TiO₂ nanorods. As an example, we showed that surface bound amine groups can bind covalently to the fluorescent dye NBD.

This technique of tailored surface functionalization opens further possibilities for improving the quality of rutile pigments or the fabrication of conducting polymer/TiO₂ thin films, which would enhance the performances of electronic or optoelectronic devices based on such nanocomposite thin films (e.g. photovoltaic or electroluminescent devices).

A multipod ligand has been designed to achieve the functionalization of highly inert MoS₂ nanoparticles through a high degree of surface binding using the principles of coordination chemistry. For this purpose we have used the tetradentate NTA ligand which was coupled either to a fluorescent ligand for detection purposes or to a reactive polymer, which simultaneously serves as an anchor to the sulfide (via the NTA groups) and the oxide surfaces (via the catecholate groups) of IF-MoS₂ and TiO₂. We believe that this functionalization protocol can be generalized for various layered chalcogenide nanoparticles.

The functionalization of fullerene-type chalcogenide nanoparticles opens several new fields for this class of materials which have been pursued actively during the past few years for the related carbon nanotubes and various oxide materials: (i) the functionalization of chalcogenide nanotubes for the attachment of electronically active components (metal and semiconductor nanoparticles, light harvesting ligands for solar cell applications) to the sidewalls of the tubes, (ii) dispersion of nanotubes, e.g. for the integration in composites which is of interest because of their exceptional mechanical properties. (iii) Furthermore, it allows the fabrication of thin films by surface binding of chalcogenide particles to oxide surfaces, which might allow their use as lubricants on seemingly incompatible ceramic materials.

Crystalline ZrO₂ nanoparticles were prepared from zirconium isopropoxide by slow hydrolysis and subsequent hydrothermal treatment of solutions containing various amounts of sodium hydroxide at 180° C. Whereas basic solutions lead to the formation of nanoparticles of monoclinic ZrO₂ with platelike morphology, monodispers nanoparticles of the cubic ZrO₂ high-temperature polymorph with diameters of approx. 5 nm were obtained from strongly basic solutions. The morphology, structure and properties of as synthesized nanoparticles were characterized using HRTEM, XRD, Raman spectroscopy, UV-vis, PL spectroscopy and BET measurements. The formation of both, the monoclinic and the cubic polymorph was confirmed by electron microscopy and Raman spectroscopy. The crystallinity and

morphology of the resulting ZrO_2 nanoparticles can be adjusted by the choice of the reaction conditions. The cubic ZrO_2 nanoparticles have a high surface area ($300 \text{ m}^2/\text{g}$) and exhibit a strong photoluminescence in the UV region.

Bare gold colloids exposed to long-chain dithiols result in precipitate owing to cross-linking of the thiol groups with gold surfaces. We have shown that through the use of a dithiol that has one of the thiol groups protected, we can, through attachment followed by deprotection, prepare gold colloids with exposed thiol. The use of such 'sticky' colloids in creating complex architectures is demonstrated by using them to template the growth of CdS nanoparticles and nanowires.

12. Methods and Instrumentation

12.1. Surface plasmon resonance spectroscopy (SPR)

The Surface Plasmon Resonance spectroscopy ^[1] is a versatile tool to measure the thickness of thin films adsorbed onto a metal surface. The method is based on electrons which have the ability to move nearly free as electron gas and thus they are completely disconnected from the atomic nucleus. This property is related to metals with a complete d-shell, having valence electrons in s- or p-orbitals like gold or silver. Under these circumstances the electrons are able to relay vibrations, i. e. the charge density like the gas particles in air. These fluctuations of the charge density are called plasmon. They show characteristic vibration energy:

$$E_p = \hbar \cdot \omega_p = \hbar \cdot \sqrt{\frac{4\pi\eta e^2}{\epsilon\epsilon_0 m_e}}$$

η = electron concentration

m_e = electron mass

ϵ, ϵ_0 = dielectric constants

As the vibrational energy acts as an electromagnetic wave the electrons can be excited by radiation.

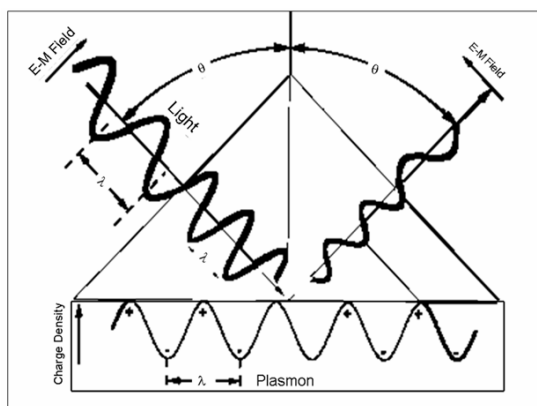


Figure 12.1.1. Kretschmann configuration of the plasmon resonance

The excitation of the plasmon is possible at a metal-dielectric interface by a monochromatic light beam, normally by a Helium-Neon laser and can be understood as a longitudinal

propagation of the surface plasmon at the interface. Therefore, it is surface selective as well as a surface sensitive method. It is observed as a deep minimum in the p-polarised reflected light as the angle-of-incidence is incremented. The amplitude of the vibration is exponentially

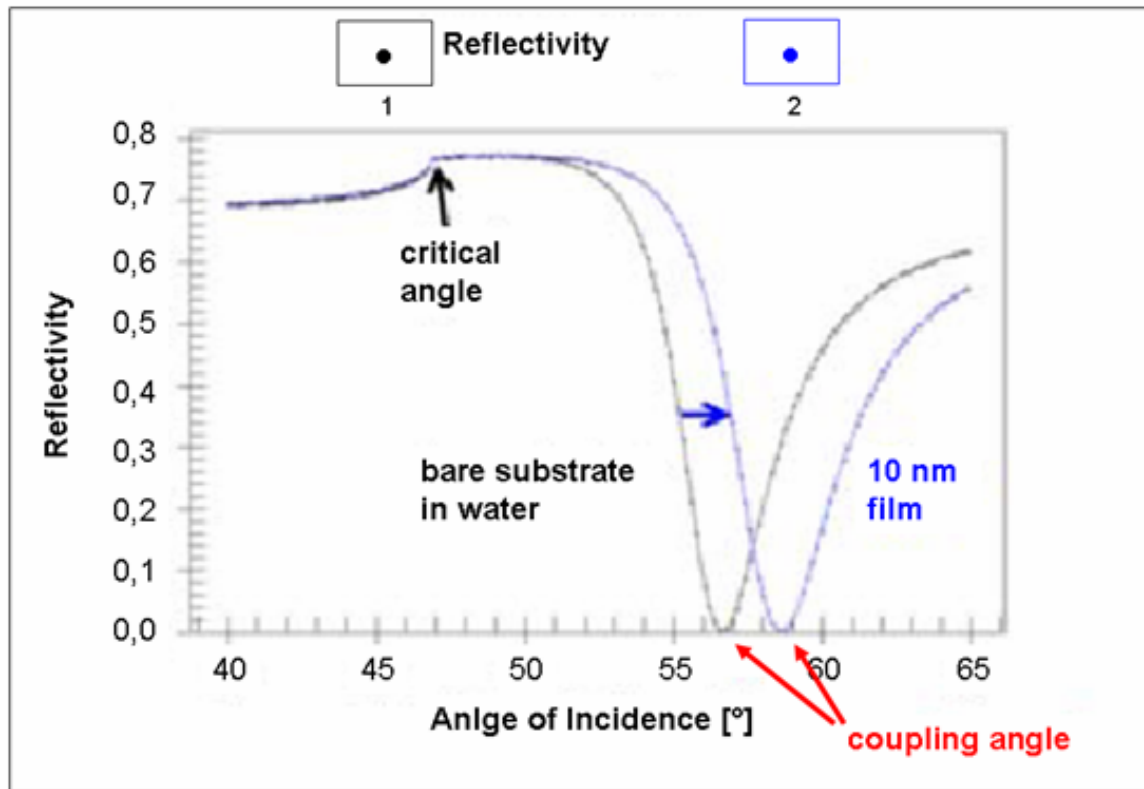


Figure 12.1.2. Plasmon spectrum from bare gold (black line) and with a substrate on the gold surface (blue line)

debilitated into the interior of the metal with a penetration depth of about ~ 100 nm. To measure the film thickness at a gold surface the most convenient configuration for plasmon resonance is the Kretschmann configuration (Figure 12.1.1) [2]. The plasmon is measured at the interface between a dielectric material and the gold, where the light comes from a medium with a higher refractive index to penetrate a material with a lower refractive index. The Snellius equation of refraction is valid (Figure 12.1.1):

$$\frac{\sin \alpha}{\sin \beta} = \frac{n_2}{n_1}$$

The phenomenon of total reflection is observed by the transition of light from an optically dense material to a less dense material. In this case β is $> 90^\circ$. At critical angle of $\alpha_T = \alpha$, β is 90° and thus $\sin \beta = 1$. The refraction equation results in:

$$\sin \alpha_T = \frac{n_2}{n_1}$$

At this critical angle total reflections of the light beam occur. Thus the plasmon spectra show a maximum (Figure 12.1.2). If α increases more, a small part of the incident light beam energy passes through the boundary layer between glass and gold. This so called evanescent wave couples with the plasmon and at a certain angle a maximum of energy is absorbed resulting in a minimum in the spectrum.

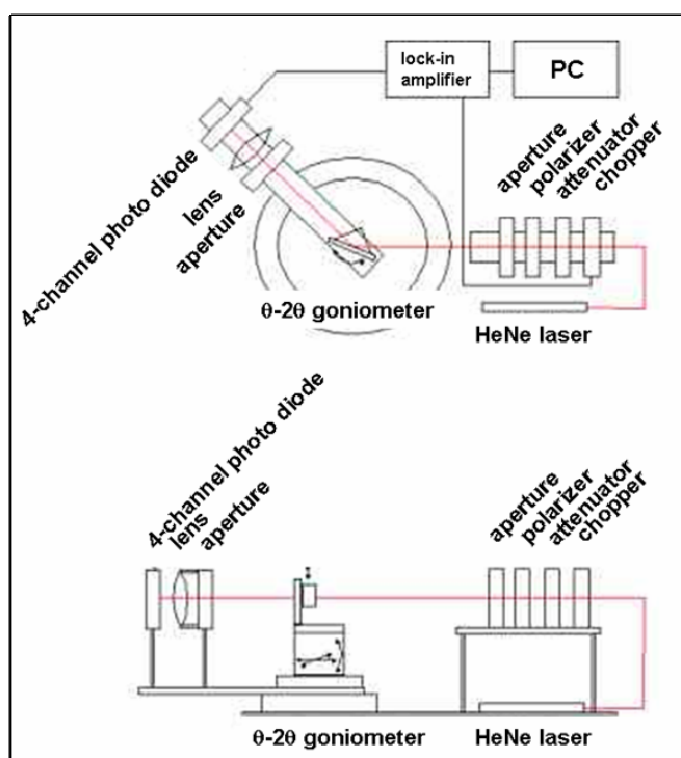


Figure 12.1.3. Kretschmann set-up of a surface plasmon spectrometer

This coupling angle indicates the point of the highest light absorption by the plasmon, i. e. the collective oscillation of the electrons with the light. The value of the experiment is that the exact angle for the plasmon resonance peak is extremely sensitive to any thin film on the metal surface even for a monolayer consisting of organic molecules. So the minimum position of the peak can be used to determine the thickness and density. The theoretical characterization of these phenomena is completely understood and the thickness of the layer can be inferred from the angle shift between spectra taken from the clean gold surface and from the gold surface with an absorbed layer by simulation with programs like WINSPALL [3].

One of the important advantages of the SPR analysis is the quite good time resolution since the surface plasmon can be generated and measured in a short time. Thus real time analysis can be made as in kinetic measurements of the absorption of a solute like proteins.

For this PhD thesis all measurements were done using a spectrometer in the Kretschmann-configuration purchased from Resonant Probes GmbH (Goslar) ^[4]. A graphical description of the complete equipment is shown in Figure 12.1.3.

12.2. Atomic force microscopy (AFM)

All scanning techniques which use a sharp tip moving over the surface of a sample in a raster scan are summarized under the name scanning probe microscopy (SPM) ^[5,6]. Binnig, Rohrer, and Gerber invented in 1982 the scanning tunnelling microscope (STM), the first type of SPM. They won the Nobel Prize in 1986. This method based on electron tunnelling, i.e. an electrical current that flows between two conductors that are separated by very short distances at Angstrom scale. This tunnelling current depends exponentially on the distance between the two conductors. By monitoring the current over each point of the surface of the sample, the electronic topography of the surface is recorded. Thus there are two distinguishable modes of operation:

- i) **Constant Height Mode:** When the distance between tip and samples is kept constant current is recorded over each point giving the electronic properties of the sample;
- ii) **Constant Current Mode:** When the current is kept constant during the scan the topography of the substrate surface is recorded.

This microscopic method is restricted to conductive substrates but permits atomic information not from an average over many atoms, but over atom by atom.

The complementary technique to the STM is the atomic force microscopy (AFM). With this instrument also non-conducting materials can be investigated. It was invented by Binnig, Quate and Gerber in 1986. The AFM uses a cantilever with a sharp tip moving over the surface of the sample in a raster scan. The cantilever bends in response to the force between the tip and the sample surface. Most of the AFMs employ an optical lever technique for detecting the bending of the cantilever. The light from a laser is reflected from the cantilever onto a split photo-diode. By measuring the aberration of the signal, and changes in the bending of the cantilever, (as the cantilever obeys Hooke's Law for small displacements,) the interaction force between the tip and the sample can be determined (Figure 12.2.1). The displacement of the tip or sample is performed by an extremely precise positioning device made from piezo-electric ceramics with a resolution of sub-angstrom.

There are principally three different classes of interaction between tip and sample: contact mode, tapping mode, and non-contact mode.

- 1) Contact mode signifies a close contact between tip and sample during scanning progress. Close contact mean that the tip approach to the surface that the inter-molecular repulsive force become positive and producing large lateral forces on the sample and the tip is dragged over the surface.(Figure 12.2.2)
- 2) The tapping mode is used by poorly immobilized or soft samples. By operating in air or other gases, the cantilever oscillates at its resonant frequency and is positioned above the surface. It only taps the surface for a very small part of its oscillation period. Thus it has a short time contact with sample surface. This decrease dramatically the lateral force as the tip scans over the surface.
- 3) The third mode of measuring is the non-contact mode. The cantilever oscillates above the surface at such a distance that there is no lateral force which means that it is no longer in the repulsive regime of the inter-molecular force curve.

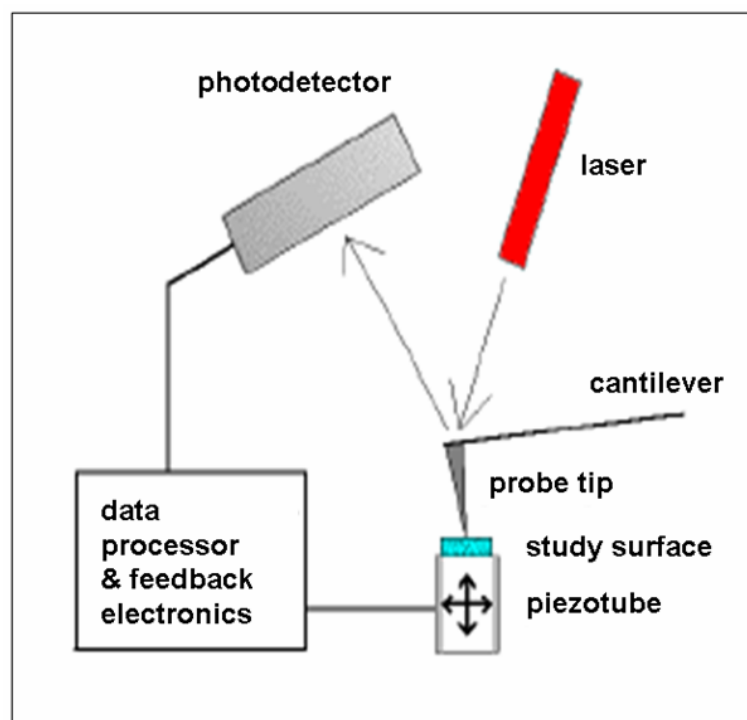


Figure 12.2.1. Schematic illustration of the measurement technique by an Atomic Force Microscope.

Apart from the study of topography with high resolution and interactions between the tip and the surface of nearly every material, AFM also can be applied for nanomechanic studies

employing the AFM tip to produce indents in a specimen or for friction measurements by scratching the tip over the surface.

The great advantage of all SPM techniques is the ability to do time-resolved investigations down to atomic or near-atomic processes in all materials.

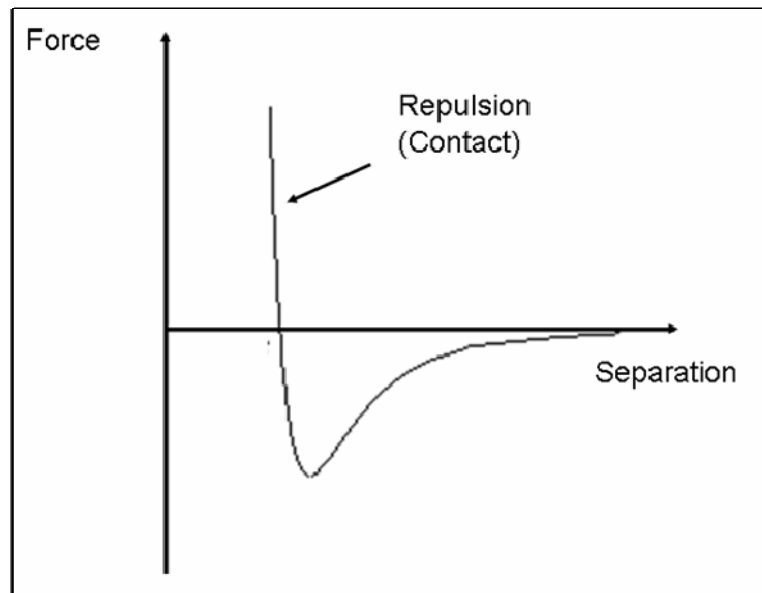


Figure12.2.2. Inter-molecular force curve

In this Ph.D. thesis samples were imaged at room temperature with a commercial SFM (Nanoscope IIIa, Digital Instruments, Santa Barbara, California) employing Tapping ModeTM using rectangular silicon cantilevers (Nanosensors, 125 μm long, 30 μm wide, 4 μm thick) with an integrated tip, a nominal spring constant of 42 N m⁻¹, and a resonance frequency of 330 kHz. To control and enhance the range of the attractive interaction regime the instrument was equipped with a special active feedback circuit, called Q-control (Nanoanalytics, Germany).

12.3. Confocal laser scanning microscopy (CLSM)

Confocal laser scanning microscopy (CLSM) is a valuable tool for obtaining high resolution images and 3-D reconstructions. The key feature of confocal microscopy is its ability to produce blur-free images of specimens at various depths. The principle for this special kind of microscopy was developed by Marvin Minsky in 1953, but it took another thirty years and the development of lasers as near-ideal point light sources for confocal microscopy to become a standard technique toward the end of the 1980s. In a typical laser scanning confocal microscope (Figure 12.3.1) a laser beam passes a light source aperture and then is focused by an objective lens into a small (ideally diffraction-limited) focal volume within a fluorescent specimen.^[7]

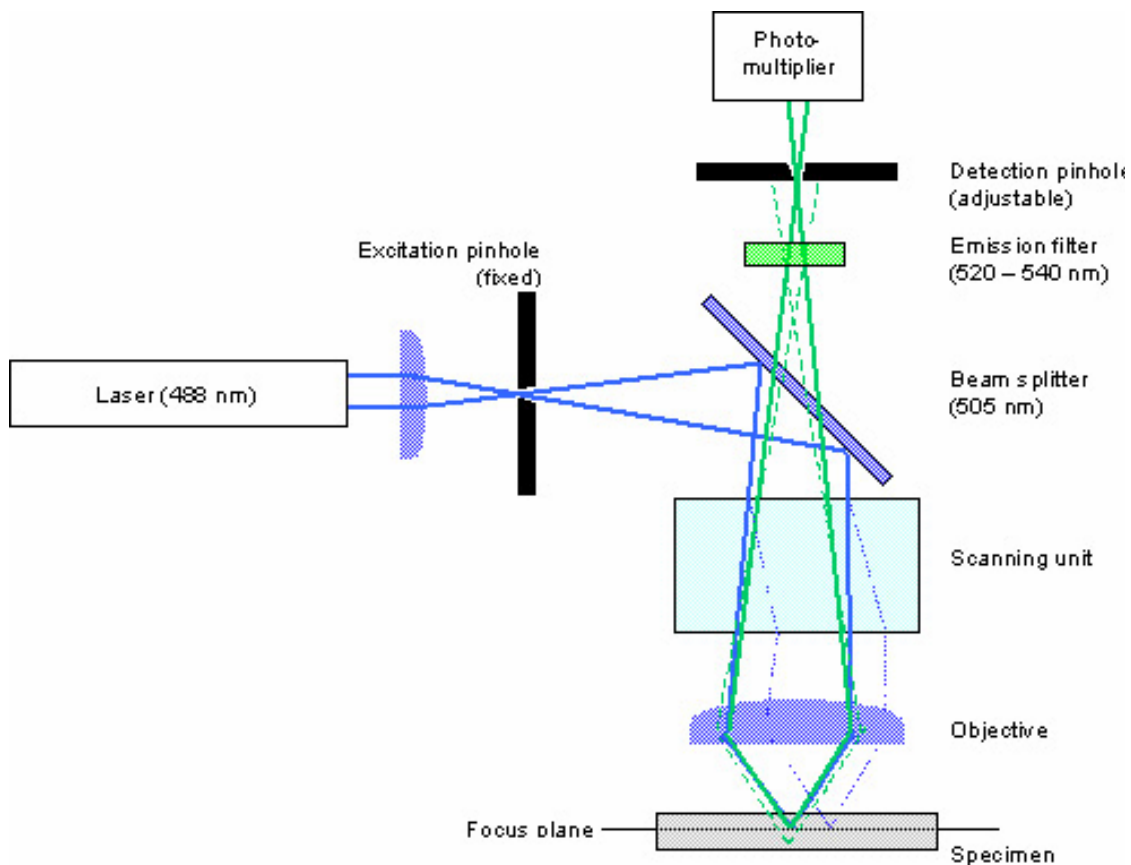


Figure 12.3.1. Pictorial representation of confocal laser scanning microscopy.

A mixture of emitted fluorescent light as well as reflected laser light from the illuminated spot is then recollected by the objective lens. A beam splitter separates the light mixture by allowing only the laser light to pass through and reflecting the fluorescent light into the

detection apparatus. After passing a pinhole the fluorescent light is detected by photo-detection device (photomultiplier tube or avalanche photodiode) transforming the light signal into an electrical one which is recorded by a computer.

In this doctorate dissertation, the confocal laser scanning microscope used was an inverted laser scanning microscope, equipped with He/Ne Laser (Leica TCS SL, Leica Microsystems, Bensheim, Germany).

12.4. References

- [1] (a) W. Knoll, *MRS Bulletin*, **1991**, *16*, 29-39. (b) A. Janshoff, H. J. Galla, C. Steinem, *Angew. Chem.* **2000**, *112*, 4164-4195. (c) H. Raether, "Surface Plasmons on Smooth and Rough Surfaces and on Gratings", Tracts in Modern Physics, Springer Verlag, Berlin, **1988**. (d) E. Burstein, W. P. Chen, Y. J. Chen, A. Hartstein, *J. Vac. Sci. Technol.*, **1974**, *11*, 1004-1019. (e) B. Rothenhäusler, C. Duschl, W. Knoll, *Thin Solid Films*, **1988**, *159*, 323-330.
- [2] E. Kretschmann, *Z. Physik.* **1971**, *241*, 313-324.
- [3] <http://www.mpip-mainz.mpg.de/documents/akkn/index.html>.
- [4] <http://www.resonant-probes.de>
- [5] D. Sarid, *Scanning Force Microscopy*, Oxford Series in Optical and Imaging Sciences, Oxford University Press, New York, **1994**.
- [6] R. Wiesendanger, *Scanning probe microscopy: analytical Methods*, Springer, Berlin, **1998**.
- [7] http://en.wikipedia.org/wiki/Confocal_laser_scanning_microscopy

13. Appendix

13. 1. List of figures

- Figure 1.1.** Comparison on length scale between naturally and artificially engineered materials.
- Figure 1.2.** a) Oxalate crystal synthesized in plant leaves, b) Oxalate crystals synthesized in the laboratory.
- Figure 1.3.** Catalytic mechanism of silicatein (Zhou et al. 1999).
- Figure 1.4.** 3-D structure of cathepsin L (right) and silicatein (left).
- Figure 1.5.** Use of functionalized nanoparticles on nanotechnology.
- Figure 2.1.** Nitrilotriacetic acid (NTA) terminated alkanethiol.
- Figure 2.2.** SPR curves of gold (circles), NTA alkanethiol on gold (triangles) and immobilized silicatein thereon (squares).
- Figure 2.2.** SPR curves of gold (circles), NTA alkanethiol on gold (triangles) and immobilized silicatein thereon (squares).
- Figure 2.3.** SFM height pictures of a) gold (111) surface, b) NTA alkanethiol on gold and c) immobilized silicatein (same scale for all images).
- Figure 2.4.** SEM images of silicization onto surfaces functionalized with NTA alkanethiol without Ni^{2+} (a) and NTA alkanethiol with Ni^{2+} chelating silicatein (b, c). No observable formation of SiO_2 occurred on NTA alkanethiol modified surfaces (a). In contrast, Ni^{2+} chelated silicatein immobilization onto NTA alkanethiol surfaces induced the formation of SiO_2 (b,c), as evidenced by the EDX-spectrum (d).
- Figure 3.1.** Immobilization of silicatein using cysteamine, a reactive ester polymer, and the NTA ligand.
- Figure 3.2a.** SPR curves of cysteamine on gold (dots), polymer with NTA (open circles) and immobilized silicatein thereon (filled circles).

- Figure 3.2b.** Reflectivity plotted as a function of time in the absence (solid line) and presence (dotted line) of Ni^{2+} indicating the specific binding of the silicatein to the NTA linker.
- Figure 3.3a.** FT-IR of NH_2 functionalized gold substrate (dotted line) and covalently bound reactive polymer on top (solid line).
- Figure 3.3b.** CLSM picture of fluorophore labeled silicatein.
- Figure 3.4.** SEM/HRSEM images of TiO_2 (a) and (c) and ZrO_2 (b) and (d) formed by catalysis using surface-bound silicatein. No observable formation of TiO_2 or ZrO_2 occurred on NTA alkanethiol modified surfaces.
- Figure 4.1.** UV-Vis spectra of the products of the reaction of recombinant silicatein with AuCl_4^- recorded as a function of time. (a) 60 min, (b) 180 min, (c) 300 min, (d) 420 min.
- Figure 4.2.** TEM images of AuCl_4^- reduced with aqueous solutions of recombinant silicatein. (a) Au nanocrystals on the axial filaments from *S. domuncula*. (b) Au nanocrystals not attached to the axial filament with SAED (selected area diffraction pattern), indicating the crystalline nature of the sample. (c) TEM image of the edge of one of the nanocrystals in (b) decorated with small nanocrystals stabilized by silicatein. The inset reveals the crystallinity of the smaller nanocrystals. This image demonstrates the high surface mobility at the edges of the nanocrystals. (d) Triangular Au nanocrystals obtained by using recombinant instead of native silicatein.
- Figure 4.3.** Upon covalent immobilization of fluorophore-labeled (Cy2 label) secondary goat anti rabbit antibodies onto their surfaces, the surface bonded silicatein can be visualized by using fluorescence microscopy.
- Figure 4.4.** FT-IR spectrum of biocatalytically synthesized gold nanoparticles.
- Figure 4.5.** (a) Au nanocrystal with fcc structure. (b) Morphology of a triangular slice cut from a 3D gold crystal. (c) A stacking fault in the structure can be constructed by mirroring the triangle and gluing it to the first one face to face. (d) The hexagonal platelets can be modeled by truncating the three corners of a triangle. (e) One can construct a faulted hexagon by mirroring with a perimeter containing (f) alternating bulges and notches (convex and concave faces).

- Figure 5.1.** XRD powder pattern of as-synthesized amine functionalized rutile TiO₂ nanorods.
- Figure 5.2.** TEM micrographs of the rutile TiO₂ nanorods: overview image (a), HRTEM image (b) and (c). Figure 2d shows the electron diffraction pattern of a TiO₂ nanorod.
- Figure 5.3.** FT-IR data of as synthesized functionalized TiO₂ nanorods.
- Figure 5.4.** NMR data of as synthesized TiO₂ nanorods.
- Figure 5.5.** Photographs of amino functionalized TiO₂ nanorods in water: suspension at pH = 2 (a), precipitate at pH = 10 (b), and re-suspension at pH = 2 (c).
- Figure 5.6.** Schematic illustration of the binding of the fluorescent dye NBD to the surface functionalized rutile TiO₂ nanorods (a). UV-VIS absorption spectrum of amine functionalized rutile TiO₂ nanorod solution in water (b). Confocal LASER scanning microscopy image of dye functionalized nanorods at 488 nm excitation (c).
- Figure 6.1.** Stepwise synthesis of the multifunctional polymeric ligand containing a dye. The active ester units of the polymer are successively exchanged by 1-pyrenemethylamine (**P1**), pipNBD (**P2**) and Texas Red (**P3**), respectively. The polymer contains 3-hydroxytyramine as anchors for the nanoparticles, alkyl chains for solubility and dye molecules.
- Figure 6.2.** Transmission electron micrographs of (a) synthesized TiO₂ nanowires, (b) nanoparticles (overview image) and (c) HRTEM image of an individual nanoparticle. The Fourier Transform (FFT) is given in the lower right corner. A theoretical HRTEM image of the [100] zone is shown given in the upper left corner.
- Figure 6.3.** X-ray diffraction pattern of *in-situ* functionalized TiO₂ nanoparticles. The pattern can be fully indexed to anatase, indices of the reflections are marked. Calculated positions of the anatase reflections are indicated by black ticks.
- Figure 6.4.** Shows the confocal laser scanning microscopy images of TiO₂ nanowires and nanoparticles after surface functionalization with **P2** and **P3**, respectively.
- Figure 6.5.** Digital camera photograph demonstrating the solubility of functionalized TiO₂ nanoparticles in chloroform/water under illumination with UV light ($\lambda = 365$ nm).

- Figure 6.6.** Fluorescence spectra of TiO₂ nanoparticles coated with **P1** (pyrene, solid line), **P2** (NBD, dashed line) or **P3** (Texas red, dotted line). TiO₂ nanoparticles carrying the **P1** pyrene fluorophore were excited at 345 nm. TiO₂ nanoparticles coated with **P2** were excited at 460 nm, and the fluorescent spectra for **P3** were recorded with an excitation wavelength of 488 nm.
- Figure 6.7.** Fluorescence spectra of NBD depending on the preparation conditions. Solid line; emission spectrum of **P2** dissolved in CHCl₃, TiO₂ particles coated with **P2** show a 10 nm blue-shifted maximum, whereas TiO₂ particles with the polymeric ligands (**P2**) show a blue shift of 17 nm with respect to **P2**.
- Figure 7.1.** Synthesis of a functional polymeric ligand containing nitrilotriacetic acid (NTA) and dopamine units.
- Figure 7.2.** FT-IR spectra (a) TEM image of TiO₂ nanowires (dashed line), b) polymeric ligand (dotted dashed line) and c) TiO₂ nanowires functionalized with polymeric ligand (solid line).
- Figure 7.3** (a) Antigen capture assay. (A) TiO₂/silicatein complex (globular symbol = silicatein, oval dentate symbol = non-specific BSA (Bovine Serum Albumine), and Y symbol = specific monoclonal anti silicatein of *S. domuncula*. Assay visualized by recognition of antigen/antibody by fluorophore Cy2 coupled to antibodies detecting the mouse F_{AB}. Upon immobilization of fluorophore-labeled Ab (antibodies) onto the TiO₂/polymer/silicatein surface, the surface bound silicatein can be visualized by using Confocal laser scanning microscopy (CLSM). (b) Overview image showing many functionalized and immobilized silicatein TiO₂ nanowires. (c) HRCSLM image showing the presence of several adjacent fluorescence spots which indicates the binding of several silicatein molecules on a TiO₂ nanowire.
- Figure 7.4.** Schematic presentation of the TiO₂ nanowire/Au nanocrystals fabrication. In the first step the TiO₂ nanowire is functionalized with the multifunctional polymer ligand (red) by complexation through the catechol groups. The NTA tripod ligand is bound to the side groups of the polymer. In the next step silicatein containing HIS-tag is attached to the NTA ligand by Ni²⁺ complexation through the His-tag. Finally, tetrachloroauric acid is reduced by the sulfhydryl groups of immobilized silicatein. The Au nanocrystals are chemically bonded to the amino groups at the protein periphery.

- Figure 7.5.** UV-vis absorption spectrum of a) synthesized TiO₂ nanowires (green line), b) polymeric ligand (red line), c) HAuCl₄ solution (black line) and d) polymer functionalized TiO₂ nanowires with immobilized silicatein and bio-reduced Au nanoparticles (blue line).
- Figure 7.6.** HR-SEM image demonstrating the hierarchical structure of the TiO₂ nanowire/Au nanoparticle composite. Overview images of the TiO₂/Au nanocomposites (top left) and a magnified view (right bottom) are given as insets.
- Figure 7.7.** (a) TEM image of TiO₂ nanowires. (b) overview image of TiO₂ nanowires decorated with Au nanocrystals, obtained by reduction with surface bound silicatein. (c) EDX spectrum of a TiO₂ nanowire decorated with Au nanocrystals, indicating the presence of Ti, O and Au. (d) Magnified view of a single TiO₂ nanowire with Au nanocrystals attached. (e) HRTEM of a crystal edge, (marked by a circle in the inset) showing the polycrystalline nature of the nanocrystal. (f) Nano-electron diffraction (NED) of an Au nanocrystal shown in the inset.
- Figure 8.1.** NTA ligand functionalized with a fluorescent 7-nitrobenzofurazan.
- Figure 8.2.** Synthesis of the block copolymer with catechol-type side groups for metal oxide binding and umbrella-type nitrilotriacetic acid ligands blocking on side of the coordination sphere of metals bonded to the S atoms of the MoS₂ surface layer, thereby preventing a precipitation of MoS₂ nanoparticles due to cross-linking.
- Figure 8.3.** Photograph of a solutions/dispersions of IF-MoS₂ before (right) and after (left) surface functionalization in water after (top layer) and in CHCl₃ (bottom layer).
- Figure 8.4.** (a) HRTEM image of a surface functionalized IF-MoS₂ particle. (b) EDX spectrum of the area marked by a circle in (a).
- Figure 8.5.** (a) FT-IR spectrum of polymer functionalized IF-MoS₂ nanoparticles. (b) FT-IR spectrum of NTA functionalized IF-MoS₂ nanoparticles. (c) UV-Vis absorption spectrum of a IF-MoS₂ dispersion (solid line), the polymer (dotted line) and the functionalized IF-MoS₂ nanoparticles (dashed line). (d)

Determination of the mass ratio of IF-MoS₂ versus polymer by thermogravimetry.

Figure 8.6. Fluorescence spectrum of IF-MoS₂ nanoparticles coated with a NBD fluorophore coupled to the NH₂ group of the NTA ligand. MoS₂ nanoparticles coated with NTA-NBD were excited at 488 nm.

Figure 8.7. (a) TEM image of IF-MoS₂ particles immobilized on a TiO₂ nanorods by surface wall functionalization. (b) Magnified image of the rectangle marked in (a).

Figure 9.1. TEM images of ZrO₂ nanoparticles a) overview 3M NaOH, b) diffraction pattern, c) growth of crystal d) and e) overview of Cubic ZrO₂ nanoparticles with 10M NaOH, f) TEM powder diffraction, g) HRTEM of single nanoparticle, simulated HRTEM image (top left side) and FFT (bottom right side) h) HRTEM diffraction pattern

Figure 9.2. XRD powder pattern of as synthesized ZrO₂ nanoparticles from a) 3M NaOH, b) 5M NaOH c) 10M NaOH

Figure 9.3. Raman spectrum of cubic ZrO₂ nanoparticles synthesized using 10M NaOH.

Figure 9.4. Photoluminescence spectrum of ZrO₂ nanoparticles synthesized using 10M NaOH excited at $\lambda = 270$ nm. (red color), the excitation spectrum of the corresponding emission at $\lambda = 376$ nm (blue color)

Figure 9.5. BET isotherm at 675K: N₂ on ZrO₂ 10M NaOH

Figure 10.1. Schematic illustration of the synthesis of thiol functionalized Au colloids.

Figure 10.2. Absorption spectra of (a) CdS nanostructures (16 hours) b) Au-CdS nanocomposites (2 hours) c) Au-CdS nanocomposites (8hours) d) Au-CdS nanocomposites (16hours), e) colloidal Au nanoparticles precipitation of CdS.

Figure 10.3. SE micrographs of Au-CdS nanocomposites grown with respect to time 2 hours (a & b), 8 hours (c & d), 16 hours (e & f) whereas (g & h) shows SE micrograph of CdS nanostructures precipitated in the absence of Au colloids.

Figure 10.4. SE micrograph of CdS nanowires synthesized using thiol protected gold colloids at 45 °C a) overview, b) HRSEM.

Figure 12.1.1. Kretschmann configuration of the plasmon resonance.

Figure 12.1.2. Plasmon spectrum from bare gold (black line) and with a substrate on the gold surface (blue line).

Figure 12.1.3. Kretschmann set-up of a surface plasmon spectrometer.

Figure 12.2.1. Schematic illustration of the measurement technique by an atomic force microscope.

Figure 12.2.2. Inter-molecular force curve.

Figure 12.3.1. Pictorial representation of confocal laser scanning microscopy.